POLYPUBLIE

High-Field Magnetization Methods for Characterizing the Critical Current Density of REBCO Tapes

Simon-Mathieu Bergeron Hartman

Document en libre accès dans PolyPublie
Open Access document in PolyPublie

Date	2025
Type	Mémoire ou thèse / Dissertation or Thesis Mémoire de maîtrise/Master's thesis
URL de PolyPublie PolyPublie URL	https://publications.polymtl.ca/71351/
Conditions d'utilisation Terms of use	© Tous droits réservés / All rights reserved
Référence Citation	Bergeron Hartman, S.-M. (2025). High-Field Magnetization Methods for Characterizing the Critical Current Density of REBCO Tapes [Mémoire de maîtrise, Polytechnique Montréal]. PolyPublie. https://publications.polymtl.ca/71351/

Détails de la thèse
Thesis details

Directeurs de recherche Advisors	Frédéric Sirois
Programme Program	Génie électrique

Ce fichier a été téléchargé à partir de PolyPublie, le dépôt institutionnel de Polytechnique Montréal
This file has been downloaded from PolyPublie, the institutional repository of Polytechnique Montréal
https://publications.polymtl.ca

POLYTECHNIQUE MONTRÉAL
affiliée à l'Université de Montréal

High-Field Magnetization Methods for Characterizing the Critical Current Density of REBCO Tapes

SIMON-MATHIEU BERGERON HARTMAN
Département de génie électrique

Mémoire présenté en vue de l'obtention du diplôme de *Maîtrise ès sciences appliquées*
Génie électrique

Décembre 2025

© Simon-Mathieu Bergeron Hartman, 2025.

POLYTECHNIQUE MONTRÉAL
affiliée à l'Université de Montréal

Ce mémoire intitulé :

High-Field Magnetization Methods for Characterizing the Critical Current Density of REBCO Tapes

présenté par **Simon-Mathieu BERGERON HARTMAN**
en vue de l'obtention du diplôme de *Maîtrise ès sciences appliquées*
a été dûment accepté par le jury d'examen constitué de :

David MÉNARD, président
Frédéric SIROIS, membre et directeur de recherche
John DURRELL, membre

DEDICATION

À Raphaëlla, Leo et Josée

ACKNOWLEDGEMENTS

I would first like to thank my advisors at Polytechnique Montréal, Frédéric Sirois, and at the Los Alamos National Laboratory, Doan Nguyen. I have now known Frédéric for several years and I can say that working with him has always been a great privilege and pleasure. Over the years, I have greatly benefited from the opportunities he has given me, which include this project with the Los Alamos National Laboratory. I would also like to thank Doan for kindly taking me on as his student and helping me navigate this project.

I would like to acknowledge the funding I received from the Fonds de recherche du Québec and from the Department of Energy of the United States government, which made this project possible.

I would like to express my gratitude to the members of the jury for accepting to review my thesis. Your feedback and insight are very much appreciated.

Over the last couple of years, I was trained, oriented, and accompanied by several individuals, and my work benefited from this tremendously. Among these people, I would first like to express my heartfelt gratitude to Boris Maiorov, who pointed me towards key publications in my field, helped train me for magnetization measurements, and always had time for my questions and long inquiries. The insights that you provided were instrumental to the success of this work. I would also like to thank Shengzhi Zhang and Minseong Lee, who both accompanied me through my first magnetization measurements and who were always available when I needed help. I additionally would like to highlight the extensive amount of time spent by Tim Noe and John Singleton operating the pulsed magnets for me. The help that you gave me was received with a lot of gratitude. Likewise, I would like to express my heartfelt thanks to Prof. Patrick Fournier, who performed many measurements on my behalf, many of which turned out to be central to a large portion of this work. A large amount of time was necessary to fine-tune the measurement procedure and I am very thankful that you took it. Many others contributed to my work, and I would therefore like to thank them and acknowledge the help from Linh, Chris, Oscar, Daniel, Danielle, Gregory, and Tannor. I would also like to thank the friends in Montréal and Los Alamos that have accompanied me, in particular, Yara, Tannor, Leah, Paul, Gregory, Nicolas, Jim, Manu, and Éli.

Finally, I would like to thank and express my gratitude to my sister, Raphaëlla, who has been a model of mine for many years. I also want to thank my father, Leo, whose wisdom gained from past academic experiences helped me find my way during challenging times. Finally, I would like to thank my mother Josée, who, more than she knows, is the biggest source of inspiration in my life.

RÉSUMÉ

Les supraconducteurs à haute température HTS («high-temperature superconductor» en anglais) et, plus spécifiquement, les supraconducteurs REBCO («rare earth barium copper oxides» en anglais) sont des matériaux très prometteurs pour le développement d'aimants à champ magnétique très intense. Leurs propriétés comme la densité de courant critique J_c, la température critique T_c et le champ magnétique critique B_{c2} sont en général très élevées, ce qui les rend avantageux dans ce contexte. Ceci dit, J_c varie fortement en fonction de la norme du champ magnétique local B, de l'orientation décrite par l'angle θ du champ magnétique et de la température T. Ceci rend la conception de dispositifs de puissance à base de supraconducteurs REBCO difficile et il devient crucial d'avoir une connaissance détaillée de $J_c(B, \theta, T)$.

Le but de ce mémoire est de développer une méthode permettant de calculer $J_c(B, \theta, T)$ de rubans REBCO commerciaux à partir de mesures par aimantation pulsée PFM («pulsed field magnetization» en anglais). Ce faisant, il serait possible d'éviter les difficultés techniques des mesures par courant de transport plus traditionnelles et d'éviter les limites associées aux mesures par aimantation quasi statique QSFM («quasi-static field magnetization» en anglais). En effet, les mesures par courant de transport nécessitent l'usage de sources de courant spécialisées dont l'emploi peut être difficile en présence de forts champs magnétiques et à basse température, alors que les mesures QSFM sont actuellement limitées au cas où le champ est appliqué perpendiculairement par rapport à la surface des échantillons. Ces problèmes sont abordés à l'aide de deux objectifs, qui sont, premièrement, de développer une méthode QSFM qui permet de calculer $J_c(B, \theta)$ avec des champs magnétiques d'orientation arbitraire et, deuxièmement, de développer une méthode PFM pour calculer $J_c(B, T)$ en présence d'un champ magnétique perpendiculaire à la surface des échantillons. L'intention sous-jacente à la sélection de ces objectifs est de fournir une base pour la généralisation future des mesures PFM en présence de champ magnétique orienté arbitrairement.

En ce qui concerne le premier objectif, un modèle analytique basé sur le modèle de Bean est proposé pour le calcul de $J_c(B, \theta)$. Celui-ci suppose que J_c est anisotrope à cause d'effets dits «force-free» et peut prendre deux valeurs, soit J_{c1} et J_{c2}. Étant donné qu'il y a deux inconnus, la méthode repose sur la réalisation de deux mesures indépendantes pour chaque combinaison (B, θ) sondée. Les échantillons sont intentionnellement coupés de façon rectangulaire et l'indépendance des mesures est obtenue en tournant ces derniers de 90° autour d'un axe parallèle à leur vecteur normal. Des distributions $J_c(B, \theta)$ sont obtenues pour $0 \leq B \leq 9$ T et $\theta = 0°$, 15°, 30°, 45°, 55°, 65°, 75°, 80° et 85°. Une analyse sur l'erreur expérimentale est

présentée et la précision de la méthode est testée avec des données générées numériquement avec la méthode des éléments finis FEM («finite element method» en anglais). Une erreur inférieure à 5 % est obtenue.

En ce qui concerne le deuxième objectif, un algorithme calculant itérativement $J_c(B,T)$ et faisant usage d'un modèle FEM axisymétrique est proposé. Des mesures expérimentales et des simulations FEM basées sur une distribution $J_c(B,T)$ réelle (calculée par QSFM) sont faites de façon préliminaire pour mieux comprendre le comportement des échantillons soumis à des champs pulsés. Il en est déduit que le chauffage par induction et la présence de courants de Foucault dans les couches non supraconductrices des échantillons ne sont pas négligeables, et que la température peut être considérée comme uniforme dans ceux-ci. Le résultat du calcul fait par l'algorithme proposé est la courbe paramétrée $J_c(B(t),T(t))$ sur la surface critique $J \times B \times T$ du supraconducteur. Une analyse sur la convergence et l'erreur de l'algorithme est présentée et il est déterminé que, malgré l'usage de valeurs inexactes de l'exposant n dans l'équation constitutive $E-J$ en loi de puissance, la projection $(B(t),T(t))$ de la courbe paramétrée $J_c(B(t),T(t))$ est bien reproduite et qu'il est possible de borner J_c en se servant de valeurs minimales et maximales de n.

Ce mémoire se termine avec une discussion sur les améliorations qui devraient être faites à court terme pour valider plus rigoureusement les méthodes proposées et une discussion sur la généralisation des mesures PFM avec champ magnétique d'orientation arbitraire.

ABSTRACT

High-temperature superconductors (HTS) and, more specifically, rare earth barium copper oxide (REBCO) materials, are very promising for the development of future high-field magnets, as these materials generally have a very high critical current density J_c, critical temperature T_c, and critical magnetic field B_{c2}. That being said, REBCO J_c distributions have strong dependencies on the local magnetic field norm B, the magnetic field orientation described by the angle θ, and the temperature T. This makes the design of superconducting power devices quite challenging and knowing the $J_c(B, \theta, T)$ landscape of the conductors being used is crucial.

The focus of this work is on the development of a $J_c(B, \theta, T)$ measurement method for commercial REBCO tapes using pulsed field magnetization (PFM). The goal is to avoid the technical difficulties of traditional methods like transport current measurements and quasi-static field magnetization (QSFM) measurements, where the former necessitates the use of current sources that can be tricky during in-field and low temperature measurements and where the latter is presently only done in quasi-static fields perpendicular to the sample's surface. These are addressed with two research objectives, which are to develop a QSFM method for measurements in applied fields of arbitrary orientation, and to develop a measurement method to calculate $J_c(B, T)$ using PFM in fields perpendicular to the sample. The intention behind the selection of these goals is to provide a basis for the generalization and the development of PFM measurements in fields of arbitrary orientation.

For the first objective, a theoretical framework based on the Bean model is proposed for QSFM $J_c(B, \theta)$ calculations. The model assumes that J_c is anisotropic because of force-free effects and that it can take the values J_{c1} or J_{c2}. Since there are two unknowns, the proposed method hinges on making two independent measurements for every probed field and angle. Samples are intentionally chosen to be rectangular and independence between measurements is achieved by rotating the sample by 90° about its normal. $J_c(B, \theta)$ distributions are obtained for $0 \leq B \leq 9$ T and $\theta = 0°$, 15°, 30°, 45°, 55°, 65°, 75°, 80°, and 85°. An analysis on the error due to the experimental setup is done. The accuracy of the method is tested against numerically generated data with the finite element method (FEM) and a maximum error of 5% is found.

For the second objective, an algorithm demonstrated with an axisymmetric FEM model is proposed to iteratively calculate $J_c(B, T)$ from PFM measurements. Preliminary experimental and numerical measurements are done to study the behaviour of samples experiencing pulsed fields, where the superconducting layer is modelled with a realistic $J \times B \times T$ critical

surface calculated from QSFM measurements with a physical sample. It is confirmed that heating and screening currents in non-superconducting layers are non-negligible, but that temperature is uniform in the sample. The result of the calculation is the $J_c(B(t), T(t))$ path of the state of the sample on the $J \times B \times T$ critical surface. An analysis on the convergence of the algorithm and on the error caused by the choice of the n value is presented. It is determined that, despite erroneous n values, the $(B(t), T(t))$ path is still well reproduced by our algorithm and that using extrema of the expected n value can establish bounds on $J_c(B(t), T(t))$.

This thesis ends with a discussion on the short-term improvements that should be made to further validate and develop the methods proposed here and on their generalization to PFM measurements in fields of arbitrary direction.

TABLE OF CONTENTS

DEDICATION iii

ACKNOWLEDGEMENTS iv

RÉSUMÉ v

ABSTRACT vii

TABLE OF CONTENTS ix

LIST OF TABLES xii

LIST OF FIGURES xiii

LIST OF SYMBOLS AND ABBREVIATIONS xv

LIST OF APPENDICES xviii

CHAPTER 1 INTRODUCTION 1
1.1 Context 1
1.2 Problem of Interest 2
1.3 Research Objectives 3
1.4 Thesis Outline 4

CHAPTER 2 LITERATURE REVIEW 5
2.1 Properties of Superconducting Matter 5
2.1.1 Phenomenology and London Equations 5
2.1.2 Type I and Type II Superconductors 5
2.1.3 Dissipation Threshold for a Current in a Perpendicular Applied Field 7
2.1.4 Dissipation Threshold for a Current in a Parallel Applied Field 8
2.1.5 E-J Constitutive Equation 10
2.1.6 J_c Dependencies 12
2.2 Magnetization of Finite Samples 13
2.2.1 Relevant Phenomena 14
2.2.2 Critical State 16
2.2.3 Solutions to Known Problems 16

2.3 Critical Current Density Measurement Methods 20
2.3.1 Transport Current Method 20
2.3.2 Magnetization Method 22
2.4 Numerical Modelling 23

CHAPTER 3 CALCULATING J_c FROM QUASI-STATIC FIELD MAGNETIZATION MEASUREMENTS IN FIELDS OF ARBITRARY ORIENTATION 25
3.1 Analytical Method Derivation 25
3.1.1 Assumptions and Problem Setting 25
3.1.2 Problem Resolution 27
3.2 Experimental Trial 31
3.2.1 QSFM Method 31
3.2.2 Experimental QSFM Results and Discussion 33
3.2.3 Discussion on Experimental QSFM Results 37
3.3 QSFM Numerical Validation 40
3.3.1 Numerical Model Definition 40
3.3.2 QSFM Numerical Validation Results and Discussion 44
3.4 QSFM Generalization and Discussion 47
3.4.1 Generalization to Crystallographic Anisotropy 47
3.4.2 Interpretation of QSFM Results With Non-Ideal Samples 50

CHAPTER 4 CALCULATING J_c FROM PULSED FIELD MAGNETIZATION MEASUREMENTS IN PERPENDICULAR FIELDS 51
4.1 Preliminary Measurements 51
4.1.1 PFM Experimental Method 51
4.1.2 Preliminary Experiment Results and Takeaways 53
4.2 Algorithm Derivation for J_c Calculations with PFM 56
4.2.1 FEM Model Definition for PFM 56
4.2.2 Assumptions and Algorithm Presentation 58
4.3 Results Using Numerically Generated Reference Data 63
4.4 Discussion on PFM Results and Limitations 65
4.4.1 Mapping the $J \times B \times T$ Critical Surface 65
4.4.2 Error Due to the n Value Selection 66
4.4.3 Experimental Considerations for Future PFM Measurements 68

CHAPTER 5 PERSPECTIVES AND GENERALIZATION 71
5.1 Short-Term Improvements to QSFM and PFM 71

5.2 Generalization of QSFM and PFM to PFM in Fields of Arbitrary Orientation 72

CHAPTER 6 CONCLUSION 75
6.1 Summary of Contributions 75

REFERENCES 77

APPENDICES 85

LIST OF TABLES

Table 3.1 Parameters obtained from the fitting of J_{c1} data to equation (3.17). . 39
Table 3.2 QSFM simulation parameters. 44
Table 4.1 Preliminary simulation parameters. 58

LIST OF FIGURES

Figure 2.1 Generic phase diagrams for (a) type I and (b) type II superconductors for zero J. 6
Figure 2.2 Mixted state of type II superconductors. 7
Figure 2.3 Field distribution in the force-free state described by equations (2.7) and (2.8). 9
Figure 2.4 (a) Power law model for various n values. (b) Dissipation regimes within the power law model. 11
Figure 2.5 (a) Maximal Lorentz force configuration. (b) Force-free plane configuration. 13
Figure 2.6 (a) Qualitative M_r plot. (b) Qualitative M_i plot. 15
Figure 2.7 B_z and J_y distributions during the magnetization of virgin samples. . 18
Figure 2.8 The cross-section of a magnetized thin strip. 19
Figure 2.9 Qualitative representation of the magnetization in an orthorhombic sample, with the height of the "sandpile" representing the M component normal to the sample surface. 20
Figure 2.10 Illustration of existing I_c criteria. 21
Figure 3.1 (a) Elliptical sample tilted with respect to the applied field. (b) Rectangular sample tilted with respect to the applied field. 26
Figure 3.2 (a) Horizontal configuration C_h and (b) vertical configuration C_v. . . 27
Figure 3.3 Current configurations during QSFM. 28
Figure 3.4 Qualitative evolution of the Γ solutions with respect to the magnetic field. 31
Figure 3.5 Sample placement in the (a) horizontal configuration and in the (b) vertical configuration. (c) *In situ* wedge placement. Marked face of the sample on the 85° wedge in (d) C_h and (e) C_v. 32
Figure 3.6 QSFM magnetization data 34
Figure 3.7 J_{c1} and J_{c2} results computed from QSFM measurements. 36
Figure 3.8 Interpretation of $\Gamma \in \mathbb{C}$. 38
Figure 3.9 Comparison of J_{c1} and J_{c2} results to models from the literature. . . . 39
Figure 3.10 QSFM FEM model definition. 42
Figure 3.12 J colour plot at $B_a = 30$ T in (a) C_h and (b) C_v. 46
Figure 3.13 Numerical experiment results and accuracy assessment. 47
Figure 3.14 Current configurations in samples with crystallographic J_c anisotropy. 48

Figure 3.15	Current configurations in samples with crystallographic and force-free J_c anisotropy.	49
Figure 4.1	Qualitative magnetic probe	52
Figure 4.2	Samples and preliminary experimental results.	54
Figure 4.3	Model definition.	57
Figure 4.4	Preliminary numerical results.	59
Figure 4.5	Behaviour of the current profile and the normalized magnetic moment m_n	61
Figure 4.6	PFM algorithm results and performance.	64
Figure 4.7	Mapping of $J \times B \times T$ space.	66
Figure 4.8	PFM results with different n values.	67
Figure 4.9	PFM measurement altered by mechanical vibrations.	70
Figure 5.1	Simulated J colour plot at $B_a = 3$ T and $\theta = 80°$.	72
Figure 5.2	Normalized magnetic moment m_n half-hysteresis loops at $\theta = 80°$.	73
Figure A.1	Data correction process for m_h at $\theta = 75°$.	85
Figure B.1	m_z measurement in the horizontal configuration at $\theta = 88°$.	86
Figure C.1	Data correction process for m_h at $\theta = 85°$.	88

LIST OF SYMBOLS AND ABBREVIATIONS

$\mathbf{A}$	Vector potential (Vs/m)
abc	Crystal lattice axes
$\mathbf{B}$	Magnetic induction (T)
B_a	Applied magnetic field (T)
B_i	Padé approximant coefficients
B_{pk}	Peak field (T)
$B_{0\parallel,\perp}$	Kim model fitting parameter (T)
B_{sat}	Externally applied field at which the current reaches the centre of the sample (T)
C_h	Horizontal configuration
C_v	Vertical configuration
CSM	Critical state model
c_p	Heat capacity (J/(kgK))
d	sample thickness (m)
d_p	Average distance between pinning centres (m)
$\mathbf{E}$	Electric field (V/m)
E_c	Electrical field criterion (V/m)
EECSM	Extended elliptical critical state model
FEM	Finite element method
$\mathbf{F}_L$	Lorentz force (N/m)
$\mathbf{F}_p$	Pinning force (N/m)
f_p	Average pinning force per pinning centre (N/m)
$\mathbf{F}_v$	Viscous force (N/m)
$\mathbf{H}$	Magnetic field (A/m)
H_c	Critical magnetic field norm (A/m)
H_{c1}	First critical magnetic field norm (A/m)
H_{c2}	Second critical magnetic field norm (A/m)
HTS	High-temperature superconductor
I	Total current (A)
I_c	Critical current (A)
$\mathbf{J}$	Current density (A/m^2)
$\langle J \rangle$	Current density averaged over specified region (A/m^2)
J_c	Critical current density (A/m^2)

J_{c0}	Kim model fitting parameter (A/m^2)
$J_{c,\parallel}$	Critical current density parallel to the applied field (A/m^2)
$J_{c,\perp}$	Critical current density perpendicular to the applied field (A/m^2)
$J^*_{c,\parallel,\perp}$	Critical current density distributions used as simulation inputs (A/m^2)
$J_\parallel$	Current density component parallel to $\mathbf{B}$ (A/m^2)
$J_\perp$	Current density component perpendicular to $\mathbf{B}$ (A/m^2)
k	Anisotropy factor
L	Sample length (m)
LTS	Low-temperature superconductor
$\mathbf{M}$	Magnetization field (A/m)
M_i	Irreversible magnetization (A/m)
M_r	Reversible magnetization (A/m)
$\mathbf{m}$	Magnetic moment (Am^2)
m_{Cu}	Magnetic moment from Cu sample layers (Am^2)
m_{exp}	Experimental magnetic moment (Am^2)
m_h	Irreversible magnetic moment measured in C_h (Am^2)
m_{hast}	Magnetic moment from hastelloy sample layer (Am^2)
m_i	Irreversible magnetic moment contribution (Am^2)
m_n	Normalized magnetic moment (m^4)
m_r	Reversible magnetic moment contribution (Am^2)
m_v	Irreversible magnetic moment measured in C_h (Am^2)
n	Power law exponent
$\hat{\mathbf{n}}$	Unit normal vector
N_p	Pinning centre density (m^{-3})
OECSM	Original elliptical critical state model
P	Total dissipation (W)
p	Kim model fitting parameter
PFM	Pulsed field magnetization
QSFM	Quasi-static field magnetization
R	Outer radius (m)
r	Radius (m)
REBCO	Rare earth barium copper oxide
T	Temperature (K)
$\mathbf{T}_p$	Current potential (A/m)
$\langle T \rangle$	Temperature averaged over specified domain (K)
T_0	Initial temperature (K)

T_c	Critical temperature (K)
T_i	Padé approximant coefficients
t	Time (s)
t_0	Beginning time of a magnetic pulse (s)
t_e	End time of a magnetic pulse (s)
Δt	Pulse width (s)
V	Volume (m^3)
V_e	Electrostatic potential (V)
$\mathbf{v}_v$	Vortex velocity (m/s)
W	Sample width (m)
YBCO	$YBa_2Cu_3O_{7-\delta}$
α	Angle formed by the border between adjacent current partitions (rad)
β_a	Coefficient representing the vortex lattice arrangement
Γ	J_{c2}/J_{c1} ratio
γ	Geometric scaling factor
ϵ	Error (Am^2 or %)
λ_L	London penetration depth (m)
λ_{ab}	Ginzburg-Landau penetration depth along ab planes (m)
μ	Permeability
μ_0	Vacuum permeability (N/A^2)
ξ_{ab}	Ginzburg-Landau coherence length along ab planes (m)
$\eta_{\parallel}$	Parallel pinning efficiency
θ	Angle between $\mathbf{B}_a$ and $\hat{\mathbf{n}}$ (rad)
κ	Thermal conductivity (W/(mK))
Φ_0	Magnetic flux quantum (Wb)
ϕ	Magnetic scalar potential (A)
$\varphi_{\parallel}$	Angle between $\mathbf{B}$ and $\mathbf{J}$ in the force-free plane (rad)
$\varphi_{\perp}$	$\mathbf{B}$ angle around $\mathbf{J}$ (rad)
χ_m	Magnetic susceptibility
Ω_c	Conducting subdomain
Ω_{nc}	Non-conducting subdomain

LIST OF APPENDICES

Appendix A	Subtraction of Reversible Magnetization from QSFM Measurements .	85
Appendix B	QSFM Magnetization Data at 88°	86
Appendix C	Data Correction Methodology for QSFM measurements at 85°	87

CHAPTER 1 INTRODUCTION

1.1 Context

Superconductors are a class of materials that are known for being lossless electrical conductors at cryogenic temperatures and have fostered wide scientific interest in the last few decades. Several microscopic theories have been developed to describe the phenomenon of superconductivity, most notably the London model, the Bardeen-Cooper-Schreiffer theory, and the Ginzburg-Landau theory [1]. These models describe the physics of superconducting charge carriers and the thermodynamic properties of these materials, like the critical temperature, the critical current density, and the critical magnetic field, which are thermodynamic thresholds above which superconductivity is destroyed. Several applications have been found for these materials, namely, quantum computing, magnetometry with superconducting quantum interference devices, and many power applications.

At this moment, the most prominent power applications all make use of high field electromagnets [2]. These include magnets that are used for nuclear fusion, for particle accelerators, for magnetic resonance imaging (MRI), for nuclear magnetic resonance (NMR), in rotating machinery, etc. While superconducting electromagnets have been made for these applications for several decades, they are still being improved upon as conductor performance increases, where conductors have increased current carrying capacity over wider ranges of operating conditions. One of the common threads for the improvement of these devices is therefore increasing the maximum field produced and improving compactness, which can have a dramatic impact on performance. For instance, the power produced by nuclear fusion in a tokamak is proportional to B^4 [3].

The electrical conductors used in these applications are composite structures usually comprising a superconducting material and metals and/or alloys, where the superconductor is the main electrical conductor and the other components are used for mechanical support and thermal stability. The superconducting materials used can be separated into low-temperature superconductors (LTS), which must remain at temperatures below 30 K to retain their superconducting properties, and high-temperature superconductors (HTS), which have critical temperatures above 77 K. For electromagnets producing fields greater than $\sim$ 20 T, HTS coated conductors are preferred and usually seen as the only viable option, as they can operate at higher temperature, have higher operating currents, and better mechanical properties [2–4].

That being said, HTSs like REBCOs (rare earth barium copper oxides) have very anisotropic electrical properties because of their crystal lattice, which is composed of stacked atomic

planes of alternating composition [4–7]. As such, their critical current density varies strongly with temperature, the magnetic field norm, the magnetic field orientation, and mechanical strain. For example, when measuring the critical current density as a function of the orientation of the local magnetic field, it is usually the case that there is a sharp maximum when the local magnetic field is parallel to the *ab* planes of the crystal lattice. It is also usually the case that the critical current decays as temperature and magnetic field norm increase.

Considering that magnetic field norm and orientation are usually not uniform in electromagnets, having to take into account all of these dependencies makes the design process very challenging. In solenoid magnets, for instance, the orientation of the field changes along the length of the magnet bore, such that the critical current density is reduced near the top and bottom turns [8]. These regions become prone to hot-spots, where an occurrence is known as a "quench" and can cause irreversible damage to the conductor. This large critical current density variability also makes it challenging to compute the mechanical constraints induced by the Lorentz force that the conductors see. From an engineering perspective, it is therefore crucial to accurately know how the critical current density varies to be able to design electromagnets using HTSs like REBCO materials.

1.2 Problem of Interest

The dependencies of the critical current density that are the most important are the magnetic field norm, the magnetic field orientation, and temperature. The characterization of these dependencies is usually done with either transport current measurements or magnetization measurements [9]. Transport current measurements consist of measuring the voltage drop across a sample as current is passed through it, where the critical current is considered to be reached when a certain voltage criterion is met and the lossless property of the current is lost (this is discussed in more detail in section 2.3.1). While transport measurements are the most common, they present some downsides, especially when they have to be done in large fields and at low temperatures to simulate operating conditions [8]. In such conditions, the critical current density is very large and it is very difficult to fit current leads in the typically very restrained space that is available. The leads usually have to be a REBCO material as well, which poses a challenge as these are brittle and are hard to secure without breaking in the presence of large Lorentz forces. These measurements are also usually done in static fields, which are limited in amplitude and have to be ramped up slowly, making them very time-consuming.

On the other hand, quasi-static field magnetization (QSFM) measurements consist of placing the sample in a magnetic field and measuring its magnetic moment, from which the critical current density can be calculated with simple analytical formulas. This method has

the advantage of not needing a current source or a voltmeter but remains limited by the amplitude of the externally applied field, as the measurements are also done in static fields. This method is discussed in detail in section 2.3.2.

That being said, pulsed field magnetization measurements (PFM) are rarely used with superconductors and are usually not used for measuring the critical current density (e.g., irreversibility field measurements in [10, 11]). There is therefore an opportunity to develop a new measurement method that does not require a large current source and cumbersome current leads, and which allows experiments at higher fields. Indeed, while the highest achievable field is of 45.5 T in DC magnets [12], fields greater than 60 T are routinely produced in pulsed magnets from different institutions around the world [13–15].

1.3 Research Objectives

The long-term goal to which this work contributes is the development of a general method for characterizing the critical current density of commercial HTS tapes using pulsed field magnetization measurements (PFM). At the present moment, magnetization experiments used to determine the critical current density are done in quasi-static fields and only in the configuration where the sample is perpendicular to the applied field. Our goal is therefore to address these limits with the following sub-objectives:

1. Develop a new methodology for calculating the critical current density using QSFM measurements with fields of arbitrary orientation. As screening currents flow along closed loops that are concentric to the sample's perimeter, the local current necessarily experiences fields of varying orientation with respect to its own direction. The variation in magnetic field orientation therefore implicitly induces anisotropy in the critical current density and a method to deal with this scenario has never been published in the literature to the best of the author's knowledge.

2. Develop a new methodology for calculating the critical current density from PFM measurements in fields perpendicular to the sample. This is relevant as we expect there to be significant heating, screening currents in non-superconducting layers of the sample, and a non-uniform spatial distribution of the current density, making the use of analytical models very hard.

The underlying intention behind the selection of these sub-objectives is to provide a basis for further generalization of the method, i.e. calculating J_c using PFM in fields with arbitrary orientation.

1.4 Thesis Outline

Following chapter 1, the contents of this work are divided into five chapters. Chapter 2 goes over the relevant literature and set the theoretical basis for the following chapters. This includes a review of superconductor physics, theoretical solutions to common magnetization problems, and common critical current density measurement methods. Chapter 3 goes over our solution to the first sub-objective, where an analytical framework is presented, followed by experimental measurements and a preliminary numerical validation. Chapter 4 goes over the work that was done to address the second sub-objective, which includes preliminary experimental measurements and numerical simulations, the presentation of our critical current density calculation algorithm, followed by a discussion on the accuracy of our method and perspectives for physical measurements. Chapter 5 first discusses how the methods developed in chapters 3 and 4 can be more rigorously validated and improved upon, and then offers a preliminary discussion on the development of a true general PFM method. Finally, chapter 6 concludes this work by summarizing the contributions that were made.

CHAPTER 2 LITERATURE REVIEW

2.1 Properties of Superconducting Matter

2.1.1 Phenomenology and London Equations

The superconducting state is defined on a phenomenological level by the existence of two phenomena: zero resistivity seen by superconducting charge carriers in a direct current and the expulsion of any magnetic field from the superconducting volume, named the Meissner effect [1]. These effects are described empirically by the London equations, which are

$$\frac{\partial \mathbf{J}_{SC}}{\partial t} = \frac{1}{\mu_0 \lambda_L^2}\mathbf{E}, \tag{2.1}$$

$$\nabla \times \mathbf{J}_{SC} = -\frac{1}{\mu_0 \lambda_L^2}\mathbf{B}. \tag{2.2}$$

$\mathbf{J}$, $\mathbf{E}$, and $\mathbf{B}$ are the current density, the electric field, and the magnetic induction. The SC subscript indicates a superconducting current and will be dropped hereafter for the sake of readability. λ_L is the London penetration depth and μ_0 is the vacuum permeability. Equation (2.1) describes the zero resistivity property. Equation (2.2) indicates that screening currents emerge in the presence of a magnetic field and can be solved using Ampère's quasi-static equation. Equation (2.2) becomes

$$\nabla^2 \mathbf{B} = \frac{1}{\lambda_L^2}\mathbf{B}. \tag{2.3}$$

The solution to equation (2.3) is a decaying exponential function and λ_L is effectively the penetration depth of the field in the material volume.

2.1.2 Type I and Type II Superconductors

While the superconducting state itself is characterized by the previously mentioned phenomena, real materials can be separated into type I and II superconductors. The difference lies in the thermodynamic states that can exist in either one. The variables that generate the thermodynamic space are the temperature T, the current density norm J, and the magnetic field norm H (the orientation of H is discussed in forthcoming sections). Within this thermodynamic space, critical thresholds exist and delimit sharp transitions between states. These quantities are not independent and define a critical surface.

Type I superconductors are distinguished by an abrupt transition between the superconducting and the normal states. The critical thresholds are the critical temperature T_c, the

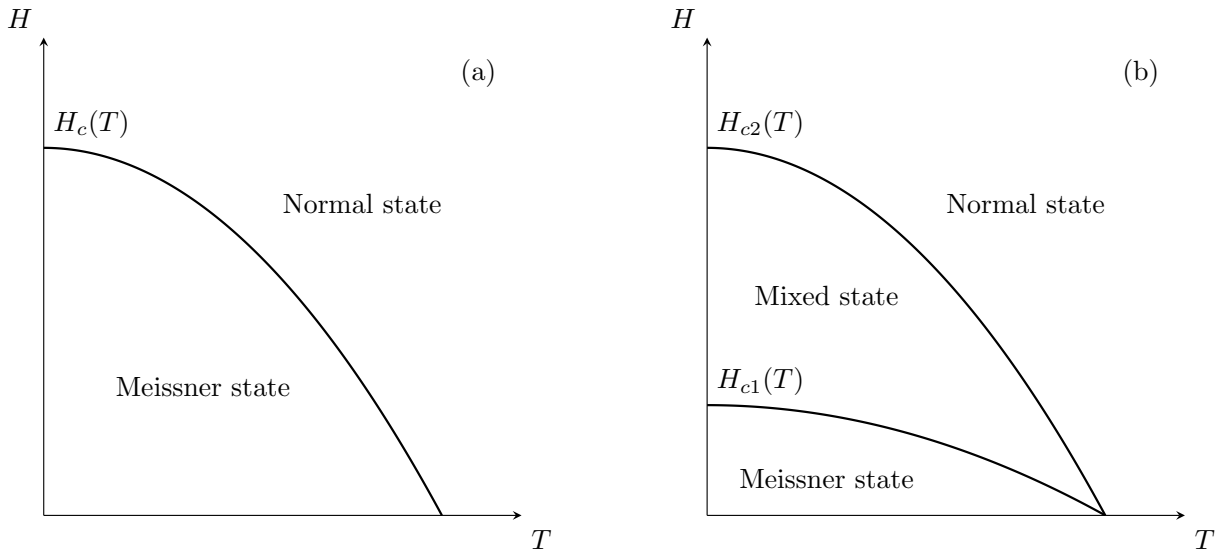


Figure 2.1 Generic phase diagrams for (a) type I and (b) type II superconductors for zero J.

critical magnetic field norm H_c, and the critical current density norm J_c. Figure 2.1 (a) shows a slice of a typical phase diagram at $J = 0$ for a type I superconductor. These materials are usually pure elements or metallic alloys such as aluminum, lead, mercury, NbTi, etc.

Type II superconductors distinguish themselves from type I superconductors by going through a mixed state between the normal and superconducting states. The critical thresholds for type II superconductors are, again, T_c, J_c, and the two critical fields, H_{c1} and H_{c2}. H_{c1} and H_{c2} respectively mark the transition between the entirely superconducting state (also known as the Meissner state) and the mixed state, and the transition between the mixed and the normal states (see figure 2.1 (b)). The mixed state itself is the composition of a superconducting volume containing small cylindrical regions in the normal state. A single normal region is called "vortex". Every vortex is at the centre of a screening supercurrent vortex, hence the name, and enables a quantum of magnetic flux (given by $\Phi_0 = hc/2e = 2.07{\cdot}10^{-15}$ Wb) to penetrate the material. Furthermore, these currents are responsible for the mutual repulsion between vortices, which causes them to organize themselves in a regular lattice (provided their movement is not impeded). Figure 2.2 shows a qualitative representation of the mixed state. A common kind of type II superconductor is, e.g., cuprate materials. These are formed by CuO planes separated by rare earth ions. Typical stoichiometries are e.g., $Bi_2Sr_2CaCu_2O_{8+x}$, $YBa_2Cu_3O_{7-\delta}$ (abbreviated YBCO), etc.

In this thesis, we solely work with type II superconductors. While the definition of J_c given above is the thermodynamic definition, where J_c is the current density that destroys the superconducting state, it is rarely used in practice. Instead, J_c is used to designate

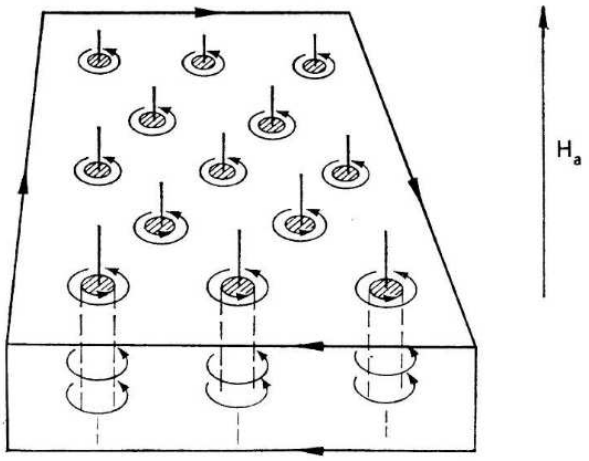


Figure 2.2 Mixed state of type II superconductors [16]. The arrows represent the supercurrents flowing within a λ_L distance of the material boundary and vortex edges.

the current density above which dissipation can be measured. From this point onward, the practical definition will be used. Let it also be noted that, hereafter, despite the microscopic inhomogeneities in type II materials, H, B, M, J, etc. will be used to designate macroscopic fields and quantities averaged over a distance larger than several vortex spacings.

2.1.3 Dissipation Threshold for a Current in a Perpendicular Applied Field

Let us once more consider the arrangement in figure 2.2, with the addition of a uniform transport current J perpendicular to the vortices and the applied field. The vortices experience a Lorentz force F_L given by

$$\mathbf{F}_L = \mathbf{J} \times \mathbf{\Phi}_0, \tag{2.4}$$

where $\mathbf{F}_L$ is a line force density in N/m. This force drives the vortices to move perpendicularly to the current direction and the magnetic flux lines. Additionally, vortices are subject to pinning forces created by defects in the material. These can be dislocations, inclusions, artificial pinning centres, etc. in the crystal lattice, which create potential wells that can trap the vortices. This means that the vortices remain fixed in place for small currents and only begin moving once J reaches some threshold value $J_{c\perp}$ that enables them to overcome these potential wells. Once vortices are in motion, they are subject to viscous forces and move at constant speed [17, 18]. While constant speed implies that the sum of the forces on individual vortices is zero, there still remains a nonzero $\mathbf{v}_v \times \mathbf{B}$ term ($\mathbf{v}_v$ being the vortex velocity) that produces a force not cancelled out by the pinning and viscous forces. It then

follows that the electric field $\mathbf{E}$ cannot be zero if there is no other Lorentz force (or any other force) contributions in the system. This electric field is given by

$$\mathbf{E} = \mathbf{B} \times \mathbf{v}. \tag{2.5}$$

This field is parallel to the transport current direction and the total dissipation P is given by:

$$P = \int_V \mathbf{J} \cdot \mathbf{E} \, \mathrm{d}^3 r, \tag{2.6}$$

where V is the material volume. Looking at this from a more macroscopic perspective, the energy required to generate the electric field has to be supplied by the current source [19].

2.1.4 Dissipation Threshold for a Current in a Parallel Applied Field

Considering the dissipation mechanism for transport currents transverse to the applied field, one could wonder: what happens when the macroscopic transport current is parallel to the applied magnetic field? Indeed, the arguments from the last section do not apply as it would seem that the vortices are parallel to $\mathbf{J}$, which implies that $\mathbf{F}_L$ from equation (2.4) is zero. The motion of flux lines and dissipation in this configuration, named the "force-free" configuration, have been studied for decades, yet there is no consensus in the community on what the microscopic mechanisms involved are. Matsushita presents a detailed review of the literature in [20] and this section highlights the important points that are made.

A common experiment used to study this configuration consists of placing a cylinder or tape in a field parallel to the sample longitudinal direction and then applying a transport current in the same direction. Some effects that are observed in such experiments are:

1. An initial diamagnetic magnetization in the longitudinal direction of the sample, followed by a paramagnetic response [21].

2. A critical current density $J_{c\parallel}$ much larger than $J_{c\perp}$. Reference [22] presents data as a function of applied field magnitude for NbTi wires. Reference [23] presents data as a function of external magnetic field orientation for YBCO samples.

3. An electric field that does not respect equation (2.5) [24].

A simple model is proposed in [25] to explain some of these results. The initial assumption is that the local current density is parallel to the local magnetic field. This force-free condition can be expressed with:

$$\mathbf{J} \times \mathbf{B} = \mathbf{0}, \tag{2.7}$$

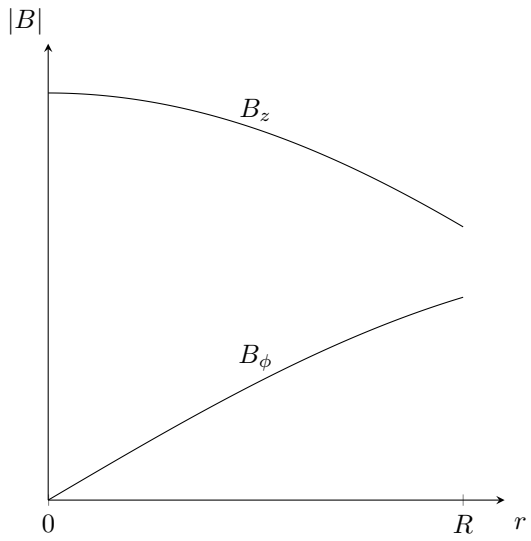


Figure 2.3 Field distribution in the force-free state described by equations (2.7) and (2.8). Adapted from [20].

$$\mathbf{J} = \frac{\alpha_f}{\mu_0}\mathbf{B}, \tag{2.8}$$

where α_f is a scalar function of $\mathbf{B}$. Matsushita makes the approximation that α_f is constant at low fields. Assuming the sample to be a cylinder of radius R and infinite along $\hat{\mathbf{z}}$ in an applied field $\mathbf{B}_a = B_a\hat{\mathbf{z}}$, the solution is given by:

$$B_z = \frac{\mu_0 I}{2\pi R}\frac{J_0(\alpha_f r)}{J_1(\alpha_f R)}, \quad B_\phi = \frac{\mu_0 I}{2\pi R}\frac{J_1(\alpha_f r)}{J_1(\alpha_f R)}, \tag{2.9}$$

where the J_i are Bessel functions of the first kind of i^{th} order and I is the total current. As can be seen in figure 2.3, the solution reproduces the paramagnetic behaviour observed in experiment, as $B_z(r) > B_z(R)$. That being said, an obvious flaw of the model is the prediction of an infinite critical current in superconductors without pinning centres, which evidently does not reproduce experiment. This is so because no work is done on the vortices. Considering this, one could estimate that, while this description is not complete, the system is in a state close to the one given by equations (2.7) and (2.8).

The two main propositions regarding the underlying microscopic mechanisms of force-free dissipation are flux cutting and the rotational shearing of the vortex lattice (as opposed to translation in the perpendicular configuration). The former was first proposed by Cave *et al.* [24] and assumes the critical condition is set by the cutting and recombining of flux lines as they enter the material at different angles and are compressed together. Several authors have made predictions for the value of J_c [24, 26–28], but these overshoot experimental ones

by several orders of magnitude. For instance, using NbTa and the results derived by Brandt *et al.* [28], a critical current density of $\sim 10^{12}$ A/m^2 at $B/\mu_0 H_{c2} = 0.7$ is obtained, which is orders of magnitude larger than the experimental result of $\sim 10^7$ A/m^2 for a sample with weak pinning [20].

The latter proposition of flux lattice shearing was made by Matsushita. Using Ampère's law as a starting point, he pointed out that a current with a force-free component induces a rotational shear in the flux line lattice. One can see this as a consequence of the superposition of the externally applied field and the additional perpendicular self-field produced by the transport current. This changes the nature of vortex motion, and in turn, changes the effect of pinning. Matsushita and Kiuchi [29] therefore suggested that the critical condition is met when the torque driving the shear of the vortex lattice is in equilibrium with an opposed pinning torque and find that $J_{c\parallel}$ is given by

$$J_{c\parallel} = 6\eta_{\parallel}\frac{N_p f_p d_p}{B a_f}, \tag{2.10}$$

with $\eta_{\parallel}$ the parallel pinning efficiency, N_p the pinning centre density, f_p the average pinning force per pinning centre, and d_p the average distance between pinning centres. Results from [30] show that $J_{c\parallel}$ is proportional to the product $N_p f_p d_p$, which supports the hypothesis that pinning still determines the critical condition.

That being said, research on the force-free configuration has not attracted much attention in recent years. While the notion of force-free effects is important for the contents of this work, the microscopic details are not relevant as the models we present are macroscopic in nature. We therefore keep this discussion as a basis for intuition for what follows.

2.1.5 E-J Constitutive Equation

To solve Maxwell's equations, a constitutive E-J equation is required. To reproduce the very nonlinear E-J characteristic of superconductors, several models have been proposed. The most common are the Bean [31, 32] and power law [33, 34] models. The Bean model states that

$$\mathbf{J} = \begin{cases} 0, & \text{if } E = 0 \\ J_c \dfrac{\mathbf{E}}{E}, & \text{if } E > 0 \end{cases}, \tag{2.11}$$

and provides a basis for the critical state model (CSM) that is discussed in section 2.2.2, which often provides the only possibility for an analytical solution, even for simple problems. In equation (2.11), Bean originally made the assumption that J_c is independent of the local field. This approximation is valid only for fields that are very weak with respect to H_{c2}. The

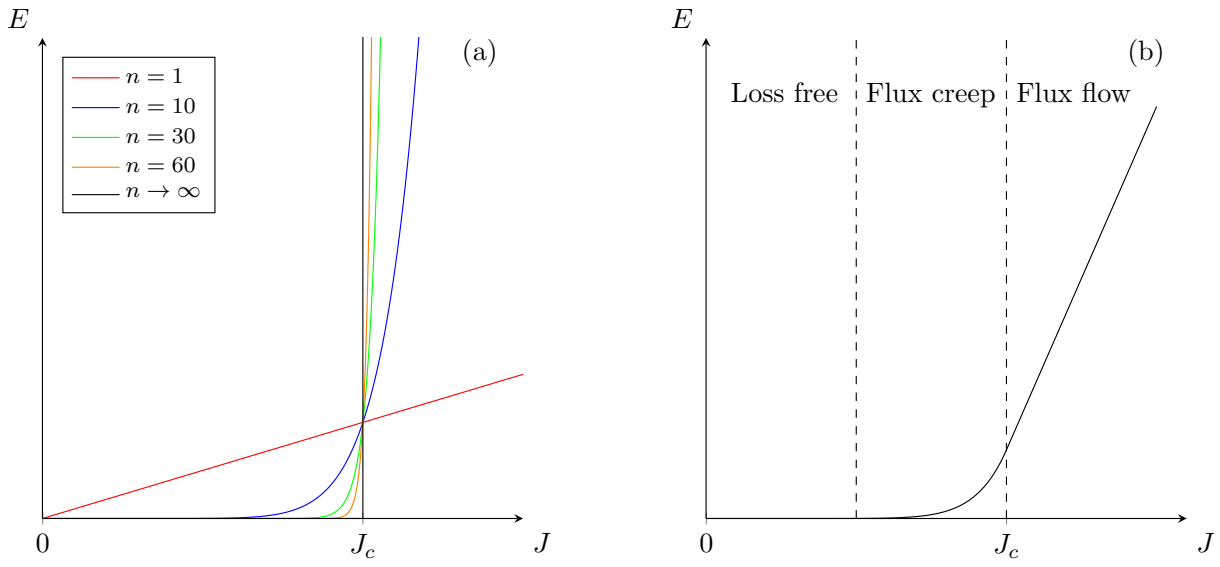


Figure 2.4 (a) Power law model for various n values. $n = 1$ is the resistive limit and $n \to \infty$ is the Bean limit. (b) Dissipation regimes within the power law model.

black curve in figure 2.4 (a) gives a qualitative representation.

In cases where the Bean model does not apply, a more accurate constitutive law is required. As shown in figure 2.4 (b), one can distinguish between three regimes. The lossless regime corresponds to the region of the E-J characteristic where the vortices remain trapped in their pinning centres and resistance is zero, while the flux flow regime corresponds to the region of constant resistance where the vortices are dislodged from their pinning sites by the Lorentz force, as discussed in section 2.1.3. The flux creep regime bridges the gap between the two previous ones and is described microscopically by the Anderson-Kim theory [17,18]. In short, flux creep becomes significant when the pinning force is weak compared to the thermal energy that the vortices carry, enabling them to jump between pinning sites. While the probability of successful jumps is low and the average vortex motion is zero at equilibrium, the presence of a current induces a bias in the potential landscape and the associated Lorentz force contributes to an increased jump probability in a given direction. The average vortex motion is therefore nonzero and contributes to resistance in the conductor. One can see in figure 2.4 (b) that this triggers the onset of resistance for $J < J_c$. The sum of these phenomena results in a smooth but sharp nonlinear E-J curve. This has been observed experimentally by several authors [34–38] and is most commonly described with the empirical power law model, given by

$$E = E_c \left(\frac{J}{J_c} \right)^n , \tag{2.12}$$

with E_c the electric field criterion (discussed in section 2.3.1) and n the power law exponent, generally a function of B and T. One can notice that by changing the n value, equation (2.12) reproduces the limiting cases, where $n \to \infty$ is the same as the Bean model and $n = 1$ yields a constitutive relation of ohmic form (see figure 2.4 (a)). It can also be said that equation (2.12) is only valid for isotropic materials but can be generalized into tensor form.

2.1.6 J_c Dependencies

Up to this point, the assumption was made that the magnetic field norm, the magnetic field orientation, and temperature were constant. To intuitively deduce the behaviour of J_c as a function of the magnetic field, one can use equation (2.4) as a starting point. When the field amplitude increases, the Lorentz force does so as well and the required current for the vortices to escape pinning centres is lower. In other words, J_c tends to decrease as B increases. To model this, several empirical analytical models exist, with the most well-known being the Kim model

$$J_c(B) = \frac{J_{c0}}{1 + B/B_0}, \tag{2.13}$$

where J_{c0} and B_0 are fitting parameters. More nuanced models exist for anisotropic cases, e.g., when REBCO materials are involved, for which J_c varies significantly depending on whether the current flows along the *ab* planes or along the *c* axis. One such model is proposed by Gömöry *et al.* [39] for the situation illustrated in figure 2.5 (a). J_c reads

$$J_c = J_{c0}\left(1 + \frac{\sqrt{k^2 B_\parallel^2 + B_\perp^2}}{B_0}\right)^{-\beta}, \tag{2.14}$$

where J_{c0} and B_0 are the same as in equation (2.13), $B_\parallel$ ($B_\perp$) is the field component parallel (normal) to the *ab* planes, $k < 1$ is a factor representing anisotropy, and β is an extra fitting parameter. We define $\varphi_\perp$ made by $B_\parallel$ and $B_\perp$, which is used later on.

In the force-free plane shown in figure 2.5 (b), similar models exist. Clem *et al.* provided a review of these models in [40] and reported that the extended elliptical critical state model (EECSM), based on the original elliptical critical state model [41–43], describes experiments more accurately. In a scenario where there is an angle $\varphi_\parallel$ between $\mathbf{B}$ and $\mathbf{J}$, J_c is constrained such that

$$\frac{1}{J_C^2} = \frac{\sin^2\varphi_\parallel}{J_{C\parallel}^2} + \frac{\cos^2\varphi_\parallel}{J_{C\perp}^2}. \tag{2.15}$$

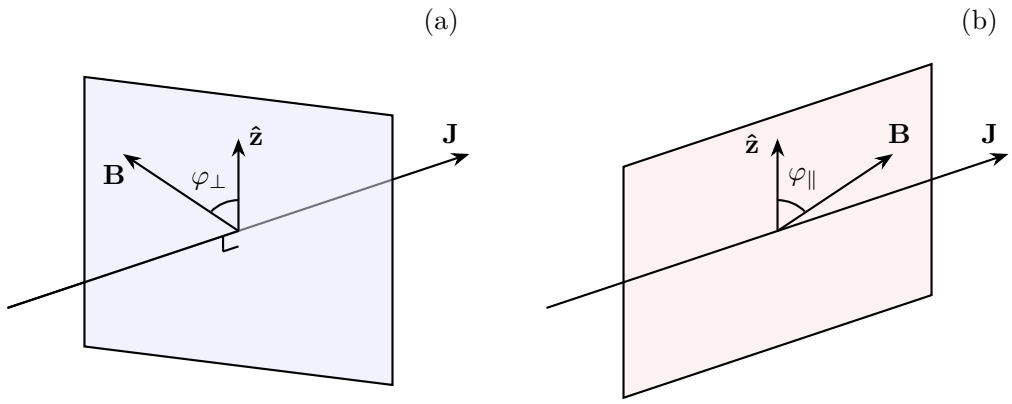


Figure 2.5 (a) Maximal Lorentz force configuration, where **B** and $\hat{\mathbf{z}}$ are contained in the shaded plane and **J** is normal to it. (b) Force-free plane configuration, where **B**, $\hat{\mathbf{z}}$, and **J** are all contained in the shaded plane.

The electric field is related to the current such that

$$E_\parallel = \rho_\parallel J_\parallel, \quad E_\perp = \rho_\perp J_\perp, \tag{2.16}$$

with the subscript $\parallel$ ($\perp$) describing vector components parallel (perpendicular) to **H** and $\rho_\parallel$ and $\rho_\perp$ are nonlinear functions representing the resistivity (see [40] for more details).

The effect of temperature on J_c can be deduced intuitively by considering its effect on flux creep. As temperature rises, vortex thermal agitation is accentuated and flux creep is more prominent. As the norm of the Lorentz force necessary to dislodge vortices becomes smaller, it follows that J_c decreases as temperature rises. While sophisticated empirical models describing $J_c(T)$ are not common, simple linear estimations can be used. For instance, the model

$$J_c(T) = J_{c0}\frac{T_c - T}{T_c - T_0} \tag{2.17}$$

is used in [44], with T_0 being the initial temperature in a transient scenario.

2.2 Magnetization of Finite Samples

Magnetization experiments consist in placing a sample in a magnetic field, either static or time varying, to observe its response. This can be done for example to measure magnetic susceptibility, the saturation field, the hysteretic behaviour of a given material or sample, etc. For superconductors, magnetization experiments are usually done to determine the critical current density from the magnetic moment, study the behaviour of vortices, and determine losses during AC operation. The literature pertaining to these experiments is abundant and

several theoretical and experimental results are reported. The following section goes over the ones that are relevant to this work.

2.2.1 Relevant Phenomena

Magnetization in superconducting matter can be divided into reversible and irreversible contributions, where a reversible behaviour implies that magnetization is only a function of the present field and an irreversible behaviour implies that magnetization is a function of the present field and the magnetic history of the sample being used. Looking at $M(H)$ plots, reversible magnetization results in a single-valued $M(H)$ curve, while irreversible magnetization leads to a hysteretic $M(H)$ curve (see figure 2.6).

The reversible magnetization M_r in superconductors in essentially due to the Meissner effect, which is caused by supercurrents circulating within a λ_L distance of the boundary of matter in the superconducting phase (recall that the volume occupied by vortices is in the normal phase). For type I materials below H_c and type II materials below H_{c1}, this boundary is composed of the sample's outside edges since there are no vortices. In this regime, the volumic fraction where the outside field is screened is constant, which results in $M_r = -H$. In type II materials between H_{c1} and H_{c2}, the boundary is composed of the sample's outside edges and the vortex interfaces. This implies that, as the outside field is increased and vortices move into the material, the volumic fraction of the sample that is screened decreases. The $M_r(H)$ curve therefore has a positive slope between H_{c1} and H_{c2} until H_{c2} is reached and superconductivity is destroyed. Typical $M_r(H)$ curves for type II materials with different Ginzburg-Landau parameters κ are shown in figure 2.6 (a). Several models have been published to calculate $M_r(H)$ between H_{c1} and H_{c2}, for instance in [45,46]. In the article where the existence of the mixed state is demonstrated [47], Abrikosov proposes that for field regimes near H_{c2},

$$M_r = \frac{H - H_{c2}(T)}{(2\kappa^2 - 1)\beta_A}, \tag{2.18}$$

where β_A is a parameter close to unity dependent on the arrangement of the vortex lattice. One can see from equation (2.18) that κ dictates the relative importance of M_r. Using the Ginzburg-Landau penetration depth $\lambda_{ab} = 89$ nm (analog to λ_L) and the coherence length $\xi_{ab} = 1.2$ nm (with the subscript $_{ab}$ indicating the direction parallel to ab planes) for YBCO [48], one can find $\kappa^2 = (\lambda_{ab}/\xi_{ab})^2 \approx 5500$ and it is obvious that M_r is small compared to H. Since the material of interest for this work is YBCO, M_r will be neglected for the time being. Let it be noted, however, that this approximation is not warranted for all materials [49,50].

Irreversible magnetization M_i in type II superconductors originates from the induction of

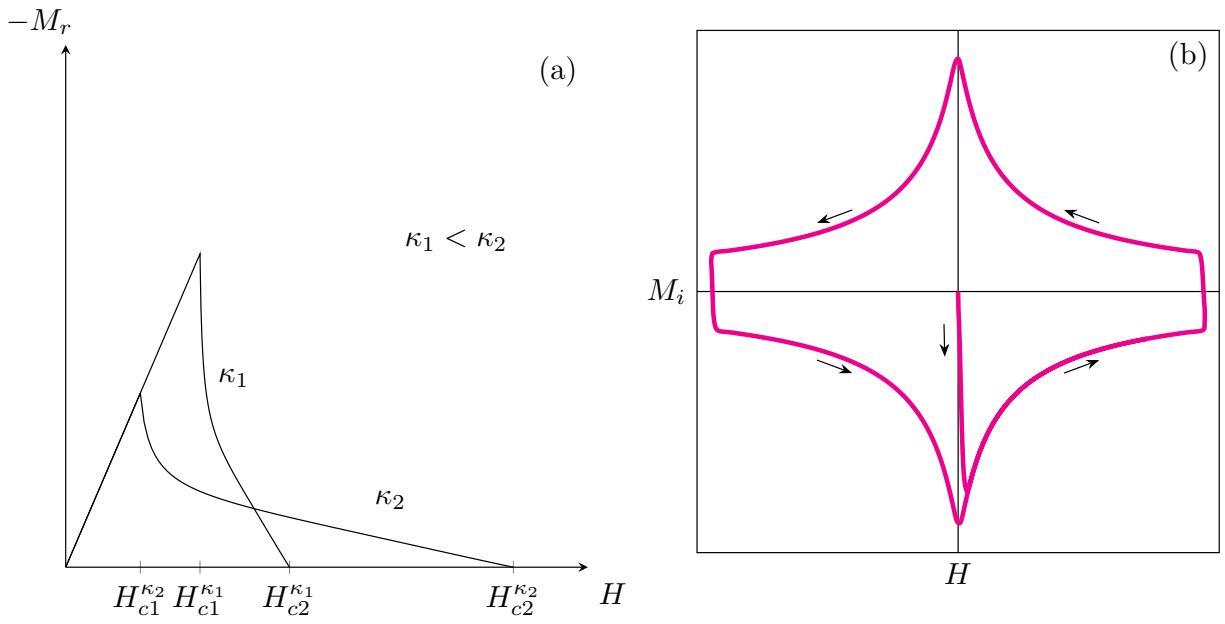


Figure 2.6 (a) Qualitative M_r plot. (b) Qualitative M_i plot. The arrows indicate the orientation of the path taken by M_i during the magnetization of a virgin sample in an oscillating field.

screening currents that are not attached to individual vortices. The irreversibility of M_i arises from the fact that, as the applied field is ramped and vortices enter the sample, dissipation occurs and energy is lost as heat (recall sections 2.1.3 and 2.1.4). This is different from reversible magnetization, where the magnetic field screening is done by lossless Meissner currents. Walking through the stages of the magnetization of a sample can help derive some properties of $M_i(H)$ (see figure 2.6 (b)). Let there be a virgin sample (i.e. with no magnetic history) that was cooled below T_c with no field present and then exposed to an oscillating applied magnetic field. From Ampère's law, it can be seen that induced currents emerge at the edges of the sample and permeate it until they reach the centre. This current saturation process corresponds to the initial slope starting at the origin and ending once it reaches the major hysteresis cycle. As the field is ramped up further, the magnitude of M_i decreases since J_c is more or less inversely proportional to H (assuming $J_c(B)$ follows the Kim model). When the sign of $\partial H/\partial t$ is reversed, the direction of the induced currents, and hence the direction of M_i, are also reversed. As the applied field oscillates, M_i moves along the major hysteresis cycle in the direction of the arrows displayed in figure 2.6 (b). Of particular importance is the fact that since M_i originates from screening currents, the top and bottom branches of the hysteresis cycle mirror each other with respect to the abscissae axis. This property will be exploited later in this work to separate M_r and M_i.

2.2.2 Critical State

The critical state describes the state in which the vortex lattice is when all forces acting on it are in equilibrium (see section 2.1.3 for a discussion on the forces involved). With F_L the Lorentz force, F_p the pinning force, and F_v the viscous force, the analytical definition of the critical state reads [20]

$$\mathbf{F}_L + \mathbf{F}_p + \mathbf{F}_v = \mathbf{0}. \tag{2.19}$$

The most commonly studied case is the one of a static field and is considered here. This implies that the vortex lattice is frozen in place and F_v is null. Considering this and using the Lorentz force expression, equation (2.19) can be reduced to [1]

$$\mathbf{B} \times \mathbf{J} = \mathbf{F_p}. \tag{2.20}$$

With a uniform F_p and using Ampère's law, equation (2.20) can be further reduced to [51]

$$\|\nabla \times \mathbf{B}\| = \frac{\mu_0 F_p}{B} = J_c \tag{2.21}$$

when B is perpendicular to J. In equation (2.21), J can be set to J_c since the equilibrium condition $F_L = F_p$ is the dissipation threshold that corresponds to J_c.

That being said, the critical state assumption is only valid in situations where field variations are substantial enough for the vortex motion to be irreversible, i.e. when vortices jump between pinning sites. Indeed, the microscopic action of a pinning centre can be described as a smooth quadratic potential in which the vortices can move reversibly, provided they remain in the same pinning site [20]. This situation is not compatible with the assumption of total irreversibility and the critical state model is not well suited to describe it.

2.2.3 Solutions to Known Problems

Magnetization experiments with superconductors have been done for decades and several papers present analytical solutions for the current and field distributions as well as the $M_i(H)$ curve for several sample geometries, field orientations, and approximation regimes. The equation that is usually solved is Ampère's law

$$\nabla \times \mathbf{B} = \begin{pmatrix} \partial_y B_z - \partial_z B_y \\ \partial_z B_x - \partial_x B_z \\ \partial_x B_y - \partial_y B_x \end{pmatrix} = \mu_0 \mathbf{J} = \mu_0 \begin{pmatrix} J_x \\ J_y \\ J_z \end{pmatrix} \tag{2.22}$$

with ∂_i the Einstein notation of the partial derivative. When the critical state hypothesis is valid, the constraint $(J_x^2 + J_y^2 + J_z^2)^{1/2} = J_c$ is enforced and equations (2.21) and (2.22) are

equivalent.

In order to have an analytical solution, many authors frame problems such that the current has only one nonzero component, say J_y. Equation (2.22) is reduced to

$$\partial_z B_x - \partial_x B_z = \mu_0 J_y. \tag{2.23}$$

This corresponds in a general manner to situations with geometries infinite in the y direction, such as infinite slabs, infinite strips, etc. and the applied field B_a lying in the xz plane. The simplest case is the one where $\mathbf{B}_a = B_a\hat{\mathbf{z}}$ and where the sample has a rectangular cross-section with edges parallel to $\hat{\mathbf{x}}$ and $\hat{\mathbf{z}}$, which is discussed first. In this configuration, the separate terms of equation (2.23) can be given a simple interpretation. This is discussed at length in [53, 54]. The first, $\partial_z B_x$, represents the horizontal bending of flux lines that would be parallel to $\hat{\mathbf{z}}$ without the sample's magnetic response and is representative of the demagnetizing field. The second, $\partial_x B_z$, represents the flux line density gradient across the sample width, which is indicative of the local vortex density. Numerical and experimental studies [53–55] show that one or the other of these terms can be neglected in the right circumstances.

The simplest case is that of the well-known infinite slab parallel to the yz plane, where $\partial_z B_x$ must be zero by symmetry, and because the virtual magnetic charges generating the demagnetizing field are displaced to $|z| \to \infty$. Figures 2.7 (a) and 2.7 (b) show generic B and J distributions across a slab of width $2W$ during its magnetization from a virgin state.

This is not true for thin geometries at low fields. Let there be a thin geometry of thickness d along $\hat{\mathbf{z}}$, where one can imagine a ribbon or strip infinite along $\hat{\mathbf{y}}$ and parallel to the xy plane. The tangential field boundary condition on the top and bottom surfaces is $H_x(d/2) = -H_x(-d/2)$ and must be accommodated over a very small thickness. Combined with the fact that flux has yet to substantially penetrate the sample, the ratio $\partial_z B_x/\partial_x B_z$ becomes quite high and $\partial_x B_z$ can be dropped from equation (2.23). Theuss *et al.* [53] estimated that this ratio is of about the order of the radius/thickness for thin cylindrical samples, which gives an order of magnitude of 1000 for a radius of 1 mm and a thickness of 1 µm. Figures 2.7 (c) and 2.7 (d) show qualitative B and J distributions for this geometry during its magnetization from a virgin state. One can notice the pronounced difference with the slab geometry in the B_z profile at the edges, where the applied field is amplified, and in the J distribution at the centre of the sample, where the current is not zero. Zeldov *et al.* [52] interpret this current to be a screening current resulting from the field discontinuity between the top and bottom surfaces, which in turn flows across the whole thickness (as opposed to within a London penetration depth of the edges). Analytical solutions in this regime are derived for various

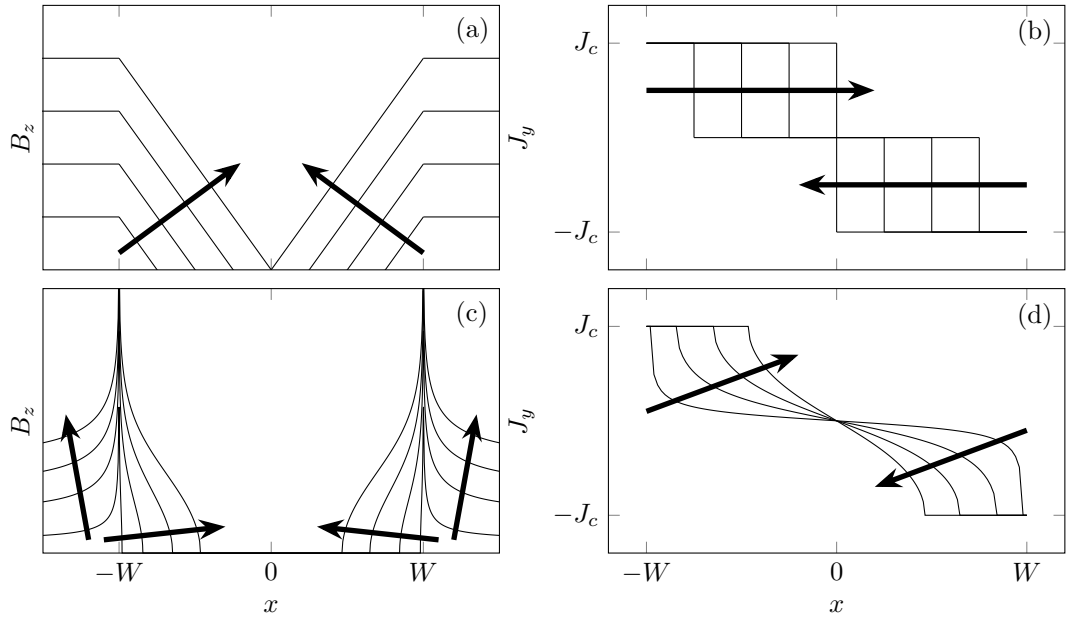


Figure 2.7 B_z and J_y distributions during the magnetization of virgin samples. (a) and (b): slab geometry with $B_a/B_p = 0.25$, 0.50, 0.75, and 1 along the arrow directions. B_p is defined as the B_a value necessary for B_z to permeate the sample entirely. (c) and (d): thin strip geometry with $B_a/B_f = 0.71$, 1, 1.67, and 5 along the arrow directions. B_f is the characteristic field for thin strip geometries. Adapted from [52].

applied fields and transport current scenarios in [52, 56, 57].

That being said, the dominance of terms is reversed at high fields. As vortices reach the centre of the sample, the magnetization current response is saturated and becomes weak compared to B_a. The flux lines straighten and samples like thin infinite strips behave like infinite slabs. Connor and Malozemoff [55] found that, at low fields, the self-field maximum is $\approx J_c d$ and $\partial_x B_z$ starts to dominate for applied fields beyond this threshold. Evaluating this expression with values $J_c = 10^{11}$ A/m^2 and $d = 1$ µm yields a threshold of 125 mT. In this regime, Ampère's law can be solved while dropping $\partial_z B_x$. Going forward, let us call these resolution regimes the low- and high-field regimes respectively.

Another relevant result was obtained by Zhukov *et al.* [58] for infinitely long thin strips along $\hat{\mathbf{y}}$ magnetized by a field with an arbitrary angle θ inside the xz plane, while assuming that the Bean model is valid, as shown in figure 2.8. The cross-section of the thin strips are characterized by a width W and a thickness d. It is argued that at high fields, the vortices are roughly parallel to B_a and are not normal to the sample surface if B_a has an arbitrary orientation (see figure 2.8 (a)). Assuming that $\mathbf{J} = \pm J_c \hat{\mathbf{y}}$ as in a slab, one can partition the current parallel and antiparallel to $\hat{\mathbf{y}}$ in the cross-section as shown in figure 2.8 (b), with the

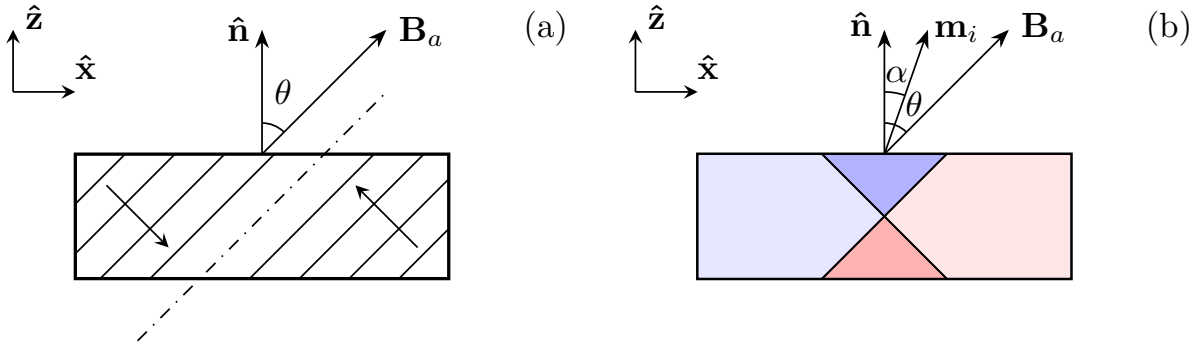


Figure 2.8 The cross-section of a magnetized thin strip. (a) Flux motion in the thin strip cross-section. The vortices are represented by the straight tilted lines and move along the arrow directions. The dash-dotted line represents the plane along which the vortices entering from both sides of the sample meet. (b) Current partitions in the cross-section. Blue (red) shading represents current going into (out of) the page. Adapted from [58].

blue (red) shaded regions having a current going into (out of) the page. From symmetry, one can see that the two zones with darker shading only contribute to m_x and that the two zones with lighter shading only contribute to m_z (this is valid for $\theta \leq \tan^{-1}(W/d)$ and $\theta \geq \tan^{-1}(W/d)$, i.e. for θ smaller and larger than the angle made by the diagonals of the cross-section). The angle α formed by m_x and m_z is given by equations 3 and 6 in [58]. Evaluating either at $\theta_c = \tan^{-1}(W/d)$ (where θ_c is the angle made by the diagonals of the cross-section) yields $\alpha = \tan^{-1}(d/W)$. For $W = 1$ mm and $d = 1$ µm, $\theta_c = 89.94°$ and $\alpha = 0.0573°$. The important conclusion here is that for samples with high aspect ratios, the resulting magnetic moment $\mathbf{m}$ is locked to the sample's normal for essentially the whole angular range of applied fields, and the orientation of m abruptly rotates by $\pi/2$ only once B_a is very close to parallel to the sample's surface. Zhukov *et al.* also derived α while assuming a power law E-J constitutive equation. They have found that very little changes between the ohmic ($n = 1$) and Bean ($n \to \infty$) limits, and therefore argue that the geometrical locking of m is relatively insensitive to the chosen constitutive law.

The last result that is discussed was published in [59] by Gyorgy *et al.* and deals with the magnetization of anisotropic samples. An expression is derived for the difference between the top and bottom branches $\Delta M = 2\langle M_i \rangle$ of a magnetization cycle using equation (2.21), while assuming that the high field regime is valid ($\langle \cdots \rangle$ is used for averaged quantities). Anisotropy is modelled by having separate critical currents, J_{c1} and J_{c2}, for different current flow directions. Visualizing M_i plotted against the x and y spacial coordinates, one gets a volume resembling an elongated pyramid, as shown in figure 2.9, for orthorhombic samples

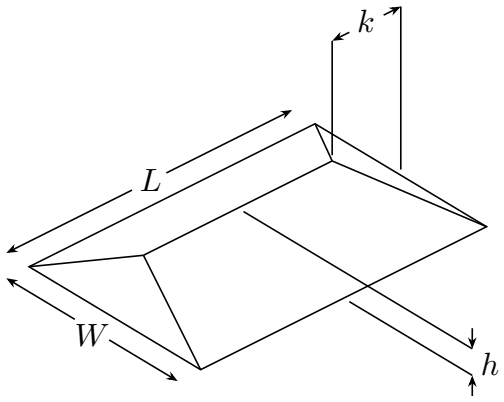


Figure 2.9 Qualitative representation of the magnetization in an orthorhombic sample, with the height of the "sandpile" representing the M component normal to the sample surface. Adapted from [59].

like the ones used by Gyorgy *et al.* Campbell and Evetts mentioned in [51] that the critical state equation is equivalent to that giving the height of a pile of sand standing on a given surface. $\langle M_i \rangle$ is therefore obtained by calculating the volume of the "magnetization pyramid" and dividing by the area. To avoid having the pseudo-width k and height h (with units respectfully in m and in A/m) in the final equations, one can use $2h/W = J_{c1}$ and $h/k = J_{c2}$ to get

$$\Delta M = \frac{W J_{c1}}{2}\left(1 - \frac{W J_{c1}}{3 L J_{c2}}\right), \tag{2.24}$$

with h, k, L, and W defined in figure 2.9. One can notice that this result is independent of the sample thickness (recall that the high field regime is valid and that the sample behaves like an infinite geometry).

2.3 Critical Current Density Measurement Methods

This section goes over the most common existing methods for measuring J_c in superconducting samples. The two main types of measurement are transport current and magnetization current measurements.

2.3.1 Transport Current Method

Transport current measurements consist in measuring continuous current-voltage curves by ramping an applied current I through a sample and reading the voltage drop V across its length [9]. A typical measurement curve is shown in figure 2.10. As the current is ramped up from zero, the sample goes through the regimes discussed in section 2.1.5, which are the

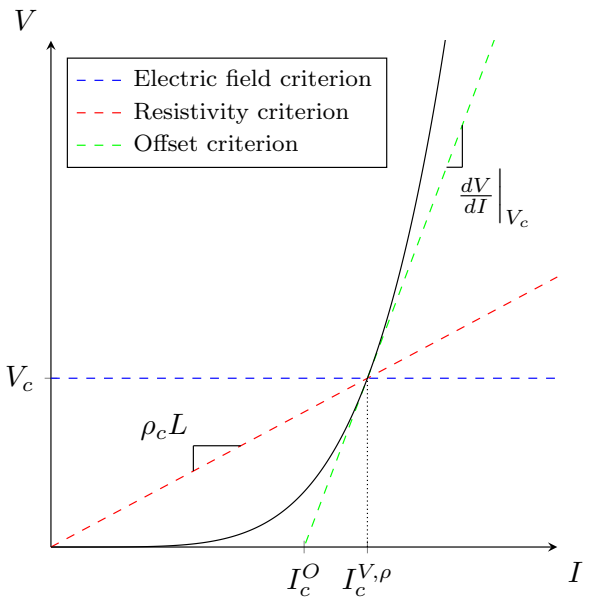


Figure 2.10 Illustration of existing I_c criteria. I_c^V, I_c^ρ, and I_c^O are respectively the critical currents found with the electric field, resistivity, and offset criteria. V_c corresponds to the product $E_c \times$ length. While $I_c^V = I_c^\rho$ in this example, that is not always true. Adapted from [20].

lossless, the flux creep, and the flux flow regimes. Given a sample with a power law E-J characteristic, e.g., REBCO tapes, it follows that the V-I characteristic will also have a power law form, such that $V \propto I^n$. Because of the smooth curve that is obtained, there is no clear theoretical way to determine I_c from experimental data. Standard practice is to establish a criterion and choose I_c such that it is the current that makes the sample reach this criterion. The most common ones are the electric field E_c, resistivity, or offset (backwards extrapolation from the linear region or the tangent to a chosen point) criteria [20], which are illustrated in figure 2.10. Typical values are $E_c = 1$ µV/cm and $\rho = 10^{-5}$ µΩcm. These values are generally chosen such that they offer a good compromise between a strict I_c measurement and the instrument resolution.

In practice, transport experiments are conducted with a four-point setup since voltages in superconductors are small [20]. Prior to measuring the V-I curve, the system is placed in the conditions that are desired, be it for the magnetic field norm, the magnetic field orientation, temperature, mechanical strain, etc. The experiment is then repeated to resolve I_c in the desired environmental parameter space. J_c can then be estimated from these measurements by dividing I_c by the superconducting cross-section of the sample. In general, transport measurements are the gold standard for any J_c measurements [9].

Since the primary focus of this work is the measurement of $J_c(B, \theta)$, let there be more emphasis placed on in-field measurements. Typically, V-I curves are measured in DC fields. These measurements are usually very time-consuming, as DC magnets are ramped very slowly [9]. That said, Leroux *et al.* have also done transport measurements in pulsed fields [60]. Pulsed measurements have the advantage of being quicker and possible at higher fields than DC ones, but require substantial sample preparation.

2.3.2 Magnetization Method

The magnetization method consists in placing a sample in a magnetic field and deducing J_c from the measurement of the resulting magnetic moment. This can be done because, at high enough fields (recall section 2.2.3), the magnetization currents reach the centre of the sample and their distribution can conveniently be determined by analytically solving the critical state equation. For instance, J_c in a cylinder is given by [53]

$$J_c = \frac{3m_i}{\pi R^3 d}, \tag{2.25}$$

where R is the sample radius, $m_i = \langle M_i \rangle V$, V is the sample volume, and d is its thickness (note that we do not assume $d \ll R$). For an isotropic orthorhombic sample, one can use equation (2.24) and substitute $\Delta M = 2\langle M_i \rangle = 2m_i/V$ and $J_{c1} = J_{c2} = J_c$, giving

$$J_c = \frac{12m_i}{W^2 d(3L - W)}. \tag{2.26}$$

This method is usually only employed when dealing with fields perpendicular to the sample. Lu *et al.* have done measurements in rotated fields without considering the anisotropy involved and it was shown that J_c calculations become inaccurate when the applied field is significantly rotated away from the sample's normal. The anisotropic case due to magnetic field orientation is treated in chapter 3.

Practical experiments are usually done using a vibrating sample magnetometer (VSM) or a superconducting quantum interference device (SQUID), as in [49, 61]. For the analytical formulas to be accurate, $\partial B/\partial t$ must be small or zero. This is the case because while thermal dissipation occurs in all cases (even when the inductive E is small, vortices moving in the sample cause dissipation, as discussed in section 2.1.3), it must be small enough that the sample's surroundings can absorb the heat faster than it is generated. When this is true, T remains constant and it is possible to extract any reversible magnetic contributions to the hysteresis loops by subtracting the average of the top and bottom branches [49]. If not, J_c varies as the sample heats up and the symmetry of the irreversible contribution is

broken. Having a small $\partial B/\partial t$ is also important to avoid inducing significant eddy currents in conductive but non-superconducting layers of the sample, e.g., copper or silver layers in commercial REBCO tapes. This point is discussed in chapter 4 and accounted for numerically.

One thing that is constant in this type of measurement is the penetration of screening currents all the way to the centre of the sample. Once this current saturation is achieved by ramping the magnetic field beyond the penetration field, the currents persist in the sample and external conditions can be changed in time to see how J_c evolves. Common experiments include measuring $m(T)$ at a fixed field, and the opposite, i.e. measuring $m(B)$ at a fixed temperature, as in [49,62]. Using the obtained data, it is possible to extract $J_c(T)$ and $J_c(B)$. Let it be known that data can be obtained at zero external field, but the field must be ramped higher than the penetration field first and then ramped back to zero.

In further sections, we will be making reference to this general procedure and we will refer to it as the QSFM (quasi-static field magnetization) method.

2.4 Numerical Modelling

This work requires the use of numerical simulations for validation purposes and to account for high $\partial B/\partial t$ effects. These simulations are performed with the finite element method (FEM), which leverages the discretization of the solution function space. While other methods could be used, e.g., finite differences, the FEM is chosen because it is commonly used in the applied superconductivity community.

Maxwell's equations are solved for the electromagnetic portion of the problem, and can be manipulated to yield different formulations. Each formulation is solved for its own field and/or potential (called state variable). Depending on the dimensionality of the domain and the approximations that are made, a given formulation can be chosen wisely to optimize numerical performance. Common numerically advantageous formulations are the H-ϕ [63–65] and T_p-A [66, 67] formulations, with ϕ the magnetic scalar potential, T_p the current potential, and A the magnetic vector potential. Both segregate conducting Ω_c and non-conducting Ω_{nc} regions of the domain and solve for a different state variable in each. For 2D simulations of conductor cross-sections where the thin shell approximation can be made, the T_p-A formulation is advantageous because T_p, in Ω_c, and A, in Ω_{nc}, only have a single significant component. This advantage is, however, not conserved in 3D domains, which is why the H-ϕ formulation was used in this work. Indeed, while H, the state variable in Ω_c, always has multiple significant components, ϕ, the state variable in Ω_{nc}, is always a scalar, no matter the dimensionality of the domain. A more detailed discussion on formulations can be found in [68].

The H-ϕ formulation makes use of the following state equations:

$$\text{In } \Omega_c : \qquad \nabla \times (\rho \nabla \times \mathbf{H}) = -\partial_t(\mu \mathbf{H}). \tag{2.27}$$

$$\text{In } \Omega_{nc} : \qquad \frac{\partial}{\partial t}(\nabla \cdot \mu \nabla \phi) = 0. \tag{2.28}$$

Both of these equations are derived from Faraday's and Ampère's laws. In Ω_{nc}, H is given by the definition $\mathbf{H} = -\nabla\phi$, and the other electromagnetic quantities can be computed with $\mathbf{B} = \mu\mathbf{H}$, $\mathbf{J} = \nabla \times \mathbf{H}$, and $\mathbf{E} = \rho \nabla \times \mathbf{H}$ [68]. Let it be known that in this paradigm, $\mathbf{H}$ is a conservative field in Ω_{nc} by definition. Therefore, if Ω_c is not simply connected, Ampère's law cannot be respected without introducing ϕ discontinuities in Ω_{nc}, usually called "cuts" [63,65]. This is not a concern for this work as all chosen Ω_c domains are simply connected, but is mentioned for the sake of completeness.

Let it be noted that the heat equation will be solved for the thermal portion of the problem. This will, however, not be discussed further as there is no ambiguity as to which equation should be solved and commercial FEM packages usually all have well-implemented modules for thermal physics.

CHAPTER 3 CALCULATING J_c FROM QUASI-STATIC FIELD MAGNETIZATION MEASUREMENTS IN FIELDS OF ARBITRARY ORIENTATION

This chapter deals with the first sub-objective, which consists in developing a new methodology for calculating J_c of samples cut from commercial REBCO tapes with QSFM in fields of arbitrary orientation. Section 3.1 goes over the derivation of the analytical method that is used, section 3.2 goes over the experimental trial that was done and its results, section 3.3 presents a preliminary validation of our method, and section 3.4 discusses the generalization of QSFM to scenarios with crystallographic anisotropy and with samples that have "non-idealities."

3.1 Analytical Method Derivation

3.1.1 Assumptions and Problem Setting

The main difference between QSFM measurements in fields perpendicular and non-perpendicular to the sample is that force-free effects must be considered. This means that J_c can have more than one value. To solve this, let us start by stating our assumptions, namely:

- a high field regime, i.e. $\mathbf{B} \approx \mathbf{B}_a$ (recall that $\mathbf{B}$ is the local field and $\mathbf{B}_a$ is the applied field),
- a thin geometry with fields $\mathbf{B}$, $\mathbf{H}$, and $\mathbf{M}$ homogeneous across the thickness d,
- an applied field B_a with a small ramping rate $\partial B_a/\partial t$,
- the Bean model is valid, i.e. $J = 0$ or $\pm J_c(B, \varphi_\perp, \varphi_\parallel)$, with $\varphi_\perp$ and $\varphi_\parallel$ defined in figure 2.5, and
- that force-free effects are the sole cause of anisotropy, i.e. we disregard anisotropy due to a change of orientation of J with respect to the a, b, and c crystal lattice axes.

Considering these assumptions and the results from the literature highlighted in the previous section, the irreversible contribution to the magnetic moment $\mathbf{m}_i$ is locked to the sample's normal vector $\hat{\mathbf{n}}$. In addition, because of the slow field ramping, the temperature T remains nearly constant and the only irreversible magnetic contribution comes from the superconducting layer of the sample, allowing for other layers to be ignored (we disregard the case where there would be hysteretic materials other than the superconductor in the sample). Finally,

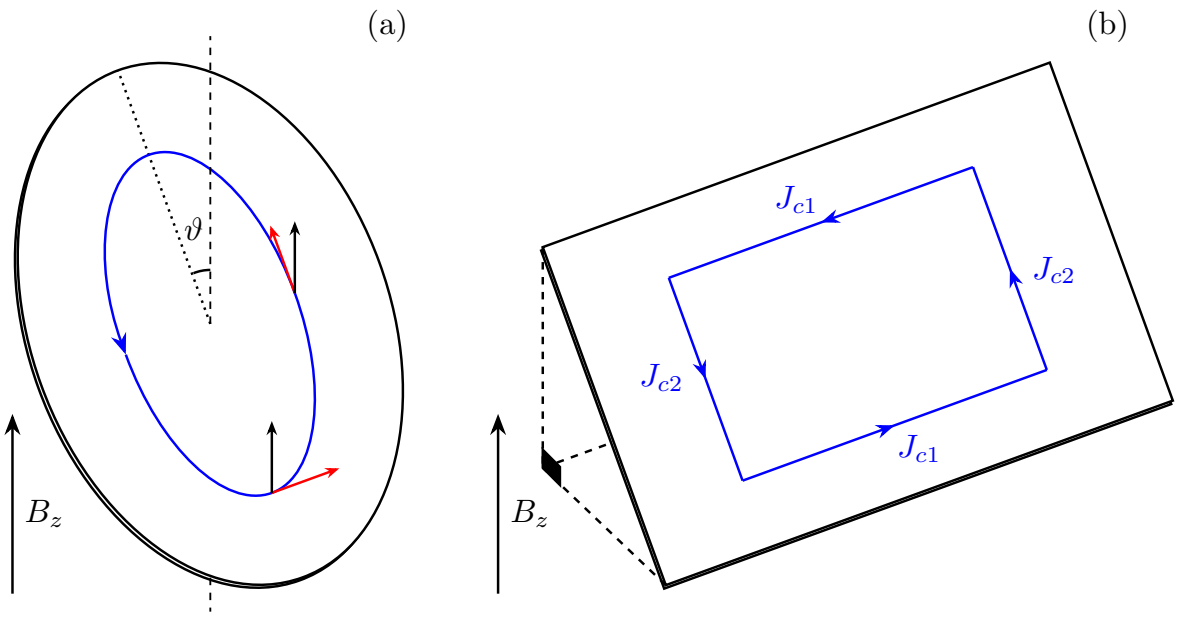


Figure 3.1 (a) Elliptical sample tilted with respect to the applied field. The red (black) arrows are the local **J** vector (**B** vector). The local angle between the red and black arrows changes along the current path represented by the blue arrow. (b) Rectangular sample tilted with respect to the applied field. There are only two possible orientations for **J** with respect to **B** and J can therefore only take the values J_{c1} or J_{c2}.

the high-field regime implies that screening currents permeate the whole superconducting layer of the sample.

While these assumptions greatly simplify the situation, none of them address the key issue of multiple J_c values. Indeed, screening currents flow along loops that are concentric to the sample perimeter and it can be deduced that the angles $\varphi_{\parallel}$ and $\varphi_{\perp}$ (see figure 2.5) vary continuously in space for an elliptical disk, for instance. A visual representation is given in figure 3.1 (a), where the black (red) arrows represent the local **B** (local **J**). The blue elliptical arrow represents a current loop and we point out that the red arrows (i.e. **J**) are tangent to it. If there is an angle ϑ between the sample's surface and $\mathbf{B}_a$, then the angle between **B** and **J** varies between $\pi/2$ (bottom arrow pair) and ϑ (top arrow pair, which forms the same angle as the dashed and doted lines). This implies that J_c also varies continuously in space and has an infinite number of values. Considering this, the sample shape must be chosen carefully. A wise choice in this scenario would be a rectangle of width W and length L (with $L > W$) since the current follows rectangular paths and therefore only has two possible orientations with respect to **B**, as shown in figure 3.1 (b). It then follows that there are only two possible J_c values, J_{c1} and J_{c2}. In these circumstances, the methodology used to derive equation (2.24) in [59] can be used.

3.1.2 Problem Resolution

The problem can now be boiled down to finding the two unknowns J_{c1} and J_{c2}. In this scenario, traditional QSFM procedures are insufficient as only one measurement is done, which only provides enough information to calculate a single unknown. We therefore solve this problem by making two independent measurements for every probed angle θ (defined in figure 3.2, with $\hat{\mathbf{z}}$ and $\hat{\mathbf{n}}$ contained within the shaded plane), where independence is achieved by rotating the sample about $\hat{\mathbf{n}}$ between measurements. The manner in which rotation makes measurements independent is going to be explained shortly. In this reference frame, $\theta = 0°$ implies that $\mathbf{B}_a$ is perpendicular to the sample and $\theta = 90°$ implies that $\mathbf{B}_a$ is parallel to the sample. The question that remains is: which two rotation angles should be chosen? We decide to orient the sample such that $J_{c1} = J_{c1}(B, \varphi_\perp)$, as in figure 2.5 (a), and $J_{c2} = J_{c2}(B, \varphi_\parallel)$, as in figure 2.5 (b). The two possible configurations are shown in figure 3.2 and are coined the "horizontal configuration" C_h (figure 3.2 (a)) and the "vertical configuration" C_v (figure 3.2 (b)). Let us note that this is only possible if $L \neq W$, as there must be a difference between C_h and C_v.

In a setting with no constraints on J_{c1} and J_{c2}, two current configurations are possible for both C_h and C_v. These are pictured in figure 3.3 and are identified with C_{h1}, C_{h2}, C_{v1}, and C_{v2} (respectively represented in figures 3.3 (a), (b), (c), and (d)). The blue partitions obey $J_c = J_{c1}$ and the red partitions obey $J_c = J_{c2}$. In these representations, the sample is

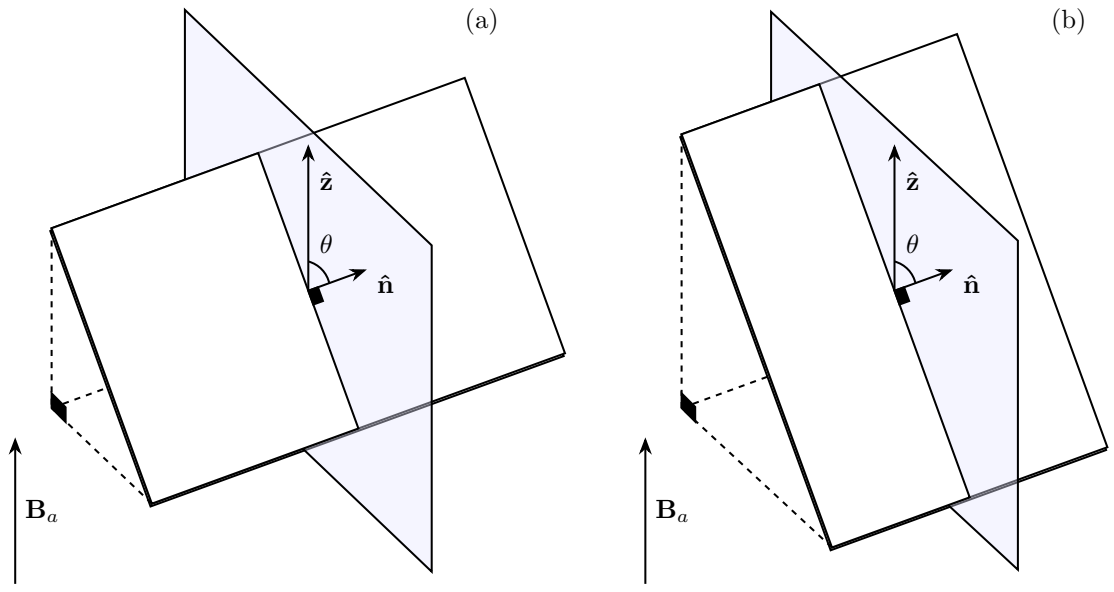


Figure 3.2 (a) Horizontal configuration C_h and (b) vertical configuration C_v.

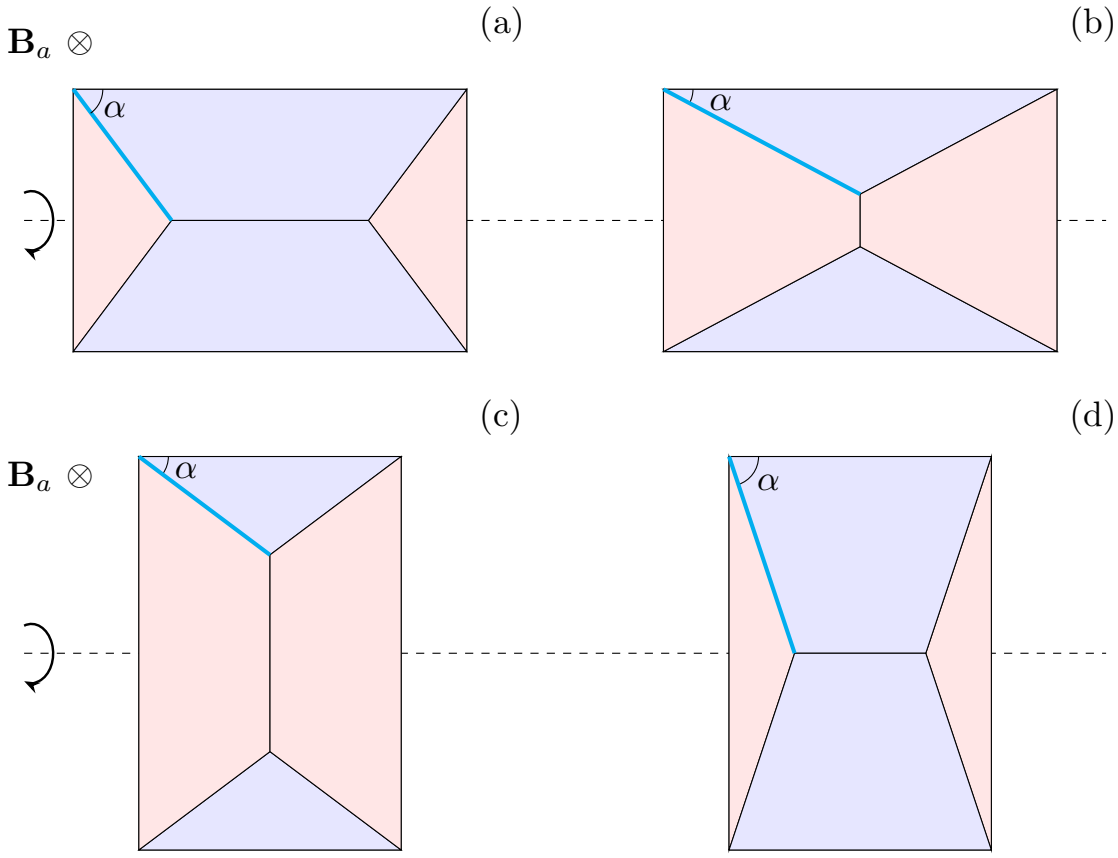


Figure 3.3 Current configurations during QSFM. The blue partitions obey $J_c = J_{c1}$ and the red partitions obey $J_c = J_{c2}$. (a) C_{h1}, (b) C_{h2}, (c) C_{v1}, and (d) C_{v2}. The samples are rotated about the dashed lines and the applied field B_a points into the page.

rotated around the dashed lines and B_a points into the page. The current configuration is determined by the angle α, defined graphically in figure 3.3. Since the current going around the sample must be conserved, α can be computed by leveraging the fact that the total current leaving a red partition must be equal to the total current entering a blue partition (and vice versa). This condition can be expressed with

$$\int \mathbf{J}_{c1} \cdot \mathrm{d}\mathbf{n} = \int \mathbf{J}_{c2} \cdot \mathrm{d}\mathbf{n}, \tag{3.1}$$

$$\Rightarrow \frac{J_{c2}}{J_{c1}} = \tan(\alpha), \tag{3.2}$$

where $d\mathbf{n}$ is an infinitesimal element with its width tangent to the cyan borders in figure 3.3 and oriented perpendicularly to them. The limiting cases between C_{h1} and C_{h2} and between C_{v1} and C_{v2} are respectively $J_{c2}/J_{c1} = W/L$ and $J_{c2}/J_{c1} = L/W$. Because the source of

anisotropy considered here are force-free effects, the condition $J_{c2} \geq J_{c1} \Leftrightarrow \alpha \geq \pi/4$ must be enforced and C_{h2} is not obtainable.

Using the relation for the irreversible magnetic moment $m_i = V\langle M\rangle_i$ (i subscript dropped hereafter), the volume of the sample $V = LWd$, and the methodology from [59], we derive m for the remaining three configurations for a given applied field, which yields

$$m_h = \frac{W^2 L d J_{c1}}{4}\left(1 - \frac{W J_{c1}}{3L J_{c2}}\right), \tag{3.3}$$

$$m_{v1} = \frac{W^2 L d J_{c2}}{4}\left(1 - \frac{W J_{c2}}{3L J_{c1}}\right), \tag{3.4}$$

$$m_{v2} = \frac{W L^2 d J_{c1}}{4}\left(1 - \frac{L J_{c1}}{3W J_{c2}}\right). \tag{3.5}$$

The integer subscript is dropped for the horizontal configuration as there is no more ambiguity. At this point, it can be noticed that $m_h \neq m_v$ for a given sample, demonstrating that rotation does produce independent measurements. To simplify further developments, we define the ratio

$$\Gamma = \frac{J_{c2}}{J_{c1}}. \tag{3.6}$$

For a pair $m_h(B)$ and $m_{v1}(B)$, a solution for Γ can be found by taking the ratio m_{v1}/m_h, which yields the cubic equation

$$W m_h \Gamma^3 - 3L m_h \Gamma^2 + 3L m_{v1}\Gamma - W m_{v1} = 0. \tag{3.7}$$

The solutions of equation (3.7) are the well-known roots of cubic equations and their nature (i.e. $\Gamma \in \mathbb{R}$ or $\Gamma \in \mathbb{C}$) can be determined by calculating the discriminant. There is always at least one real solution. Plugging Γ in equation (3.3), J_{c1} and J_{c2} can be calculated from

$$J_{c1} = \frac{12 m_h \Gamma}{W^2 d(3L\Gamma - W)}, \tag{3.8}$$

$$J_{c2} = \Gamma J_{c1}. \tag{3.9}$$

Alternatively, J_{c1} and J_{c2} can also be found by plugging Γ in equation (3.4), resulting in the solutions

$$J_{c2} = \frac{12 m_{v1}}{W^2 d(3L - W\Gamma)}, \tag{3.10}$$

$$J_{c1} = \frac{J_{c2}}{\Gamma}. \tag{3.11}$$

For a pair $m_h(B)$ and $m_{v2}(B)$, Γ can be solved for by taking the ratio m_{v2}/m_h. The solution can be shown to be

$$\Gamma = \frac{1}{3WL}\frac{m_h L^3 - m_{v2} W^3}{m_h L - m_{v2} W}. \tag{3.12}$$

J_{c1} and J_{c2} can be found either by using equations (3.8) and (3.9) or by plugging Γ in equation (3.5), yielding

$$J_{c1} = \frac{12 m_{v2} \Gamma}{L^2 d(3W\Gamma - L)}, \tag{3.13}$$

$$J_{c2} = \Gamma J_{c1}. \tag{3.14}$$

The last piece of the puzzle is to know which Γ to select during the resolution. Firstly, whether the sample is in C_{v1} or C_{v2} must be known. Secondly, if the sample is in C_{v1}, a way to determine which is the appropriate solution to equation (3.7) is needed. With regard to knowing if the sample is in C_{v1} or C_{v2}, let us point out that, at zero external field (assuming B_a was ramped down from a larger value), $J_{c1} \approx J_{c2}$, as force-free effects are not prominent with no outside field. While this is not strictly true because the demagnetization field becomes important and B is not uniform in the sample anymore, we can draw the conclusion that Γ must approach unity and that $\alpha \approx \pi/4$ as the applied field approaches zero. For a sample with $L \geq W$, this implies that $C_v = C_{v1}$ for fields below a certain threshold. As the field increases, the transition from C_{v1} to C_{v2} happens when the condition $\tan(\alpha) = \Gamma = J_{c2}/J_{c1} = L/W$ is met. This happens when the borders of the current partitions match the sample's geometric diagonals. When this condition is met, $L = \Gamma W$ and both equations (3.7) and (3.12) can be rewritten to be

$$2m_h\Gamma^3 - 3m_v\Gamma^2 + m_v = 0. \tag{3.15}$$

The possible solutions for Γ are therefore the same, and it is guaranteed that they can be chosen such that Γ remains continuous as the state goes from C_{v1} to C_{v2}.

With regard to choosing the right Γ when $C_v = C_{v1}$, figure 3.4 shows which solution should be chosen in a qualitative scenario. The fact that $\Gamma \approx 1$ when $B_a \approx 0$ can be used as a starting point. Assuming that $J_{c1}(B, \varphi_\perp)$ and $J_{c2}(B, \varphi_\parallel)$ are smooth and from the fact that Γ must be continuous, the same Γ solution should always be chosen unless it becomes degenerate for a given field with one of the other two solutions to equation (3.7). In other words, Γ should not "jump" between solution "branches" unless they cross. While increasing B_a from zero, the solution that is selected should therefore be the one closest to unity until it crosses another solution "branch", if another solution branch is crossed. In figure 3.4, Γ_2 is therefore chosen for $0 \leq B_a \leq B_1$. If a crossing of solutions does occur, the same solution

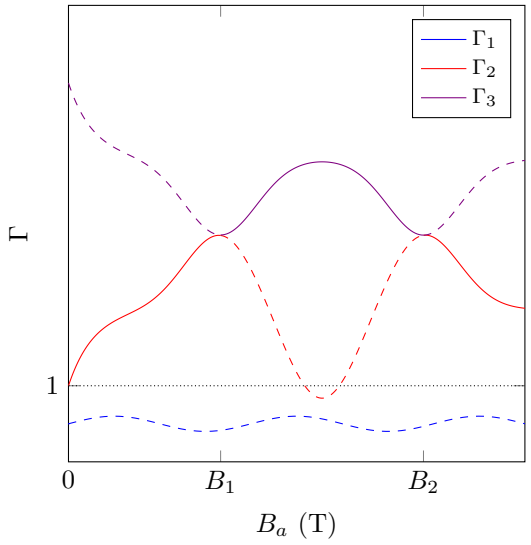


Figure 3.4 Qualitative evolution of the Γ solutions with respect to the magnetic field. The blue curve is the first solution $\Gamma_1(B)$, the red curve is the second solution $\Gamma_2(B)$, and the purple solution is the third solution $\Gamma_3(B)$. The first solution Γ_1 is discarded for any B_a since it is smaller than 1, which is not compatible with force-free effects. The solid line, regardless of colour, represents the selected solution for any B_a. For $0 \leq B_a \leq B_1$, Γ_2 is selected since it is superior to unity and the closest to it at $B_a = 0$ T. For $B_1 < B_a \leq B_2$, where Γ_2 and Γ_3 cross at $B_a = B_1$ and B_2, Γ_3 is selected since Γ_2 dips below 1 in this interval. For $B_a > B_2$, a potential transition back to Γ_2 after the second crossing is displayed.

must be kept until the next crossing occurs, if it occurs. After a crossing, one of the branches should be eliminated by seeking a contradiction anywhere on the interval where it would be selected, and the contradiction should be related to the physics of the problem (e.g., $J_{c1} > J_{c2}$ is not compatible with force-free effects). In figure 3.4, Γ_3 is chosen for $B_1 < B \leq B_2$ since Γ_2 dips below unity, which is not compatible with force-free effects. We note that Γ_1 is rejected over the whole field range for the same reason.

3.2 Experimental Trial

3.2.1 QSFM Method

The sample used for manipulations was cut from a Superpower SCS 4 mm wide tape, where YBCO is the superconducting material, and was determined to have dimensions $L = 2.87$ mm, $W = 2.20$ mm, and $d = 1.60$ µm. The QSFM measurements were carried out using the VSM apparatus integrated in a Quantum Design physical property measurement system (PPMS). The sample was sandwiched between cylindrical angled wedges, as shown in figure 3.5, which were then fitted in a tight straw attached to a rod oscillated along the

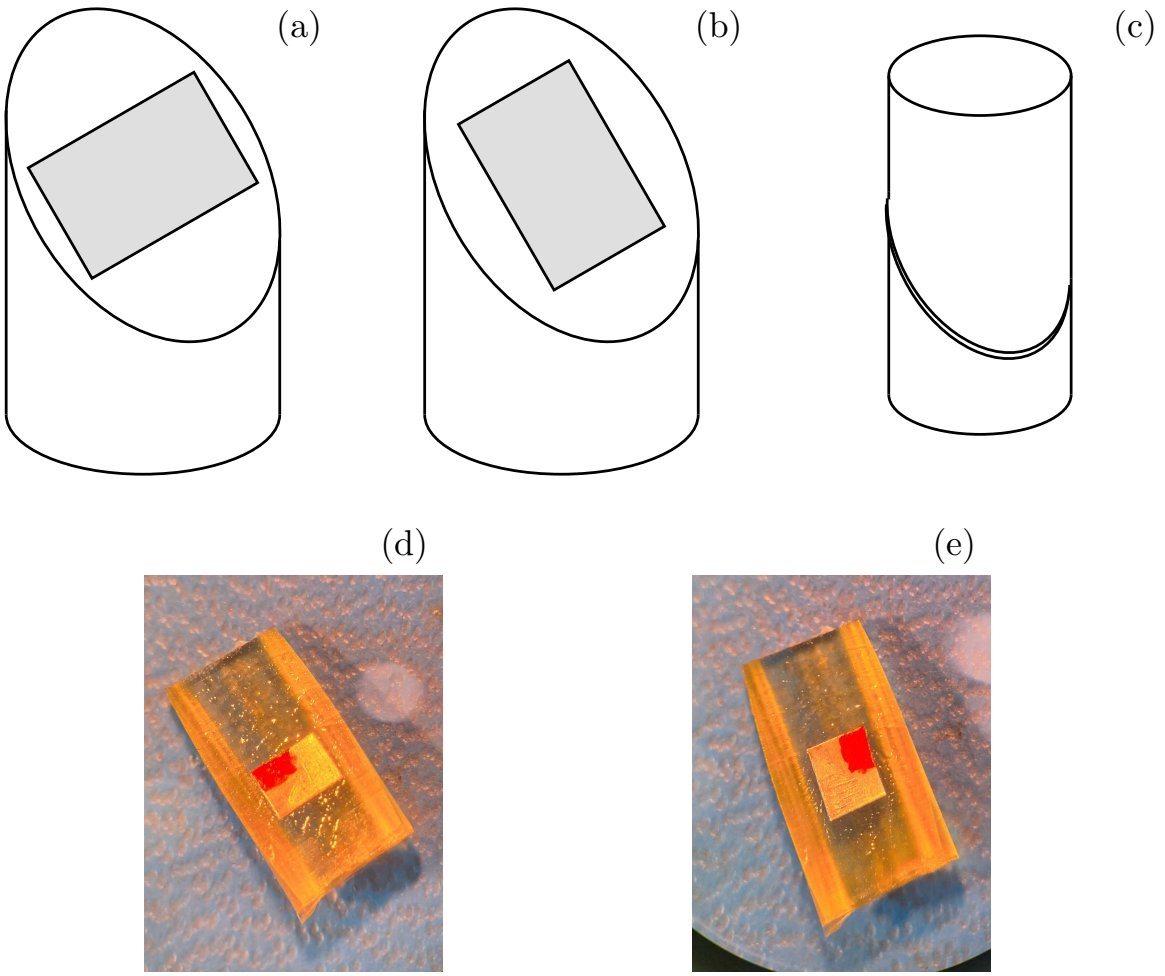


Figure 3.5 Sample placement in the (a) horizontal configuration and in the (b) vertical configuration. (c) *In situ* wedge placement. Marked face of the sample on the 85° wedge in (d) C_h and (e) C_v.

magnet's axis by an external actuator. The axes of the cylindrical wedges, the applied field, and the oscillatory motion of the sample are all parallel to the vertical $\hat{\mathbf{z}}$ direction in the laboratory's reference frame. The applied field was ramped down to −4 T to fully magnetize the sample, then up to 9 T, and finally back down to 0 T, with $|\partial B_a/\partial t| = 5$ mT/s. The measurements were done for $\theta = 0°$, 15°, 30°, 45°, 55°, 65°, 75°, 80°, 85°, and 88° in both C_h and C_v. The measurements were all done at 5 K, with the sample being brought back to room temperature between each one of them. One corner of the sample was marked such that the top and bottom faces could be told apart, which helped in making sure the marked face was always "on top" and the marked corner always had the same orientation during C_h (figure 3.5 (d)) and C_v measurements (figure 3.5 (e)).

3.2.2 Experimental QSFM Results and Discussion

Figure 3.6 (a) shows m_h measurements and figure 3.6 (b) shows m_h and m_v for selected angles. For the data to be usable, the reversible contributions of non-superconducting sample layers and surrounding materials were first taken out by subtracting the average of the top and bottom branches and then the total magnetic moment was computed with $m = m_z/\cos(\theta)$. More details on reversible magnetization subtraction are given in appendix A. The first trend that can be seen is that $|m|$ of the major hysteresis cycle increases with θ. Force-free effects and pinning from the ab planes become more prominent and cause J_{c1} and J_{c2} to be larger, increasing m_h. Secondly, the current reversal is done over a larger field interval as θ increases, which is expected since the field component perpendicular to the sample decreases. Finally, $m_h \approx m_v$ up to $\approx 55°$ and $m_v > m_h$ for larger angles. This is coherent with the results from [23] with YBCO, where $J_{c1} \approx J_{c2}$ up to $\approx 50°$ and $J_{c2} \geq J_{c1}$ for larger angles.

Let us point out that data at 88° is not presented because it is dominated by reversible magnetization and the sample is not fully penetrated by screening currents. The obtained m_h data is presented in appendix B. Also, the current reversal at 85° takes place over a very wide field range, which makes it hard to use the average of the top and bottom branches to subtract the reversible magnetization. In an attempt to render the 85° data usable, we interpolate between the reversible magnetization at 80° and 88° and scale the result such that it crosses the midpoint between the top and bottom branches of the 85° data at $B_a = 3.6$ T. More details on the data processing at 85° are given in appendix C.

The error ϵ associated to $m_h(B, \theta)$ is shown for selected angles in figure 3.6 (c). The error on the $\hat{\mathbf{z}}$ component ϵ_z is calculated by the PPMS for every data point. In this case, the Quantum Design PPMS uses a lock-in amplifier to extract the sample's signal during the measurement. Noise is considered to be random and its amplitude is assumed to follow a Gaussian probability distribution. ϵ_z is therefore the standard deviation of this Gaussian distribution. The error ϵ on m_h is computed with $\epsilon = \epsilon_z/\cos(\theta)$, explaining the large increase for large angles. The spike in the error is due to the poorer quality of the measurement when m is close to zero. This happens during the current reversal when $\partial B_a/\partial t$ changes sign, as there is a moment when the currents of opposite direction mutually cancel their contributions to m. There is therefore a shift of this spike towards smaller fields as θ increases because of the lengthening of the current reversal interval.

Figure 3.6 (d) shows Γ computed from m_h and m_v. The horizontal dashed line marks the C_{v1} to C_{v2} transition at $\Gamma = L/W \approx 1.309$. The general trend here seems to be that Γ increases with angle and field, which is expected as force-free effects become more pronounced. It can also be noticed that the amplitude of noise-like oscillations increases with θ, which is coherent with the fact that the error on the measurement grows with θ as well.

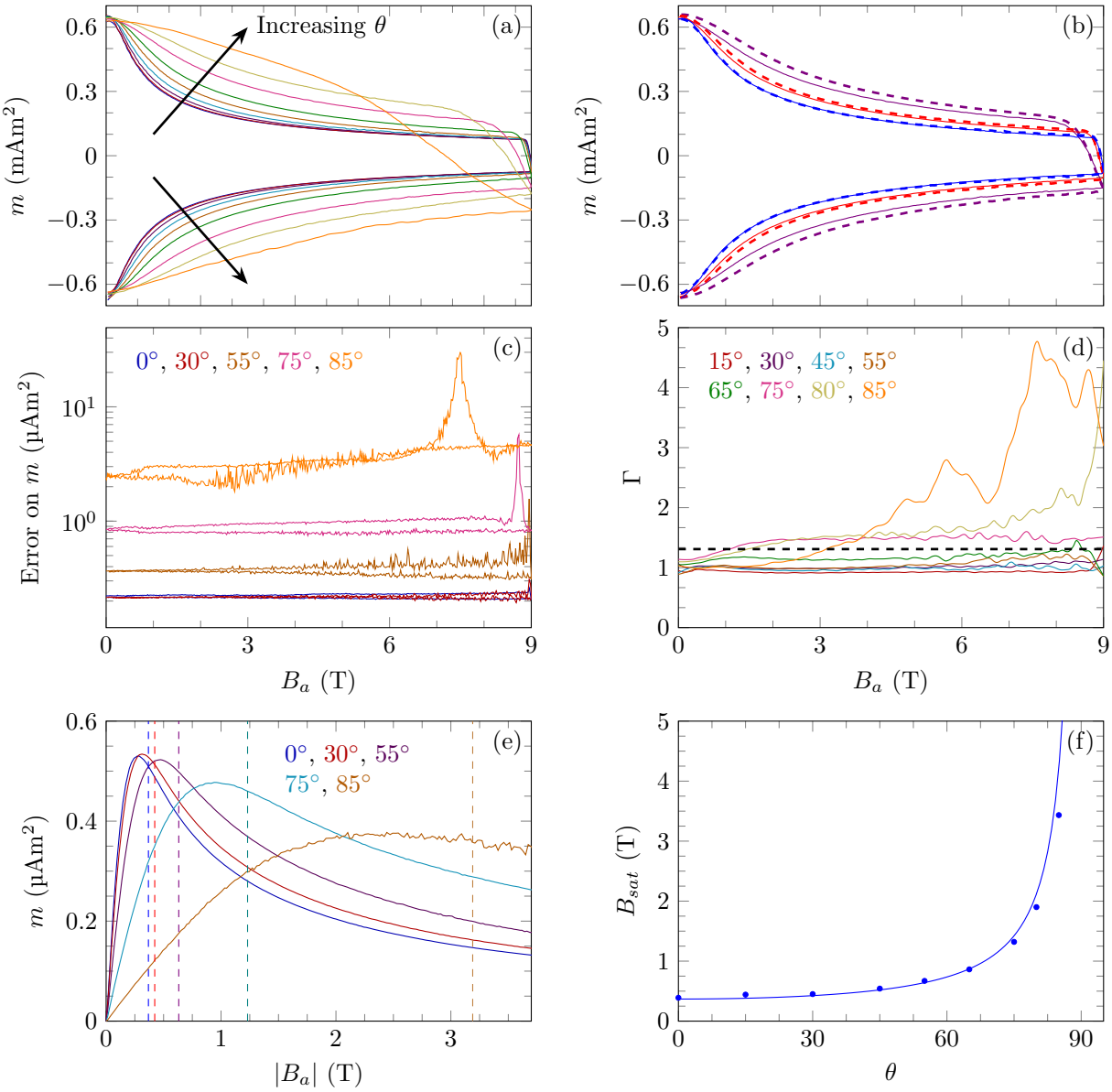


Figure 3.6 QSFM magnetization data. (a) m_h for $\theta = 0°$, 15°, 30°, 45°, 55°,65°, 75°, 80°, and 85°. (b) m_h and m_v for $\theta = 55°$ (blue), 65° (red), and 75° (purple). The solid lines represent m_h and the dashed lines represent m_v. (c) Measurement error ϵ on m for C_h measurements. (d) $\Gamma(B)$ for $0° \leq \theta \leq 85°$. The dashed black line represents the transition from C_{v1} to C_{v2}. (e) Initial magnetization m_h of the sample starting in the virgin state and B_{sat} calculation. The solid lines represent the measured magnetization m_h. The dashed lines represent the saturation field calculated with $B_{sat} = 1.3B_{max}$ associated to m_h of the same colour. The data is plotted as a function of $|B_a|$ for visualization purposes since the initial ramp is negative. (f) B_{sat} as a function of θ. The data points correspond to the absissae of the dashed lines in (e) and the solid line is given by $B_{sat}(\theta = 0°)/\cos(\theta)$.

Figure 3.6 (e) shows the magnetization of the sample from a virgin state. While this portion of data is not useful to calculate J_{c1} and J_{c2}, we use it to calculate the field below which the high-field regime assumption (i.e. $B \approx B_a$) breaks down, which we assume to be the field B_{sat} at which the current permeates the whole sample (recall the discussion from section 2.2.3 [55]). B_{sat} is calculated by finding B_{max}, the field that maximizes m in the displayed quadrant, and multiplying by a constant greater than unity to make sure m is actually on the major hysteresis cycle. B_{max} is reached when the progression of the current penetration and J decay from the increasing field balance out, where these phenomena have an opposite effect on |m|. We assume that m asymptotically approaches the major cycle after that point. We found that $B_{sat} = 1.3B_{max}$ works well and the calculated values are marked by the dashed lines.

Figure 3.6 (f) shows $B_{sat}(\theta)$. The data points correspond to the dashed lines in figure 3.6 (e), and the solid curve is given by $B_{sat}(\theta = 0°)/\cos(\theta)$. The good agreement between the data points and the solid curve indicates that, at least in regard to building the initial Bean profile, only the B component perpendicular to the sample matters.

Figures 3.7 (a) and (b) show the calculated $J_{c1}(B, \theta)$ and $J_{c2}(B, \theta)$ distributions in the interval $B_{sat} < B < 9$ T, i.e. where $B \approx B_a$ and our model is valid. The expected trends can be seen, i.e. J_{c1} and J_{c2} increasing with increasing θ and decreasing with increasing B (this is not true at high fields for J_{c2} at $\theta = 80°$ and 85° but is discussed below). It can also be seen that, in general, J_{c2} is larger than J_{c1}.

Figures 3.7 (c) and (d) show the relative error on J_{c1} and J_{c2}. This error is calculated by first computing the bounds on m_h and m_v, where the superior (inferior) bounds are found by adding (subtracting) the PPMS measurement error to the magnetic moments in both configurations. The obtained bounds are m_h^+, m_h^-, m_v^+, and m_v^-, where the $^+$ ($^-$) designates a superior (inferior) bound. Then, J_{c1} and J_{c2} are calculated with the different combinations of bounded m_h and m_v. These combinations are (m_h^+, m_v^+), (m_h^+, m_v^-), (m_h^-, m_v^+), and (m_h^-, m_v^-). This results in four different distributions for each J_{c1} and J_{c2} and the superior (inferior) bound for a given J_{ci} is calculated by taking the maximum (minimum) from these four distributions. The relative error is finally computed by taking the difference between the superior and inferior bounds and dividing by the centred J_{ci} (shown in figures 3.7 (a) and (b)).

It can be seen that the calculated relative error increases with θ and that all J_{c1} distributions and J_{c2} distributions up to 75° have an error below 10%, while the error on J_{c2} at $\theta = 80°$ and 85° reaches up to $\sim 70\%$. This is expected since, firstly, the error on m_h and m_v increases with θ. Secondly, J_{c2} at 80° and 85° is expected to have large errors because of Γ^2 in the numerator whether J_{c2} is computed using equations (3.8) and (3.9) or equations (3.13) and (3.14) (let's note that the sample is in C_{v2} for most of the applied field interval). On the

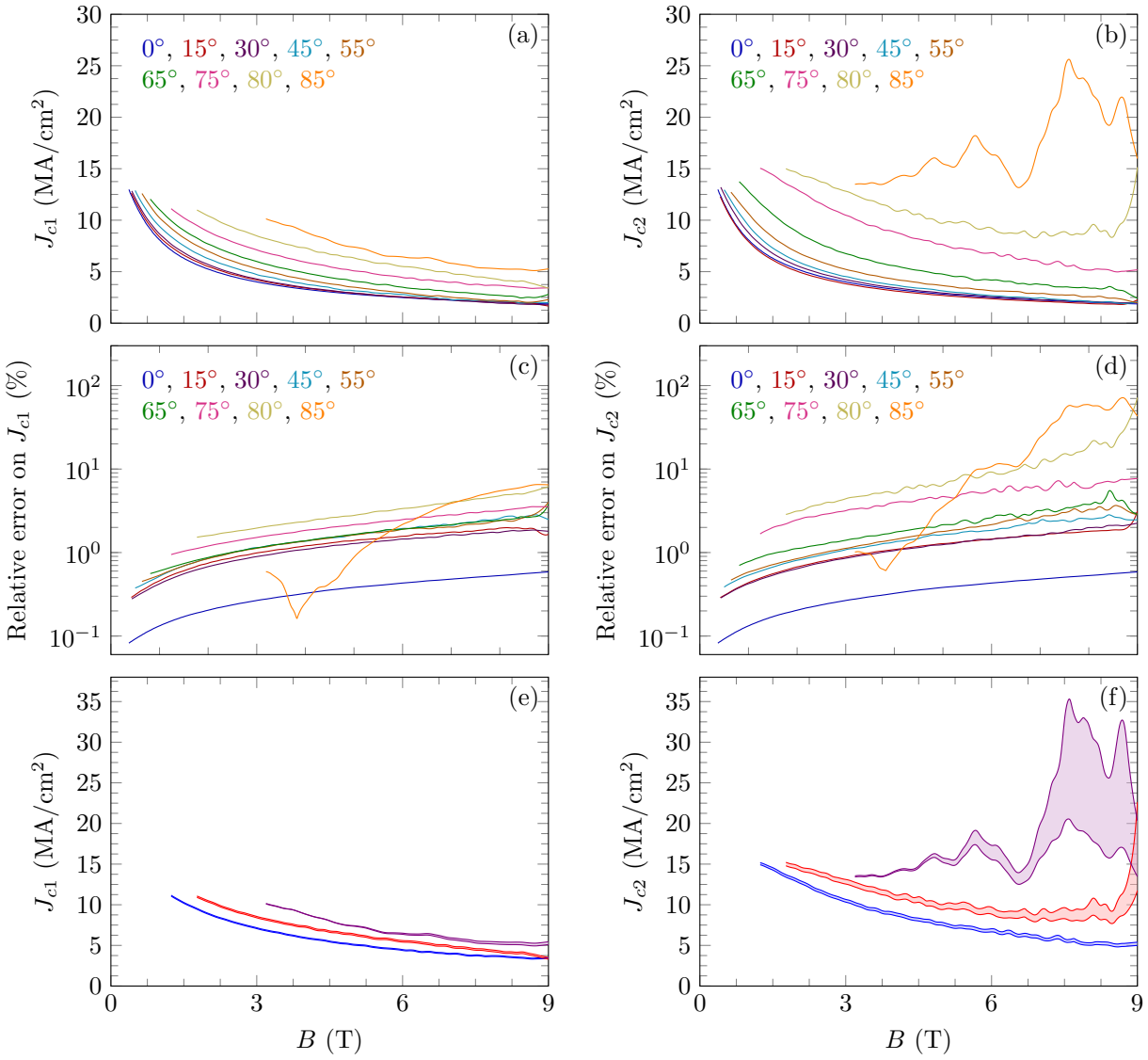


Figure 3.7 J_{c1} and J_{c2} results computed from QSFM measurements. (a) $J_{c1}(B,\theta)$ distributions, (b) $J_{c2}(B,\theta)$ distributions, (c) relative error on $J_{c1}(B,\theta)$, and (d) relative error on $J_{c2}(B,\theta)$. Uncertainty bounds on (e) J_{c1} and (f) J_{c2}, for $\theta = 75°$, 80°, and 85°.

other hand, the expressions for J_{c1} only have Γ in the numerator (see equations (3.8) and (3.13)). Explicitly, for J_{c2}, we have by plugging equation (3.8) into equation (3.9) and by plugging equation (3.13) into equation (3.14)

$$J_{c2} = \frac{12 m_h J_{c1} \Gamma^2}{W^2 d(3L\Gamma - W)} = \frac{12 m_{v2} J_{c1} \Gamma^2}{L^2 d(3W\Gamma - L)}. \tag{3.16}$$

While this does not seem to cause issues for $\theta \leq 75°$, the combination of these two error factors has a prominent effect on J_{c2} at high fields and at $\theta > 75°$. This means that, at high θ, the accuracy of the J_{c2} calculation is heavily dependent on the accuracy of Γ. Let's also note that equation (3.12) has a singularity when $m_h L = m_{v2} W$. When this condition is close to being satisfied, equation (3.14) explodes and the error has a dramatic impact on the result.

Figures 3.7 (e) and (f) show the bounds on J_{c1} and J_{c2} from which the relative error was computed, for selected angles. These clearly show that the accuracy of J_{c2} is much more sensitive than the accuracy of J_{c1}. Figure 3.7 (f) also indicates that there is another systematic error source that was not accounted for since we expect J_{c2} to decay monotonically, which is not the case even when sticking to the lower bound. This is most likely due to how the reversible magnetization was computed and subtracted from the total m_z. Indeed, when looking at the 80° data, it can be seen that J_{c2} blows up in the B_a interval where the current reversal occurs. As explained in appendix A, we must make a linear extrapolation to calculate the reversible magnetization in this interval, which induces an error. When looking at the 85° data, we can see that J_{c2} generally increases over the whole range, which we do not expect and means that the result is not trustworthy. This is most likely a result of the alternative reversible magnetization calculation method that was used (see appendix C for details). Other systematic errors to consider are, for instance, a faulty sample installation, where the sample would not be placed in a perfect C_h or C_v configuration because of a small extra rotation within the wedge plane.

3.2.3 Discussion on Experimental QSFM Results

In light of the previous results, let us discuss the nature of the solutions of equation (3.7), how our results compare to known physical models, and how QSFM could be improved. Figure 3.8 (a) shows the three solutions for $\Gamma(B)$ at $\theta = 80°$ in the complex plane, where the red solution was retained and the blue and purple solutions were not. While we could not have used the purple solution because of the "loose constraint" $\Gamma = J_{c2}/J_{c1} \geq 1$ (recall that the cause of anisotropy is the presence of a force-free regime), we could imagine a scenario where the blue solution could be appropriate if it crossed the red solution and remained real.

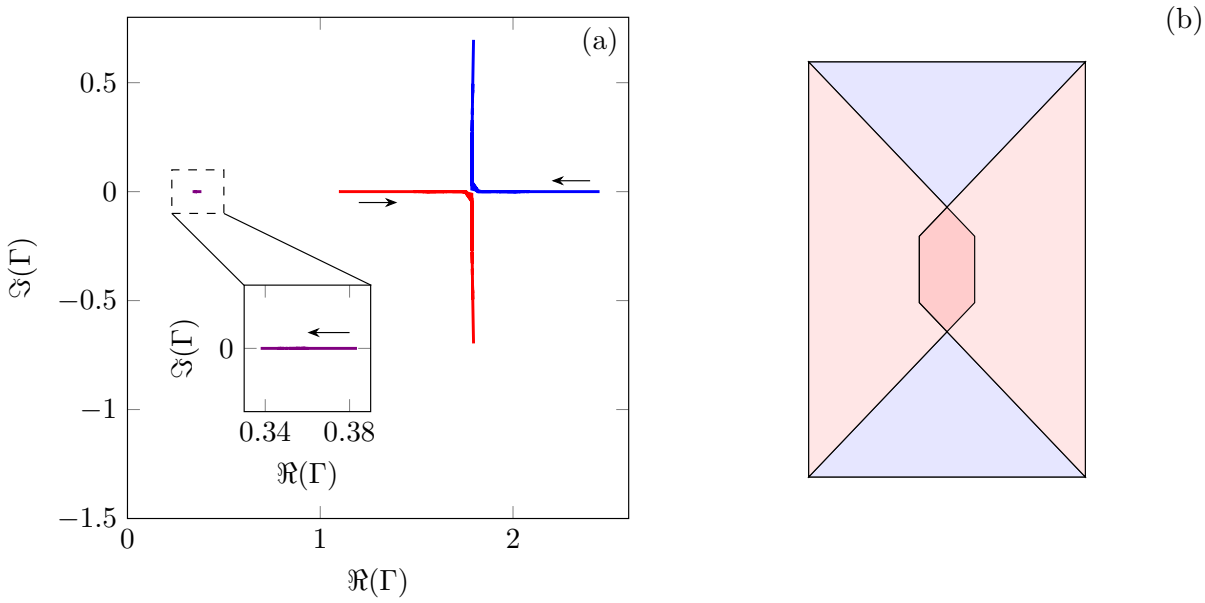


Figure 3.8 Interpretation of $\Gamma \in \mathbb{C}$. (a) Parametrization of Γ solutions in the complex plane. The arrows indicate the direction of evolution as B increases. (b) Example of a geometric contradiction corresponding to $\Gamma \in \mathbb{C}$.

However, we can see that the red and blue solutions seem to be symmetric to one another with respect to a point on the real axis close to 1.7. Let us therefore hypothesize that this symmetry is due to the nature of the cubic equation and that the two complex solutions never cross for any general case. This implies that only one of the solutions is useful.

We can also ask ourselves, what does a complex Γ mean? While we do not have a straightforward answer, a simple hypothesis is that it represents a geometric contradiction in the current partitions. A simple example of what a geometric contradiction could be is illustrated in figure 3.8 (b). That being said, the transition from C_{v1} to C_{v2} occurs before we need to be concerned with how to interpret $\Gamma \in \mathbb{C}$. This would, however, not be the case with a sufficiently skewed sample, i.e. where L is large enough with respect to W, because $\Gamma(B, \theta)$ would stay the same (since J_{c1} and J_{c2} are determined by local fields) while the criterion $\Gamma_t = L/W$ for the transition between C_{v1} and C_{v2} would be larger.

The obtained data can be compared to known models from the literature. Figure 3.9 (a) shows $J_{c2}(B, \theta)$, which is equivalent to $J_c(B, \varphi_\parallel)$, in polar coordinates in the force-free plane of the current space. This space is generated by the orthogonal vectors $\mathbf{J}_\parallel$ and $\mathbf{J}_\perp$, where $J_\parallel$ ($J_\perp$) is the current component parallel (perpendicular) to B. Looking at figure 2.5 (b), $J_\parallel$ and $J_\perp$ are respectively parallel to $J_c(B, \varphi_\parallel = \pi/2)$ and $J_c(B, \varphi_\parallel = 0)$. The total J_c in the force-free plane is the norm of the position vector (see [40] for more details). The data was

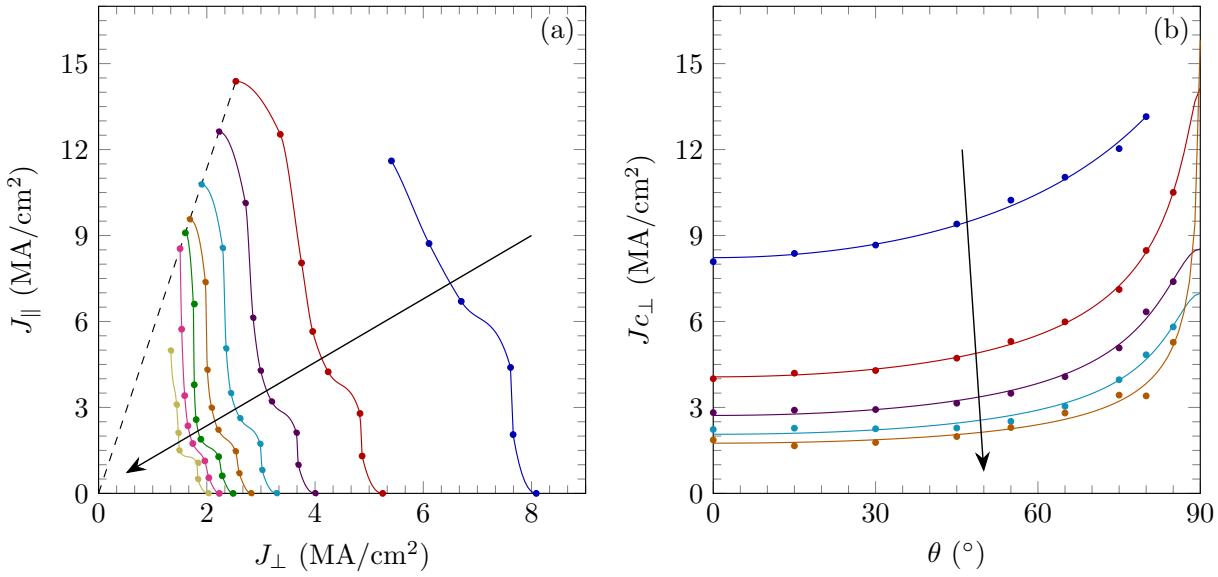


Figure 3.9 Comparison of J_{c1} and J_{c2} results to models from the literature. (a) J_{c2} interpolation in the force-free plane at $B_a = 1$ T, 2 T, 3 T, 4 T, 5 T, 6 T, 7 T, and 8 T. The dashed line goes along the 80° measurement data. The axes do not have the same length scale. (b) Fitting of equation (2.14) to J_{c1} data at $B_a = 1$ T, 3 T, 5 T, 7 T, and 9 T.

Table 3.1 Parameters obtained from the fitting of J_{c1} data to equation (3.17).

B_a (T)	J_{c0} (MA/cm^2)	k	B_0 (T)	β
1	15.58	$1.158 \cdot 10^{-6}$	0.550	0.616
3	16.89	0.0237	0.1580	0.475
5	22.0	0.0946	0.0908	0.520
7	17.42	0.0785	0.111	0.513
9	15.81	10^{-6}	0.0736	0.457

plotted for B_a between 1 T and 8 T, such that the high-field assumption is valid, and for $0° \leq \theta \leq 80°$, where the 85° data was rejected because of its poor quality. The EECSM [40] makes the prediction that the J_c contour lines are elliptical in the force-free plane. Our data seem to be different considering that there is a recurring relatively abrupt slope change near 30°, but the overall trend does seem qualitatively elliptical. That being said, an important difference between the experiment considered by Clem *et al.* and our own is that Clem *et al.* used a long cylindrical sample of small diameter while we used a sample with a thin plate geometry. In virtue of the fact that there is a magnetic energy term in the Ginzburg-Landau free energy, we can expect the vortices to act differently in these different geometries to minimize the energy of the system. Assuming that force-free dissipation is determined by

pinning as discussed in section 2.1.4, it seems reasonable to think that the vortex lattice in these geometries interacts differently with the pinning centres and influences J_c.

Figure 3.9 (b) displays $J_{c1}(B,\theta)$, which is equivalent to $J_c(B,\varphi_\perp)$, for B_a = 1 T, 3 T, 5 T, 7 T, and 9 T. To see if our method produces results that are consistent with existing models, the data was fitted to equation (2.14). Using $B_\parallel = B\sin(\theta)$ and $B_\perp = B\cos(\theta)$, equation (2.14) was reformulated as

$$J_c = J_{c0}\left(1+\frac{B}{B_0}\sqrt{(k^2-1)\sin^2(\theta)+1}\right)^{-\beta}. \tag{3.17}$$

The obtained fits are plotted as solid lines in figure 3.9 (b). The agreement between our data and the fit is excellent. The only mishap happens at $B_a = 9$ T close to 90°, where the fitted function unexpectedly explodes above all the others at lower fields. The obtained fitting parameters are presented in table 3.1. Let us note that, while the fitting quality was good, the obtained fitting parameters cannot be taken for granted as fittings of similar quality were obtained with various other parameter combinations.

Finally, our experiment could be improved in different ways, firstly by having a more skewed sample. This would allow for a more pronounced difference between m_h and m_v and would be especially useful for calculating J_{c1} and J_{c2} in situations with a small θ, where force-free effects are not prominent. The choice of L and W should also be made such that the configuration changes from C_{v1} to C_{v2} before Γ has an imaginary part.

Secondly, using a VSM or SQUID in which *in situ* rotation is possible and with pickup coils centred on two perpendicular axes, as in reference [49], would be another improvement. This would allow reducing the error on m for large θ, as m could be measured with the coil closest to $\hat{\mathbf{n}}$ and the error could be calculated with error = $(\text{error})_{x,y}/\cos(90°-\theta)$. *In situ* rotation would also ensure that the sample is always permeated by screening currents, since the sample could be magnetized at $\theta = 0°$ and then rotated to, e.g., $\theta = 88°$.

3.3 QSFM Numerical Validation

3.3.1 Numerical Model Definition

Since data from transport measurements are not available to assess the accuracy of our method, numerical simulations are used to generate reference $m_h(B_a)$ and $m_v(B_a)$ data. From this reference set, J_{c1} and J_{c2} can be computed and then compared against the known current distributions in the sample. To model the situation, we assume

- that the magnetic response of the superconductor is entirely due to screening currents induced by the applied field B_a,

- a thin sample geometry of thickness d,
- a small $\partial B_a/\partial t$,
- a power law E-J constitutive equation, and
- an isotropic J_c within the ab plane when force-free effects do not need to be considered (i.e. no crystallographic anisotropy).

From these assumptions, further simplifications can be made. Firstly, reversible magnetization does not need to be modelled and corrected for. Practically speaking, this is done by setting the magnetic susceptibility $\chi_m(B) = 0$. Secondly, the current is assumed to be entirely contained within the plane of the sample, i.e. $\mathbf{J} \cdot \hat{\mathbf{n}} = 0$. Finally, the small B_a ramping rate allows us to ignore heating and non-superconducting sample layers (recall the discussion from section 2.3.2).

The numerical model used was implemented using the commercial FEM software Comsol Multiphysics 6.2 with the AC/DC and Mathematics modules and makes use of the H-ϕ formulation. Detailed discussions on the practical implementation of the formulation in Comsol are given in [64,69,70]. The simulation is set in what we will refer to as the "sample's reference frame", defined in figure 3.10 (a) (as opposed to the laboratory's reference frame displayed in figures 3.1, 3.2, and 3.5). The reference frame is chosen such that $\hat{\mathbf{z}}$ is parallel to $\hat{\mathbf{n}}$ and $\hat{\mathbf{x}}$ and $\hat{\mathbf{y}}$ are parallel to the edges of length W and L. We chose B_a to be contained within the yz plane and swap W and L to go back and forth between C_h and C_v. The simulation domain is shown is figure 3.10 (b), where the conducting domain Ω_c is highlighted in blue and a symmetry boundary condition is applied to the yz plane. The domain is meshed using hexahedral elements in Ω_c and tetrahedral elements in Ω_{nc} (see figure 3.10 (c)). To enforce the $\mathbf{J} \cdot \hat{\mathbf{n}} = 0 \Leftrightarrow J_z = 0$ condition, Ω_c is only meshed with a single element layer along the sample thickness to ensure there is no current sharing between layers. The superconducting layer is also scaled by a factor γ to avoid having skewed elements and to have better convergence. This factor is accounted for in the resistivity expression.

To implement the power law constitutive equation, equation (2.12) can be reformulated to have the form $E = \rho J$, with the resistivity ρ given by

$$\rho = \frac{E_c}{J_c}\left(\frac{J}{J_c}\right)^{n-1}. \tag{3.18}$$

In this setting, ρ can be expressed as a diagonal tensor and the ρ_x and ρ_y components can be associated to J^*_{c1} and J^*_{c2}. Let us note that the * exponent is used to designate currents used as inputs in Comsol, which are not the same as the currents calculated with our analytical

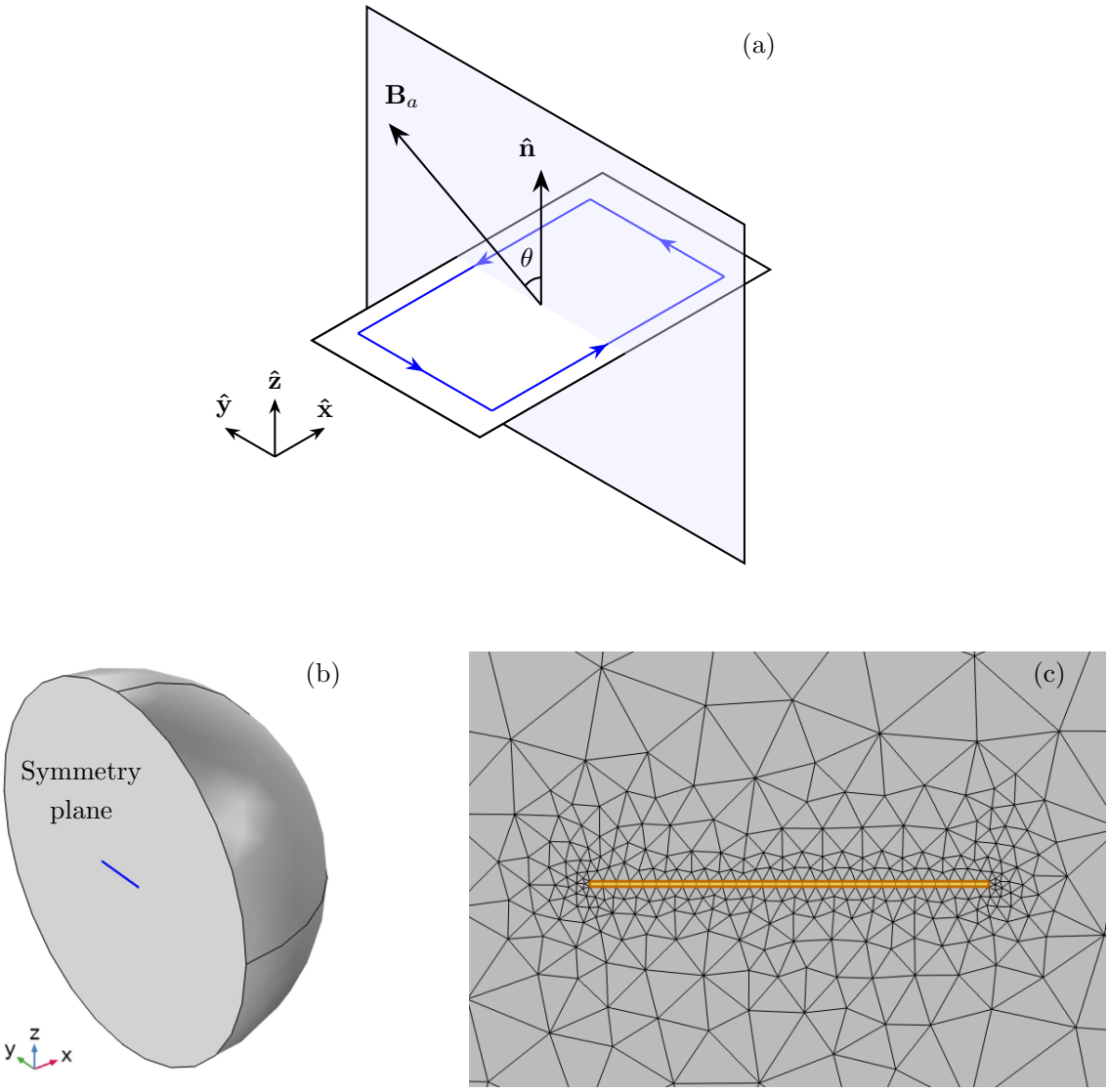


Figure 3.10 QSFM FEM model definition. (a) Sample's reference frame. The sample is represented by the white thin rectangle and the yz plane is represented by the blue-shaded plane containing $\mathbf{B}_a$ and $\hat{\mathbf{n}}$. (b) FEM simulation domain. Ω_{nc} is represented by a half-sphere and both Ω_c and Ω_{nc} have a symmetry boundary condition along the equivalent of the shaded plane in (a). (c) yz view of the mesh with a zoom on the sample represented in the highlighted region.

method, J_{c1} and J_{c2}. That being said, J^*_{c1} and J_{c1} are defined such that they are both parallel to $\hat{\mathbf{x}}$ in the sample's reference frame (J^*_{c2} and J_{c2} are similarly both parallel to $\hat{\mathbf{y}}$). Accounting for γ, the diagonal components are

$$\rho_x = \frac{\gamma E_c}{J^*_{c1}}\left(\frac{\gamma J_x}{J^*_{c1}}\right)^{n-1}, \tag{3.19}$$

$$\rho_y = \frac{\gamma E_c}{J^*_{c2}}\left(\frac{\gamma J_y}{J^*_{c2}}\right)^{n-1}, \tag{3.20}$$

$$\rho_z = \varepsilon^{-1}. \tag{3.21}$$

ε is a predefined small number in Comsol used to avoid divisions by zero without changing the result. Choosing this ρ_z makes it very large and, while it is redundant with using a single element layer in Ω_c, serves to enforce $J_z = 0$.

Force-free effects are modelled through the J^*_{c2} choice. To compute it, the following procedure is followed.

1. The angle $\varphi_\parallel$ is computed by exploiting the dot product property $\|\mathbf{J}\|\|\mathbf{B}\| = JB\cos(\varphi_\parallel)$. Explicitly, we have

$$\varphi_\parallel = \cos^{-1}\left(\frac{J_yB_y + J_zB_z}{\|\mathbf{J}\|\|\mathbf{B}\| + \varepsilon}\right). \tag{3.22}$$

   ε is added to the denominator to avoid divisions by zero and J_x and B_x are ignored since they are not in the force-free plane.

2. J^*_{c2} is computed using the EECSM (discussed in section 2.1.6). Using $\varphi_\parallel$, equation (2.15) can be rewritten

$$J^*_{c2} = \left(\frac{\cos^2(\varphi_\parallel)}{J^{*2}_{c\perp}(B)} + \frac{\sin^2(\varphi_\parallel)}{J^{*2}_{c\parallel}(B)}\right)^{-1/2}. \tag{3.23}$$

   Let it be noted that $J^*_{c\perp}$ and $J^*_{c\parallel}$ are chosen as simulation inputs.

Once computed, J^*_{c2} can be directly inserted in the ρ_y expression. J^*_{c1} could be implemented with a $\varphi_\perp$ dependency in a similar fashion, which was not done here. Indeed, the objective of this numerical experiment was to assess the accuracy of our previous analytical development and only the knowledge of J_x and J_y is necessary to do so (this is discussed shortly). The implementation of a $\varphi_\parallel$ dependency without a $\varphi_\perp$ one was the best comprise found between realism and likelihood of convergence. We therefore set $J^*_{c1}(B, \varphi_\perp) = J^*_{c\perp}(B)$.

The $J^*_{c\perp}(B)$ and $J^*_{c\parallel}(B)$ distributions are used as inputs and are chosen to be described by equation (2.13). To be representative of force-free effects, their parameters must be chosen

such that $J^*_{c\parallel}(B=0) = J^*_{c\perp}(B=0)$ and $J^*_{c\parallel}(B) \geq J^*_{c\perp}(B)$. To this end, B_0 is substituted with $B_{0\parallel}$ or $B_{0\perp}$, giving

$$J^*_{c\parallel,\perp}(B) = \frac{J_{c0}}{(1+B/B_{0\parallel,\perp})^{\beta}}. \tag{3.24}$$

J_{c0} is the same for both $J^*_{c\parallel}$ and $J^*_{c\perp}$, with $B_{0\parallel} \geq B_{0\perp}$, and where β is an exponent added for generality.

3.3.2 QSFM Numerical Validation Results and Discussion

The parameter values used for the generation of $m_h(B_a,\theta)$ and $m_v(B_a,\theta)$ are given in table 3.2. The field was ramped up to B_{pk} and then brought back to zero following a triangular waveform. Note that we do not need to apply a field of opposite polarity first, as described in section 3.2, because there is no need to correct for reversible contributions and therefore no need to have the top and bottom branches fully magnetized (recall that the data correction is made by subtracting the average of the top and bottom branches of the major cycle to the raw data). Simulations were done for both C_h and C_v at 0°, 15°, 30°, 45°, 55°, 65°, 75°, and 80°.

To validate our results, we numerically calculate the average current densities $\langle J_1 \rangle$ and $\langle J_2 \rangle$ across the sample's green cross-sections shown in figure 3.11. These averages are used as comparison points for J_{c1} and J_{c2}, the currents calculated from m_h and m_v with the formalism from section 3.1. The reason this is done, as opposed to using the inputs $J^*_{c\perp}$ and $J^*_{c\parallel}$, is that J is substantially smaller than J_c in our simulations, regardless of the current partition that is looked at. This is a result of using the power law E-J constitutive equation, which is ill-suited to model magnetization experiments. Indeed, quasi-static magnetization

Table 3.2 QSFM simulation parameters.

Parameters	Values
L	3 mm
W	2 mm
d	1.6 µm
γ	25
B_{pk}	35 T
$\partial B_a/\partial t$	5 T/min
J_{c0}	22.0 MA/cm^2
$B_{0\perp}$	5 T
$B_{0\parallel}$	30 T
β	0.9
E_c	1 µV/cm
n	30

induces electric fields in the sample that are smaller than typical E_c values, which causes $J < J_c$ [50,71]. That being said, references like [72,73] discuss how to model the magnetization of REBCO superconductors while taking into account force-free dissipation but they make use of variational methods rather than the FEM, and implementing such methods goes beyond the scope of this work. We therefore continue by comparing J_{c1} and J_{c2} to $\langle J_1 \rangle$ and $\langle J_2 \rangle$ for simplicity. The green cross-sections are used to calculate $\langle J_1 \rangle$ and $\langle J_2 \rangle$ instead of the cyan ones because they cross current partitions that penetrate to the centre of the sample. This is more accurate as the cyan cross-sections must be stopped before reaching the centre to avoid $J \approx 0$ regions, which would bias the averaging. While the discarded averaging paths could be defined such that they go from the surface of the sample to, for instance, half of the distance to the centre, they would still be inaccurate as the current partitions move in time as α and $\Gamma(B)$ evolve.

Figures 3.12 (a) and (b) show the J distributions in the sample for C_h and C_v respectively. It can be seen that J is roughly constant within the current partitions, which are delimited by sharp transitions in the current norm. Because of this J uniformity, we consider $\langle J_1 \rangle$ and $\langle J_2 \rangle$ to be in some sort equivalent to "effective" critical current densities. While the chosen E-J law is flawed in this particular scenario, the current partitions remain very similar to what was shown in figure 3.3. Let us remark, however, that C_{v2} was never observed numerically here. Figure 3.13 (a) shows m_h and m_v at 80°, which show similar behaviour to m_h and m_v in figure 3.6 (b) (i.e. $m_v > m_h$) despite the E-J law. Figure 3.13 (b) shows both the references $\langle J_1 \rangle$ and $\langle J_2 \rangle$ (dashed lines) and the calculated J_{c1} and J_{c2} (solid lines) at 80°. It can be seen that the agreement for $J_{c1}(\theta = 80°)$ is excellent, while the agreement for $J_{c2}(\theta = 80°)$ is of similar quality but a little less accurate. This matches the trend seen with

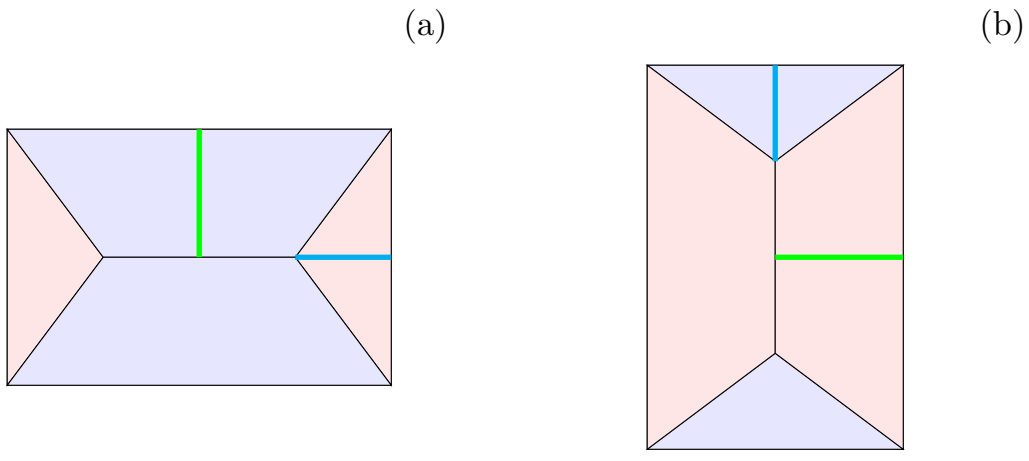


Figure 3.11 Cross-section definitions for $\langle J_1 \rangle$ and $\langle J_2 \rangle$ in (a) C_h and (b) C_v.

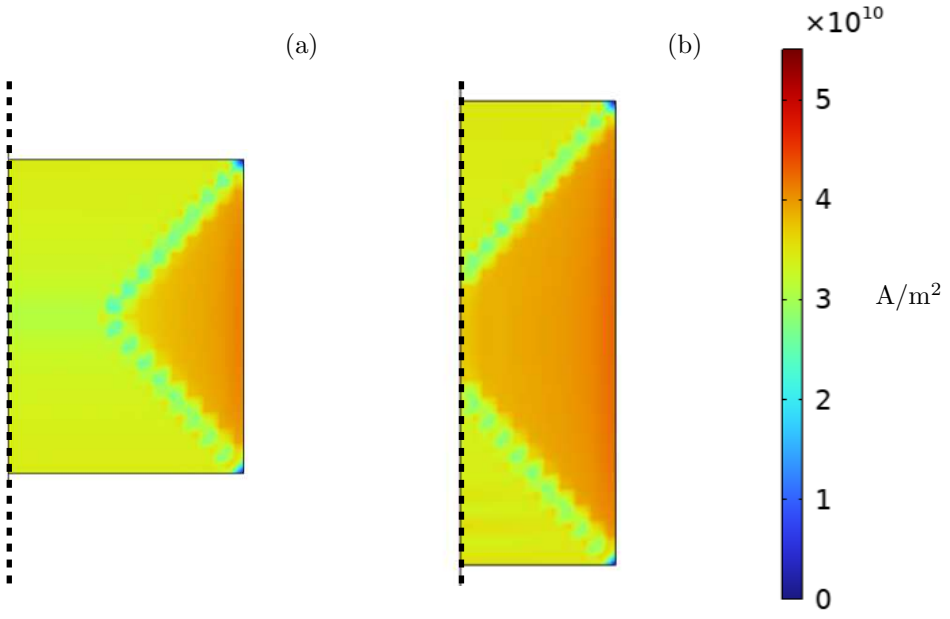


Figure 3.12 J colour plot at $B_a = 30$ T in (a) C_h and (b) C_v. The dashed lines represent the symmetry plane.

our experimental results, where the error on $J_{c2} \propto \Gamma^2$ was larger than the error on J_{c1} (see figure 3.7). Figures 3.13 (c) and (d) respectively show the relative error on J_{c1} and J_{c2} for the angles that were probed. Despite all the assumptions that were made (most importantly assuming that the Bean model is valid, i.e. $n \to \infty$), the relative error remains below 5% in both cases. We can notice that the error at higher angles progresses towards an asymptote for both J_{c1} and J_{c2}. This is most likely due to the implementation of the E-J law, as this was not seen in the experimental data.

These results seem satisfactory as a preliminary validation. That being said, the numerical model that was used could be improved such that the chosen E-J constitutive law is better suited for low electric field situations like quasi-static magnetization. A possibility would be to use a percolation law as discussed in [71]. This law is piecewise continuous and prescribes $\rho = 0$ when $J < J_{cmin}$, where J_{cmin} is a threshold current density smaller than J_c. This is somewhat like giving a "head start" to J and could conceivably make it so that $J \approx J_c$. The constitutive equations in references [72,73] could also be looked into. These are left for future investigation. The ultimate way to validate our method would be to do transport current measurements, which are the gold standard for measuring J_c at the moment. We also leave this work for future contributions.

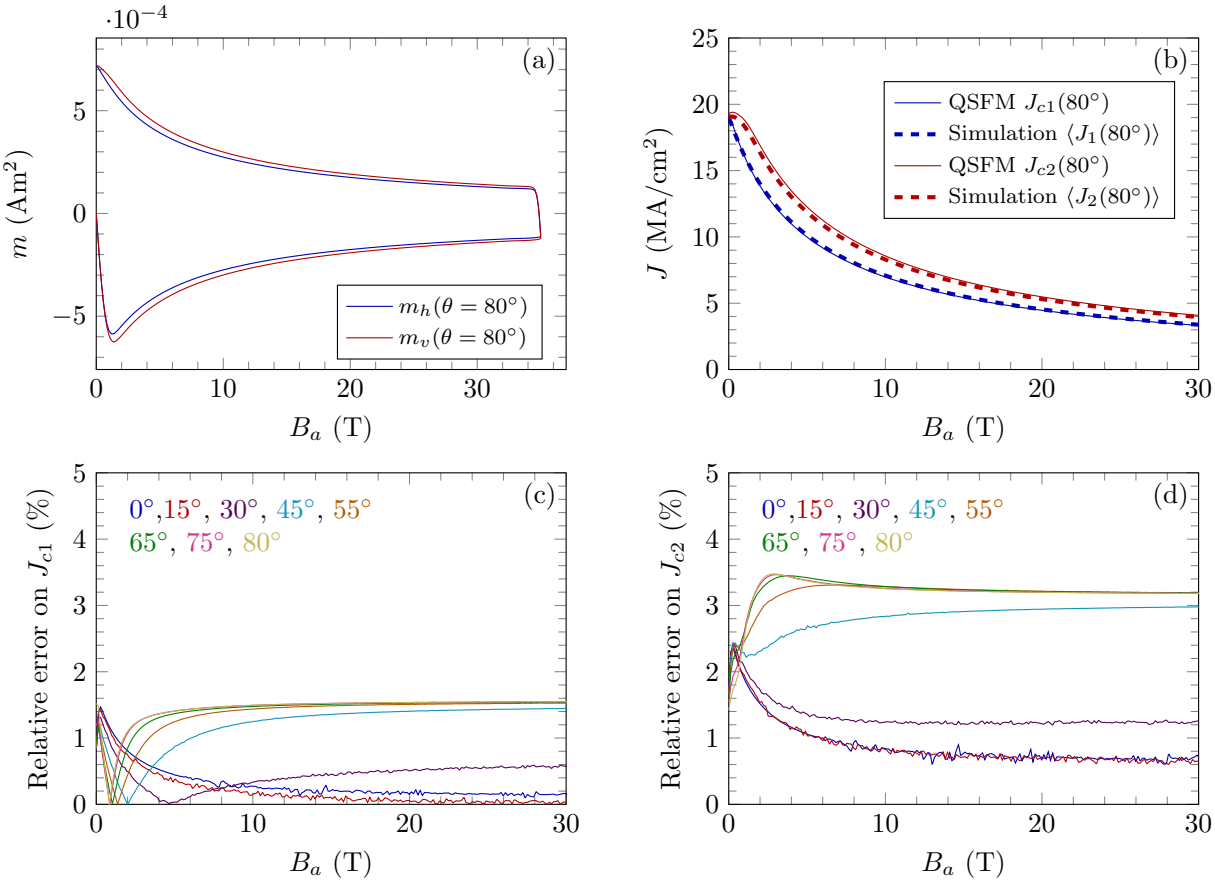


Figure 3.13 (a) Half-hysteresis loops in C_h and C_v, (b) J_{c1} and J_{c2} magnitudes compared to $\langle J_1 \rangle$ and $\langle J_2 \rangle$ at $\theta = 80°$, (c) relative error on J_{c1} for all angles, and (d) relative error on J_{c2} for all angles.

3.4 QSFM Generalization and Discussion

3.4.1 Generalization to Crystallographic Anisotropy

The case that was studied in this work was the one of anisotropy due to force-free effects, which is not the only possible one for anisotropic J_c in superconductors. In a more general case, J_c can vary depending on its orientation with respect to the crystal axes. In REBCO materials, the J_c anisotropy between the c axis and the ab plane is well known but is rarely considered. Indeed, tapes are usually manufactured such that the large face is parallel to the ab planes, which are therefore always parallel to the current direction. That being said, J_c can also be anisotropic with respect to the a and b axes, as reported in [74]. If this anisotropy is pronounced, it cannot be neglected in QSFM measurements, as the current's looping nature implies that it necessarily sees the effect from both axes.

In such cases, QSFM can still be used, but a few modifications must be made to the

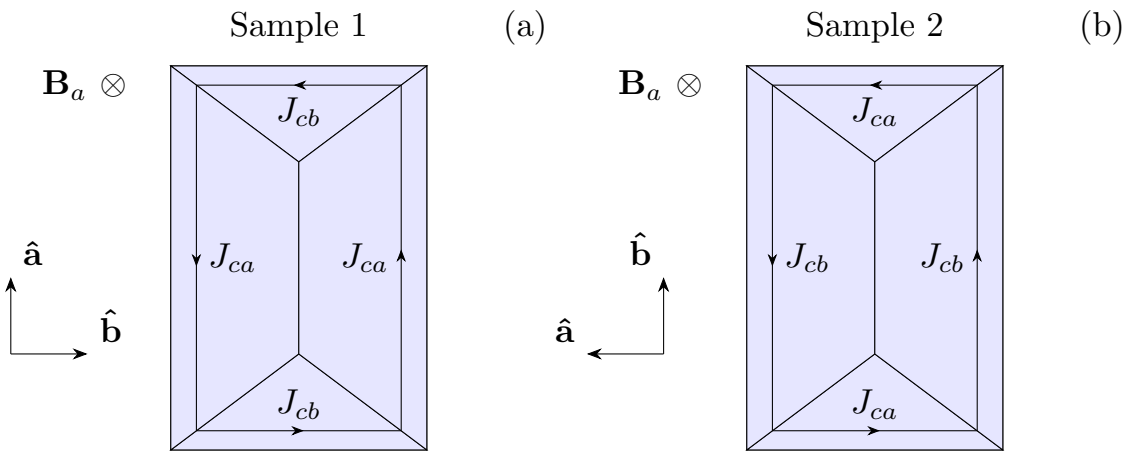


Figure 3.14 Current configurations in samples with crystallographic J_c anisotropy. (a) m_a and (b) m_b. The uniform blue shading indicates there is no partition containing force-free currents (as opposed to figure 3.2, where force-free currents are represented by red shading).

experimental protocol. Looking at figure 3.3, we can notice that it is necessary to have one measurement where J_{c1} (J_{c2}) is parallel (perpendicular) to the sample's long edges (this corresponds to m_h) and one measurement where J_{c1} (J_{c2}) is parallel (perpendicular) to the sample's short edges (this corresponds to m_v). This is done by physically rotating the sample in cases where only force-free effects need to be considered, but the equivalent is not possible in the case of crystallographic anisotropy. Assuming a thin sample with the c-axis parallel to $\hat{\mathbf{n}}$ and with J_c anisotropy in the ab plane, two samples of identical geometry but with a $\pi/2$ angular offset of the a and b axes are needed, as shown in figure 3.14 (notice the orientation of the a and b axes with respect to the sample outline). Practically speaking, this could be done by cutting two rectangular samples from the same tape, where the outline of the second sample is rotated by $\pi/2$ with respect to the first (we assume that the tape has good enough J_c uniformity along its length).

Figure 3.14 shows how these samples could be configured for a QSFM experiment. Let us first consider the case with B_a perpendicular to the sample. In these circumstances, there are no force-free effects. There are two critical current densities: J_{ca} in the direction parallel to the a-axis and J_{cb} in the direction parallel to the b-axis. We define m_a (m_b) as the m measurement where J_{ca} (J_{cb}) is parallel to the sample's long edges, where m_a (m_b) can be seen as the equivalent of m_h (m_v). The configurations corresponding to m_a and m_b are shown in figures 3.14 (a) and (b) and the formalism discussed in section 3.1 can be used to find J_{ca} and J_{cb}. When force-free effects are not present, only two measurements are necessary.

When force-free effects and crystallographic anisotropy are involved, four different con-

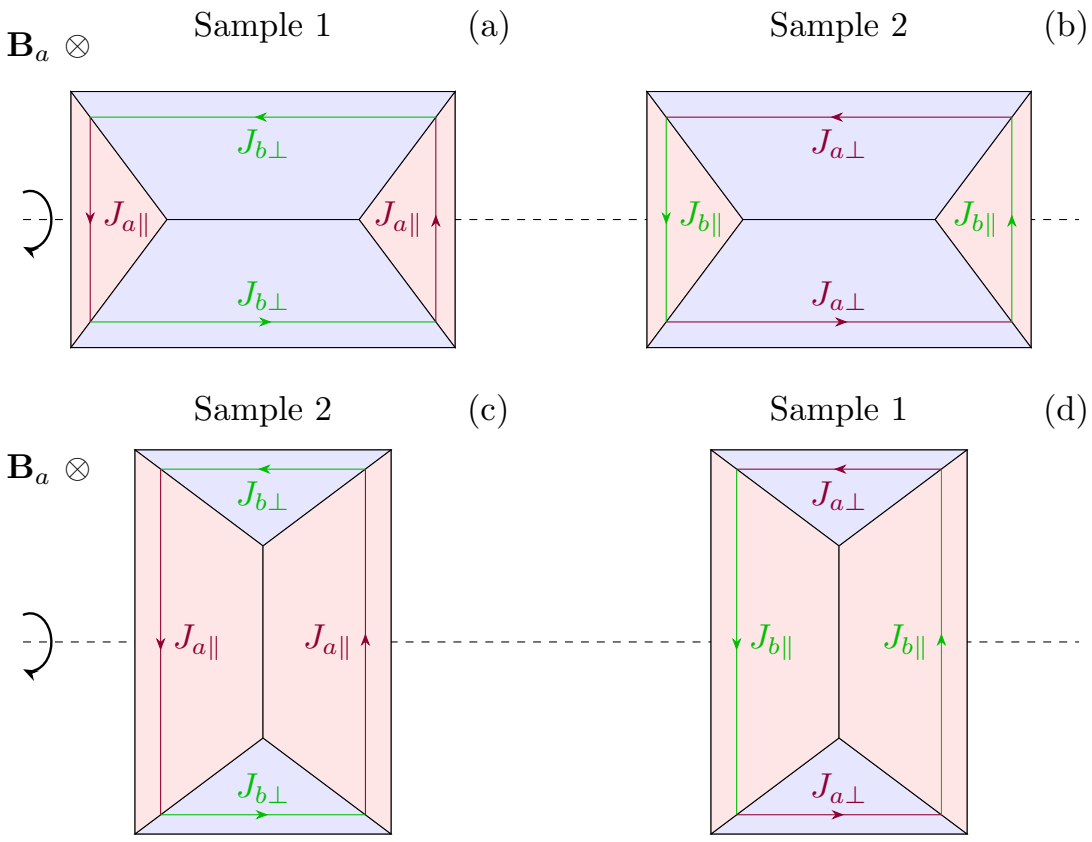


Figure 3.15 Current configurations in samples with crystallographic and force-free J_c anisotropy. (a) m_{hb}, (b) m_{ha}, (c) m_{va}, and (d) m_{vb}. The blue shading is associated to regions where the current is perpendicular to B_a and the red shading is associated to regions where force-free effects are present.

figurations must be used because there are four unknown J_c distributions, which are $J_{a\perp} = J_{ca}(B, \varphi_\perp)$, $J_{a\parallel} = J_{ca}(B, \varphi_\parallel)$, $J_{b\perp} = J_{cb}(B, \varphi_\perp)$, and $J_{b\parallel} = J_{cb}(B, \varphi_\parallel)$. For every probed θ, a total of four measurements must be made (two for each sample). We label these measurements m_{ha}, m_{hb}, m_{va}, and m_{vb}, where the first subscript is noted with the same convention as in section 3.1 (i.e. h is used when the long edges are perpendicular to B_a and v is used when the short edges are perpendicular to B_a) and the second subscript indicates which crystal axis is parallel to the long edge of the sample (see the labels in figure 3.15). To calculate $J_{ca}(B, \varphi_\perp)$ and $J_{cb}(B, \varphi_\parallel)$, the formalism previously introduced must be used with m_{ha} and m_{vb} (see figures 3.15 (b) and (d)). To calculate $J_{ca}(B, \varphi_\parallel)$ and $J_{cb}(B, \varphi_\perp)$, the formalism must be used with m_{hb} and m_{va} (see figures 3.15 (a) and (c)).

3.4.2 Interpretation of QSFM Results With Non-Ideal Samples

When dealing with commercial samples, some additional non-idealities might need to be considered, e.g., a tilt angle between the c axis and $\hat{\mathbf{n}}$, non-isotropic pinning, etc. While our QSFM method remains valid, more nuance can be brought to how the results should be interpreted. We distinguish between non-idealities which conserve a 180° symmetry of J_c and those that do not. This distinction is important as J_{c1} and J_{c2} partition pairs have antiparallel currents and their norms remain the same if there is 180° symmetry.

The case of a symmetry-conserving non-ideality can be described with the condition $J_c(B,\theta) = J_c(B,\theta+\pi)$. When this is true for the two J_{c1} currents and the two J_{c2} currents (as shown in figure 3.1 (b)), then both antiparallel J_{c1} partitions and both antiparallel J_{c2} partitions respectively have the same local J_c. In these circumstances, the calculated J_c values can be interpreted to be accurate as they are. While symmetry-conserving non-idealities are not common, we bring up this discussion for the sake of completeness.

A non-ideality that causes $J_c(B,\theta) \neq J_c(B,\theta+\pi)$ is, for example, the asymmetry of the materials in contact with the top and bottom of the superconducting layer [75]. This affects J_c prominently when B_a is parallel or almost parallel to the ab planes. Looking at J_{c1}, the Lorentz forces acting on the two antiparallel currents are also antiparallel and drive the vortices towards opposing sample surfaces, which are in contact with different materials. This makes the local J_{c1} different in both regions, as factors like the lattice mismatch differ and alter the local pinning potential. This effect can be observed in figures 1, 2, and 5 of reference [76] and in figure 3 of reference [75].

Considering this kind of asymmetry, there are potentially four different J_c values in the sample at the same time. As a first approximation and assuming that there are different materials on the top and bottom surfaces of the superconducting layer, the calculated J_{c1} could be considered as an average of the currents experiencing top and bottom surface pinning potentials. This approximation would be most appropriate when B_a is close to parallel to $\hat{\mathbf{n}}$ and this effect is less prominent. For an exact resolution, however, four different J_c and α values must be considered and a more adapted formalism should be used.

CHAPTER 4 CALCULATING J_c FROM PULSED FIELD MAGNETIZATION MEASUREMENTS IN PERPENDICULAR FIELDS

Our second sub-objective is to develop a new methodology to calculate J_c in perpendicular fields with pulsed field magnetization (PFM). Like QSFM, PFM consists in placing a sample in a magnetic field and measuring its magnetic moment. The main differences are due to the large $\partial B/\partial t$ and are that

- inductive voltages are large enough that the Bean model is not valid anymore,
- significant screening currents are induced in the non-superconducting layers of the sample, and
- heat generation and diffusion are significant.

Calculating J_c analytically would therefore not be straightforward and we elect to make use of the FEM. The following chapter presents our proposed J_c calculation method for samples in perpendicular fields. We recognize that there are many experimental challenges to overcome and we therefore chose to test our method with numerically generated data. Section 4.1 goes over preliminary PMF measurements, section 4.2 goes over our calculation method, section 4.3 goes over the results obtained with numerical data, and section 4.4 discusses the limitations of the method and future perspectives.

4.1 Preliminary Measurements

4.1.1 PFM Experimental Method

The method that was used is described in detail in [77, 78], and we shortly summarize it. A qualitative magnetic probe is shown in figures 4.1 (a) and (b). In essence, the setup is similar to the one in a VSM with the difference that the sample and the pickup coils remain stationary during measurements. The sample is placed inside an ampule that is mounted at the end of a G10 rod. This rod is inserted into a hollow G10 cylinder, at the bottom of which are fixed the pickup coils. Both are placed inside a cryostat (not shown) and the rod can be slid in and out of it while the cryostat, the hollow G10 cylinder and the pickup coils remain fixed. We discriminate between the "sample-in" position, where the sample is at the centre of the main pickup coil, and the "sample-out" position, where the sample is away from the pickup coil. The use of these positions is explained below. Let it be noted that the sample's field decays rapidly with distance and its $\partial B/\partial t$ contribution to the measured voltage is negligible in the "sample-out" position.

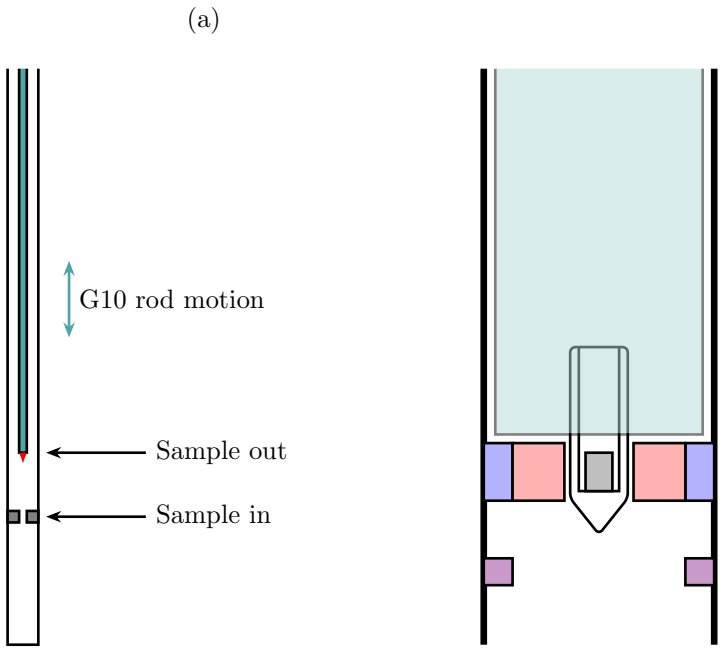


Figure 4.1 Qualitative magnetic probe. (a) View of the sample positions. The red triangle represents the ampule carrying the sample and the shaded squares are the pickup coils. (b) Zoom on the "sample-in" position. The blue and red shaded blocks are the pickup coil, where the different shades indicate opposing winding directions. The purple shaded blocks represent the compensation coil. The grey shaded block represents the stack of samples. The ampule is slid into the G10 rod and is set in place with GE varnish.

While no signal could be measured with this setup in a DC field, the short timescale of the sample's magnetization produces a large enough flux variation to induce a readable voltage in the pickup coil. That being said, the sample's $\partial B/\partial t$ is usually very small compared to the pulsed magnet's $\partial B/\partial t$ and the pickup coil must be designed with this in mind. To isolate the sample's contribution, a first set of turns is wound in a given direction and then another set of turns is counter-wound over it (respectively the red and blue shaded blocs in figure 4.1 (b)). The number of turns in each set is chosen such that their respective voltage contributions cancel out in a uniform $\partial B/\partial t$. Considering that the applied field is approximately uniform (the pickup coil is small compared to the magnet bore's length) and the sample's field is not, the coil only sees the sample's contribution.

In practice, however, it is very hard to totally cancel out the magnet's $\partial B/\partial t$ for the whole pulse length. This is mitigated, firstly, by adding an additional compensation coil in the vicinity of the main pickup coil in series with a potentiometer that is tuned to make the magnet's signal as flat as possible (purple shaded blocs in figure 4.1 (b)). Secondly, a signal is recorded in the "sample-out" position and is subtracted to signals recorded in the

"sample-in" position. This is equivalent to subtracting the background field such that only the sample's contribution is left.

To account for all the points made previously, the measurement procedure to get a major hysteresis cycle is as follows:

1. Zero field cool (ZFC).
2. Compensation coil tuning.
3. Optimization of the sample position (this is done to make sure the sample is in the centre of the pickup coil and to maximize the measured signal).
4. "Sample-out" pulse with $B_z > 0$.
5. "Sample-in" pulse with $B_z < 0$.
6. "Sample-in" pulse with $B_z > 0$.
7. "Sample-out" pulse with $B_z < 0$.

Let us point out that we do not perform a ZFC between each measurement and the sample still goes through the magnetization process even in the "sample-out" position (the sample is still in the magnet bore). This is fine since we are only interested in the magnetization data from the major hysteresis cycle. It can also be added that time is taken between pulses to let the sample cool down back to its initial temperature (in fact, the magnet also needs to cool down between pulses). Finally, the field polarity is reversed at every pulse, as we want the state of magnetization to remain on the major hysteresis cycle (as opposed to causing the current direction to be reversed at the start of the pulse).

4.1.2 Preliminary Experiment Results and Takeaways

The samples used were cut from the same tapes as in section 3.2. To have a large enough signal, ten rectangular cutouts were stacked and they were mounted in a small ampule sealed with vacuum grease. The ampule has a 1 mm diameter and the samples are hand-cut squares with 0.7 mm sides. The individual samples are shown in figure 4.2 (a) and the ampule containing the sample stack is shown in figure 4.2 (b). While the samples do not precisely have the same dimensions, we proceed with the experiment as our aim is qualitative in nature. Measurements presented in this section were done at 4 K with a 30 T peak field. Figure 4.2 (c) shows the field's waveform. The obtained hysteresis loop is displayed in figure 4.2 (d) and was calculated by integrating in time the measured voltage. We do not calibrate our measurements as we only seek qualitative information. That being said, the

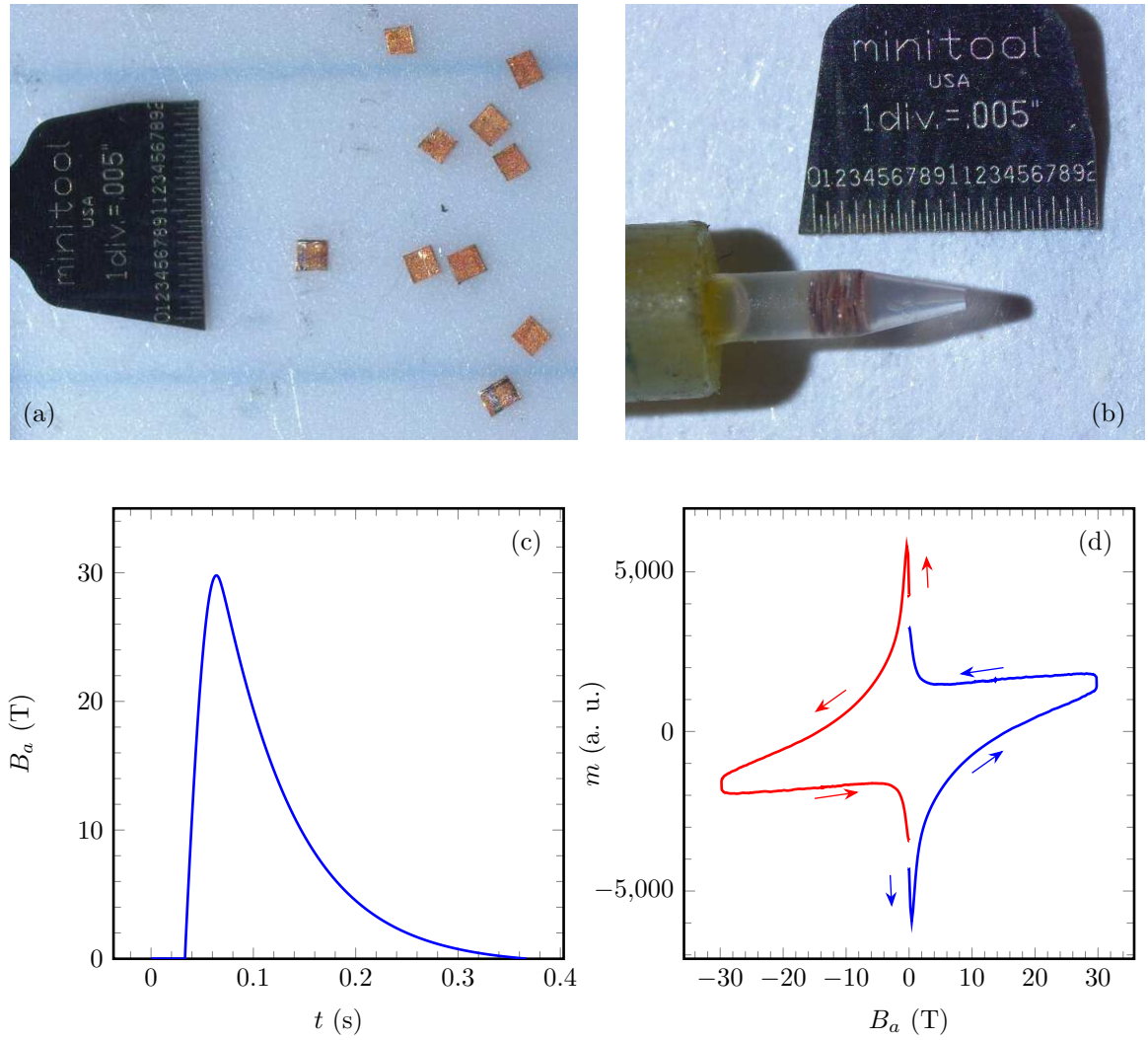


Figure 4.2 Samples and preliminary experimental results. (a) Samples before placement in the ampule. The samples are cut to be as close as possible to squares with 0.7 mm sides to fit in the ampule. (b) Sample stack in the ampule. Ten samples are stacked to have a large enough signal. The samples are placed inside the ampule first, and are then sealed in with vacuum grease. The ampule is inserted inside the end of the G10 rod and is fixed in place with GE varnish. The ampule has a 1 mm diameter. (c) Applied field waveform. (d) Hysteresis loop for $|B_a| \leq 30$ T and in arbitrary units. The blue curve was measured from a $B_z \geq 0$ pulse and the red curve was measured from a $B_z \leq 0$ pulse. The arrows indicate the direction of time evolution. The vertical offset between curves is added for visualization purposes as it cannot be calculated from voltage integration. For a given pulse, it can be noticed that the top and bottom branches are not symmetric with respect to the x-axis and that $m(B = 0, t_0) \neq m(B = 0, t_e)$.

measurement can be calibrated by measuring the voltage in the pickup coil while a sample with a well-known m is used, as described in [78].

Let us define t_0 and t_e, respectively the beginning and end times of a given pulse. Firstly, it can be seen that $m(B)$ is not symmetric about the x-axis. Secondly, $m(B = 0, t_0) \neq m(B = 0, t_e)$ (opposite offsets of equal norm are imposed on the top and bottom branches for visualization purposes as m can only be calculated down to a constant). We deduce the following from these observations:

1. The reversible contribution M_r from non-superconducting sample layers or other nearby magnetic materials cannot be neglected since the top and bottom branches associated to a given pulse are in the same quadrant for fields greater than a given threshold. Indeed, heating could have been assumed to be the cause for asymmetry about the x-axis if the top and bottom branches were respectively in the top and bottom quadrants during the whole pulse, as the "worst case" limit $T \to T_c$ leads to $J_c \to 0$. In such scenarios, branches cannot cross into another quadrant and a similar statement could be made about screening currents in non-superconducting layers. That being said, the need to consider M_r is sample dependent. For instance, the measurements presented in figure 3 of reference [78] do not have to take this into account. Similar reversible magnetization can, however, be seen in references [10, 11].

2. Heating and screening currents in non-superconducting layers cannot be neglected. Indeed, if $m(B = 0, t_0) \neq m(B = 0, t_e)$, then $J_c(B = 0, t_0) \neq J_c(B = 0, t_e)$ and the variation in J_c cannot be due to reversible contributions, since $B_a(t_0) = B_a(t_e)$ (assuming there are no hysteretic materials aside from the superconductor). This is validated numerically in the following sections.

It is therefore obvious that J_c follows a non-reversible path on the $J \times B \times T$ critical surface (i.e. J_c does not "retrace its steps" after the pulse peak). A complete algorithm that calculates this $J_c(B(t), T(t))$ path must do so whilst dealing with the previous points. That being said, focus is only brought to the latter of these points i.e. dealing with heating in the sample and the screening currents from non-superconducting sample layers. Indeed, dealing with M_r requires that we know how to accurately extract the magnetic susceptibility χ_m from M_r, such that magnetization can be computed locally in our simulations. This would prove very hard and require a dedicated optimization process as our samples are not ellipsoids (recall that the demagnetizing field is only uniform in ellipsoids) and the thickness of the superconducting layer is artificially scaled to improve convergence (i.e. the sample cannot be approximated by the thin planar ellipse limiting case). We leave this aspect for future work.

4.2 Algorithm Derivation for J_c Calculations with PFM

4.2.1 FEM Model Definition for PFM

Similarly to what was done in section 4.1, a preliminary numerical experiment was done to better understand the behaviour of our system. This section therefore starts with the definition of our FEM model, which was done in Comsol Multiphysics 6.2 with the AC/DC, Mathematics, and Heat Transfer in Solids modules.

The geometry that is used is displayed in figure 4.3 (a). We assume the sample is cylindrical, enabling us to use an axisymmetric model. The sample is parallel to the azimuthal plane and is made up of, from top to bottom, a copper layer (20 µm, purple shading), a superconducting layer (1.6 µm before scaling, green shading), a hastelloy layer (50 µm, navy shading), and another copper layer (20 µm) (the dimensions are chosen to resemble the specifications listed in [79]). The sample has a diameter of 0.7 mm, which matches the side length of the samples in the preliminary experiment. B_a is parallel to $\hat{\mathbf{z}}$ and has a triangular waveform. We chose to use a power law E-J constitutive equation. We note that the power law is better suited for the numerical modelling of PFM than QSFM, as the large $\partial B/\partial t$ involved induces large enough electric fields to have $J \approx J_c$. For the sake of simplicity, we chose J_c and thermal properties to be isotropic and an adiabatic boundary between the sample and its surrounding environment. We assume that the electrical and thermal properties of the non-superconducting layers are known and that the superconductor is YBCO.

We implement the H-ϕ formulation, where Ω_c is the sample (including all the non-superconducting but conducting layers) and Ω_{nc} is the surrounding domain. A detailed implementation example is given in references [65, 69] (both presenting the same example). The mesh that was used is presented in figure 4.3 (b). The element sizes are chosen such that they are roughly uniform and square in the sample. Note that current can be shared between layers in this configuration, as opposed to the model that was presented in section 3.3.1. To avoid skewed elements in the mesh and improve convergence, the superconducting layer's thickness is scaled by a factor $\gamma > 1$. The same can be done for other layers but it is not necessary here as only the superconducting layer has a high aspect ratio. When scaling is involved, the resistivity associated with the power law E-J constitutive equation reads

$$\rho = \frac{\gamma E_c}{J_c}\left(\frac{\gamma J}{J_c}\right)^{n-1}. \tag{4.1}$$

The mass density ρ_m and the heat conductivity κ are scaled such that $\rho_m \to \rho_m/\gamma$, $\kappa_{r,\vartheta} \to \kappa_{r,\vartheta}/\gamma$, and $\kappa_z \to \gamma\kappa_z$ (the subscripts r and ϑ designate the radial and azimuthal components).

The critical current density is modelled such that $J_c = J_c(B, T)$. To have quantities

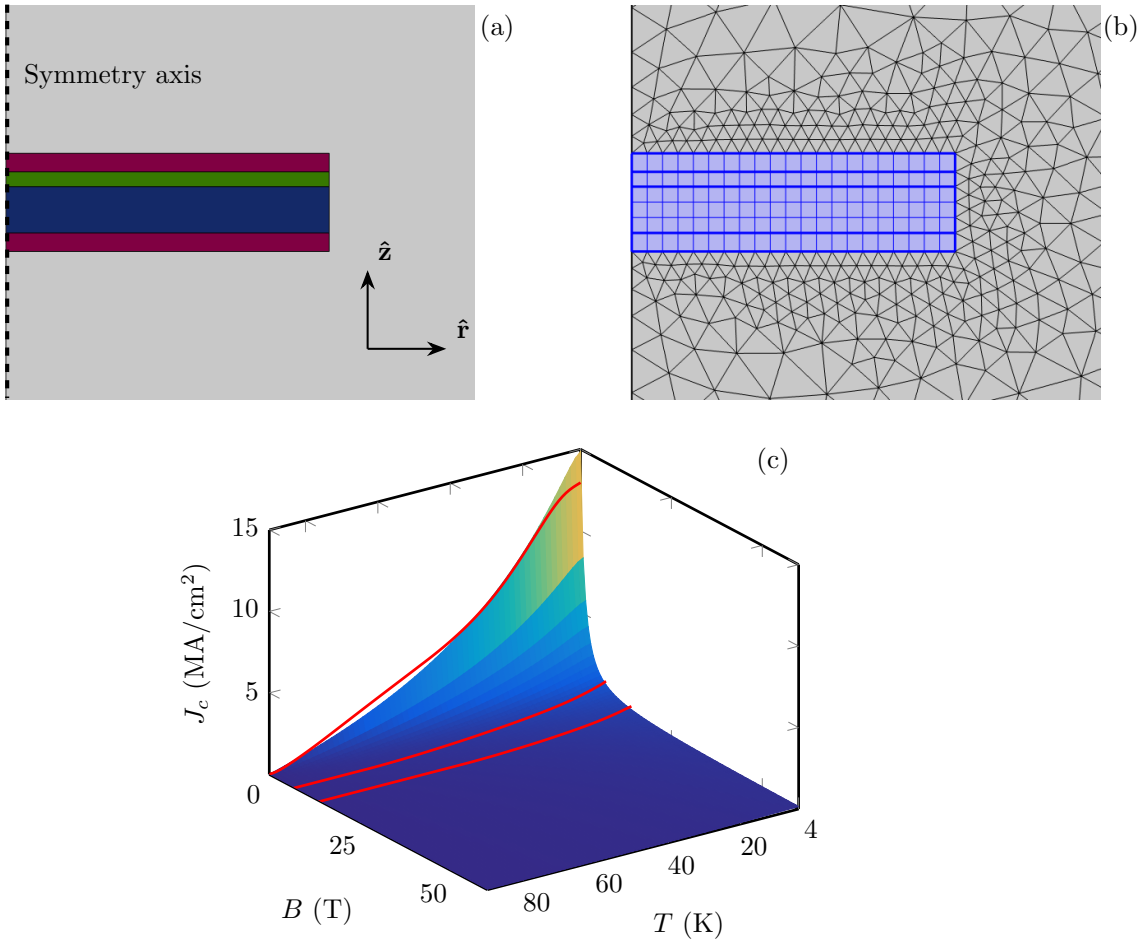


Figure 4.3 Model definition. (a) Sample cross-section in cylindrical symmetry. The dashed line represents the symmetry axis. The purple, green, and navy layers respectively are the copper, superconducting, and hastelloy layers. (b) Geometry mesh. (c) $J \times B \times T$ critical surface. The red curves represent the $J_c(B,T)$ distributions calculated from equation (2.26), with $B = 0$ T, 7 T, and 14 T.

that are representative of reality, we have calculated $J_c(B,T)$ using traditional QSFM with a 2.12×3.09 mm^2 sample cut from the same tapes as the samples used above. Magnetic moment data $m(B,T)$ were measured for 4 K $< T <$ 95 K and $B = 0$ T, 7 T, and 14 T. Then, J_c was computed with equation (2.26), and the data was fit to a product of Padé approximants that we propose and is given by

$$J_c(B,T) = J_{c0}\left(\frac{B_1B^2 + B_2B + B_3}{B_4B^3 + B_5B^2 + B_6B + B_7}\right)\left(\frac{T_1T^2 + T_2T + T_3}{T_4T^3 + T_5T^2 + T_6T + T_7}\right)\left(1 - \frac{T}{T_c}\right), \quad (4.2)$$

with $T_c = 90$ K. The goal of this curve fit is to generate a realistic critical surface that can eventually be used for reference simulations. Our choice of equation is inspired by the

rough $1/B$ Kim model dependence. The orders of the polynomials (for both B and T) are chosen such that $p - q = 1$ (p is the order of denominator polynomials and q is the order of numerator polynomials), allowing for the possibility to find a Kim-like law by a fitting algorithm, whilst having a richer function space. Good agreement is found and the result is presented in figure 4.3 (c), where the surface represents equations (4.2) and the red curves represent J_c calculated from our $m(T)$ measurements. The T/T_c term is added to make sure $J_c(B = 0, T)$ is zero in the vicinity of T_c. Let us note that, rigorously speaking, we should not use equation (2.26) to compute $J_c(B = 0, T)$ because we are not in the high-field regime. However, we only want a general idea of the J_c landscape at low fields and we can move forward without optimal accuracy.

4.2.2 Assumptions and Algorithm Presentation

Table 4.1 presents the parameter values that were used for our preliminary numerical experiment. The pulse length $\Delta t = t_e - t_0$ (since the waveform is triangular, $B_a(t_0) = B_a(t_e) = 0$ T) and the peak field B_{pk} are chosen such that they match what can be generated by the long pulse magnet at the pulsed field facility of the National High Magnetic Field Laboratory in Los Alamos [80]. Three observations can be made.

- T is uniform throughout the sample for the whole length of the pulse. This is shown in figure 4.4 (a).
- The magnetic moment due to screening currents in copper is significant compared to the magnetic moment of the superconducting layer (purple curve in figure 4.4 (b)).
- J_c follows an irreversible path in the $J \times B \times T$ space. This is shown in figure 4.4 (c), where the path was calculated by plugging $B_a(t)$ and the average temperature $\langle T(t) \rangle$ (computed during the simulation) in equation (4.2).

Table 4.1 Preliminary simulation parameters.

Parameters	Values
γ	10
E_c	1 µV/cm
n	30
J_{c0}	13.2 MA/cm^2
B_i ($i = 1$ to 7)	0.864, 1.42, 1.61, -2.96, -3.07, -7.69, -3.40
T_i ($i = 1$ to 7)	-8.93, -3.41, 1.45, 0.0761, 3.03, 2.01, 0.977
B_{pk}	60 T
T_0	4 K
Δt	2 s

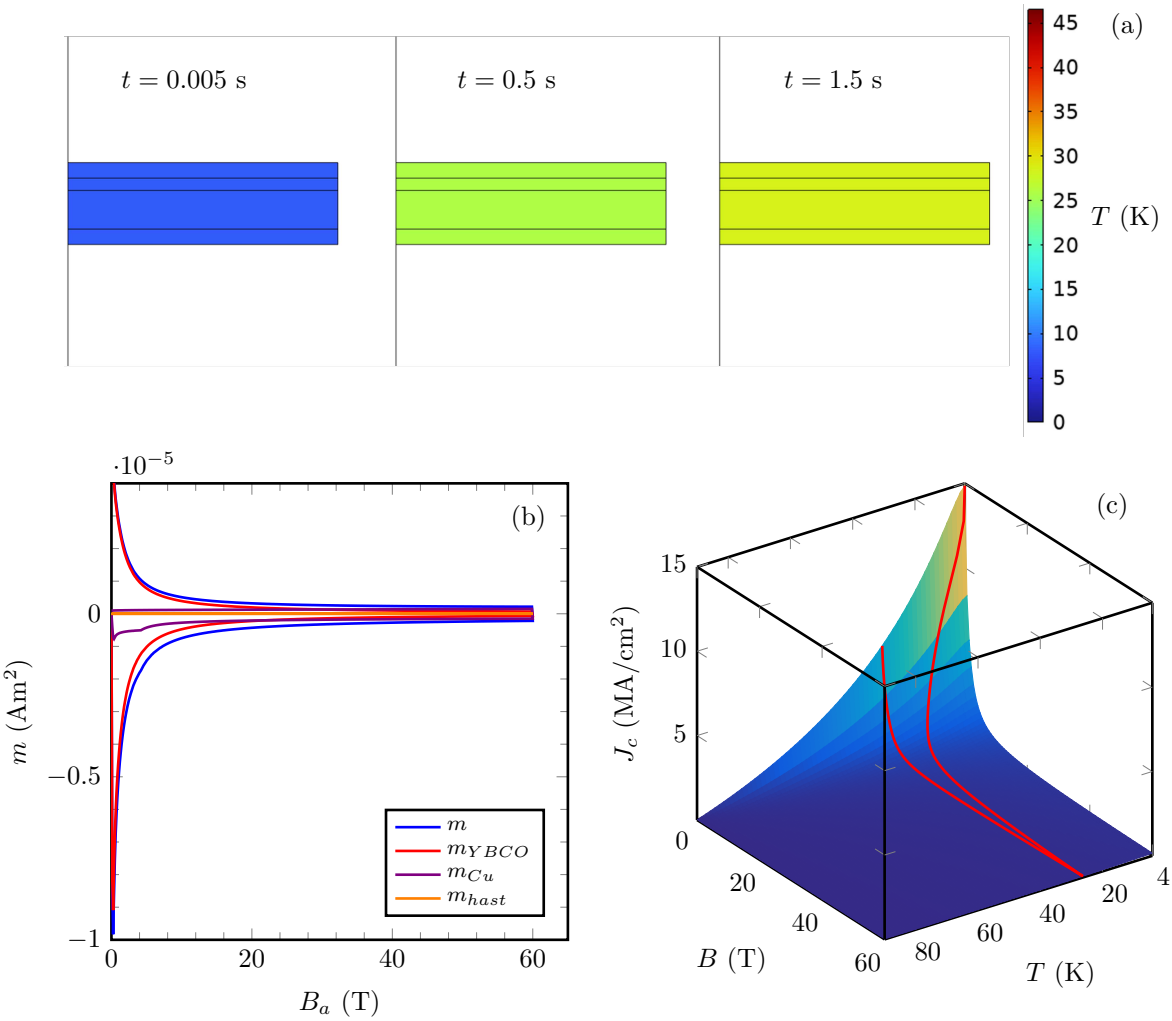


Figure 4.4 Preliminary numerical results. (a) Temperature across the sample's cross-section for $t = 0.005$ s, 0.05 s, and 1.5 s. (b) Magnetic contributions from the copper, hastelloy, and superconducting layers. (c) $J_c(B(t), T(t))$ path in the $J \times B \times T$ space.

These observations guide the derivation of the method we propose. The observations confirm the hypothesis made from our experimental results that heating and screening currents are significant (note that $m(B = 0, t_0) \neq m(B = 0, t_e)$ in figure 4.4 (b) and that $J_c(B = 0, t_0) \neq J_c(B = 0, t_e)$ in figure 4.4 (c)).

Before moving forward, let us recall the definition of m due to screening currents and also introduce the normalized magnetic moment m_n (with units in m^4), which have the definitions

$$m = \frac{1}{2}\int_V \mathbf{r} \times \mathbf{J} d^3r, \quad m_n = \frac{1}{2}\int_V \frac{\mathbf{r} \times \mathbf{J}}{J_c(B,T)} d^3r. \tag{4.3}$$

One can first notice that, since $B(\mathbf{r}, t) \approx B_a(t)$ and $T(\mathbf{r}, t) \approx \langle T(t) \rangle$, $J_c(B, T)$ is roughly

uniform in the sample and can be taken out of the integral. This makes it possible to compute J_c with

$$m_n = \frac{m}{J_c}, \quad \Rightarrow J_c = \frac{m}{m_n}, \tag{4.4}$$

provided that m is only composed of the superconductor's magnetic response. In these circumstances, J_c can be calculated without having to use an iterative algorithm. While this is not true for the rest of this work because of the other conducting layers that must be considered, we nonetheless note that a good approximation of J_c can be obtained with this method. Let us note that, while m_n might not seem useful since we do not know J_c *a priori*, m_n is in fact not dependent on J_c. As it turns out, m_n can be derived for cylindrical samples magnetized in perpendicular fields. Using Faraday's law in integral form, the relationship between the electric field and $\partial B/\partial t$ for a path concentric to the sample's perimeter can be derived. For a circular path of radius r, this relationship can be shown to be

$$E = -\frac{r}{2}\frac{\partial B_a}{\partial t}. \tag{4.5}$$

We note that E is always tangential to the integration path in virtue of the problem's symmetry and that $\partial B/\partial t \approx \partial B_a/\partial t$ when in the high-field regime, which in turn implies that the field variation is roughly uniform over the integration area. Using the power law constitutive equation $E = E_c(J/J_c)^n$ and taking the norm, the ratio J/J_c at a radius r is given by

$$\frac{J}{J_c} = \left(\frac{r}{2E_c}\frac{\partial B_a}{\partial t}\right)^{1/n}. \tag{4.6}$$

Figure 4.5 (a) shows the simulated behaviour of the ratio J/J_c along the sample radius and in time. We can first notice that the numerical curves are in near perfect agreement with equation (4.6). Also, the J/J_c ratio remains constant in time, as all the curves shown are virtually indistinguishable (except for numerical artifacts). This explains why $|m_n|$ is constant for a given set of experimental parameters (a triangular waveform is assumed for the field, and n and E_c are constant), as can be seen in figures 4.5 (b) and (c). In this situation, $|\mathbf{r} \times \mathbf{J}| = rJ$ and an expression for m_n can be derived. We have

$$\begin{aligned} m_n =& \frac{1}{2}\int_0^d \int_0^{2\pi} \int_0^R r\left(\frac{r}{2E_c}\frac{\partial B_a}{\partial t}\right)^{1/n} r\mathrm{d}r\mathrm{d}\vartheta\mathrm{d}r \\ =& \pi d\left(\frac{1}{2E_c}\frac{\partial B_a}{\partial t}\right)^{1/n}\left(\frac{R^{3+1/n}}{3+1/n}\right), \end{aligned} \tag{4.7}$$

where R is the sample's outer radius and ϑ is the azimuthal angle in the cylindrical reference frame that is used.

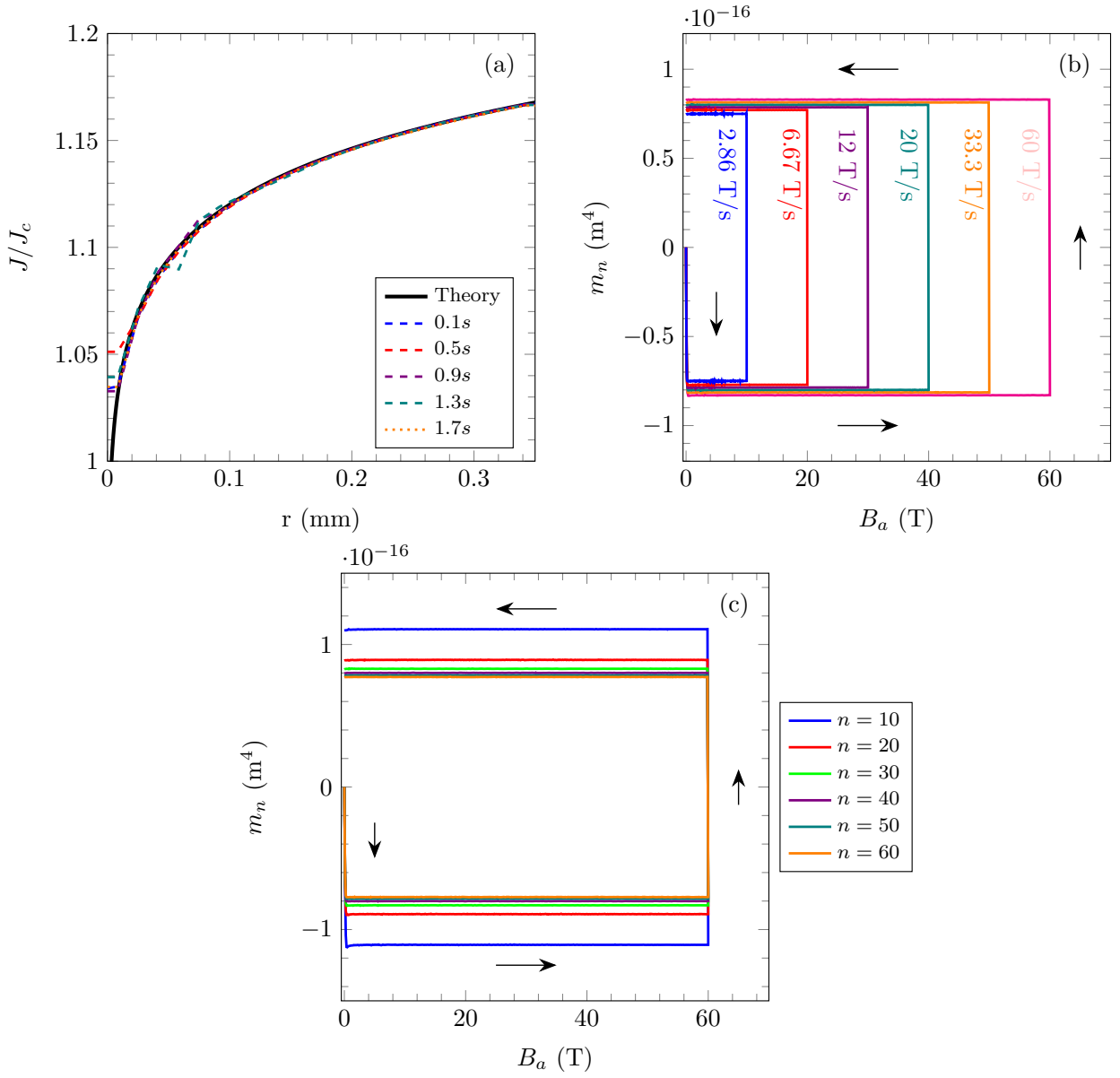


Figure 4.5 Behaviour of the current profile and the normalized magnetic moment m_n. (a) J/J_c ratio along the sample radius r. (b) m_n hysteresis loops for $n = 30$ (fixed) and $\partial B_a/\partial t = 2.86$ T/s, 6.67 T/s, 12 T/s, 20 T/s, 33.3 T/s, and 60 T/s. (c) m_n hysteresis loops for $\partial B_a/\partial t = 60$ T/s (fixed) and $n = 10$, 20, 30, 40, 50, and 60.

It can be seen that m_n remains constant if the applied field ramp and n are constant. Increasing or decreasing $\partial B_a/\partial t$ by an order of magnitude changes m_n by a factor $10^{1/n}$. Going from a QSFM experiment (where $\partial B/\partial t$ is usually at most 10 mT/s with a typical VSM) to a PFM experiment (where $\partial B/\partial t$ can go up to $\approx$ 1000 T/s) with $n = 30$, a change of $\approx$ 47% in m_n (and m) occurs. Figure 4.5 (b) shows m_n hysteresis loops for different $\partial B_a/\partial t$ values that are realistic for the long pulse magnet. It can also be seen that m_n is approximately proportional to $(\partial B/\partial t)^{1/n} R^{1/n}$ and this behaviour is displayed in figure 4.5 (c). As n increases, m_n decays while converging to a certain value, which would be the Bean model m_n value. Looking at figure 4.4 (c) and figures 4.5 (b) and (c), we can see that m_n is more or less constant in a variety of circumstances, where the state of the sample takes a complex path on the $J \times B \times T$ critical surface. It can also be noticed that J_c never appears in equation (4.7), which indicates that m_n is independent of the J_c distribution used as a simulation input.

Because of the facts that the magnetic responses of the different layers are coupled to each other and that $J_c(B,T)$ must be entered as an input in the simulation (i.e. we are forced to make a guess), we are constrained to use an iterative approach. We leverage m_n and propose the following simple algorithm:

1. Set the initial guess $J_c^{(1)}(t)$, the power law n value, and stop criterion.
2. Simulate the sample's magnetization and extract $m_{Cu}^{(i)}(t)$, $m_{hast}^{(i)}(t)$, $m_n^{(i)}(t)$, and $\langle T(t)\rangle^{(i)}$.
3. Evaluate $J_c^{(i+1)}(t)$ with

$$J_c^{(i+1)}(t) = \frac{m_{exp}(t) - m_{Cu}^{(i)}(t) - m_{hast}^{(i)}(t)}{m_n^{(i)}(t)}. \tag{4.8}$$

4. Repeat steps 2 and 3 until the stop criterion is met.
5. Use $B_a(t)$ and the last $J_c^{(i)}(t)$ and $\langle T(t)\rangle^{(i)}$ to plot the sample's path in the $J \times B \times T$ thermodynamic space.

The variables $m_{exp}(t)$, $m_{Cu}^{(i)}(t)$, $m_{hast}^{(i)}(t)$, and $\langle T(t)\rangle^{(i)}$ are respectively the experimentally measured magnetic moment of the whole sample, the numerically calculated magnetic moment of the copper layers, the numerically calculated magnetic moment of the hastelloy layer, and the numerically calculated average temperature. The exponent i is the current iteration. Let us note that, in the following sections, $m_{exp}(t)$ is generated with a reference simulation instead of a real measurement. It can also be noticed that the n value must also be chosen as an input. This choice was made as magnetization measurements are not well suited for n value

calculations. The error related to the choice of n and the possibilities for its measurement are discussed in a later section.

4.3 Results Using Numerically Generated Reference Data

The parameters used for the numerically generated $m_{exp}(t)$ are the same as in table 4.1. We choose $J_c^{(1)}(t) = 10^{12}$ A/m^2 (constant in time) as an initial guess (we choose this constant J_c in virtue of the tentative assumption that m_n is independent of the J_c choice). We intentionally make our initial guess such that $J_c^{(1)}(t) > J_{c,exp}(t)$, where we force the superconductor to dominate the sample's response. This is done to avoid having, e.g., $J_c^{(1)}(t_1) \leq J_{c,exp}(t_1)$ and $J_c^{(1)}(t_2) \geq J_{c,exp}(t_2)$ (with $t_2 > t_1$).

The results are presented in figure 4.6. Figure 4.6 (a) shows the $J_c(B(t), T(t))$ path in the $J \times B \times T$ space, where the dashed red curve was obtained by our method and the black curve is the reference curve (also shown in figure 4.4 (c)). The agreement that was obtained is excellent, except for the very beginning. This is expected since m_n is initially zero (there is no current in the sample) and $J_c^{(i)}$ explodes. One can notice from the path that most of the heating occurs close to the beginning of the pulse and when J_c is large. This can also be seen in figure 4.6 (b), where the slope of the temperature tapers off when $t \approx 0.1$ s.

Figures 4.6 (c) and (d) show the bottom quadrants of m_{tot} (the magnetic moment of the whole sample) and m_{Cu} for the first few iterations. The very first iteration is excluded, because $J_c^{(1)}$ is purposely chosen such that m_{SC}, the magnetic moment of the superconducting layer, dominates. From both figures, we can see that m_{tot} and m_{Cu} converge from opposite directions to their final values. This is a consequence of the fact that we chose $J_c^{(1)}(t) \gg J_{cexp}(t)$. This entails that the magnetic response is dominated by the superconductor, which produces a field that opposes the applied field and attenuates the local field variation seen by the copper (and other) layers. For a given iteration i, this means that $m_{Cu}^{(i)}$ is smaller than its real value and that $J_c^{(i+1)}$ has to be larger than its real value. This trend is conserved across iterations and prevents oscillations around the real distributions. Therefore, m monotonically decreases in norm and m_{Cu} monotonically increases as $J_c^{(i)}$ converges towards its real value.

Figure 4.6 (e) shows the evolution of the average error (averaged over time) for m_{tot} (blue points), J_c (red points), and $\langle T \rangle$ (purple points) as a function of the iteration. Using the data points at $i = 2$ and $i = 10$ and the equation

$$-p = \frac{\log(\epsilon(i = 10)) - \log(\epsilon(i = 2))}{\log(10) - \log(2)}, \tag{4.9}$$

we get convergence orders of 2.91, 1.66, and 2.94 for the average error on $m_{tot}(t)$, $J_c(t)$, and $\langle T(t) \rangle$, where ϵ is the average error for the chosen quantity. We chose these points as our

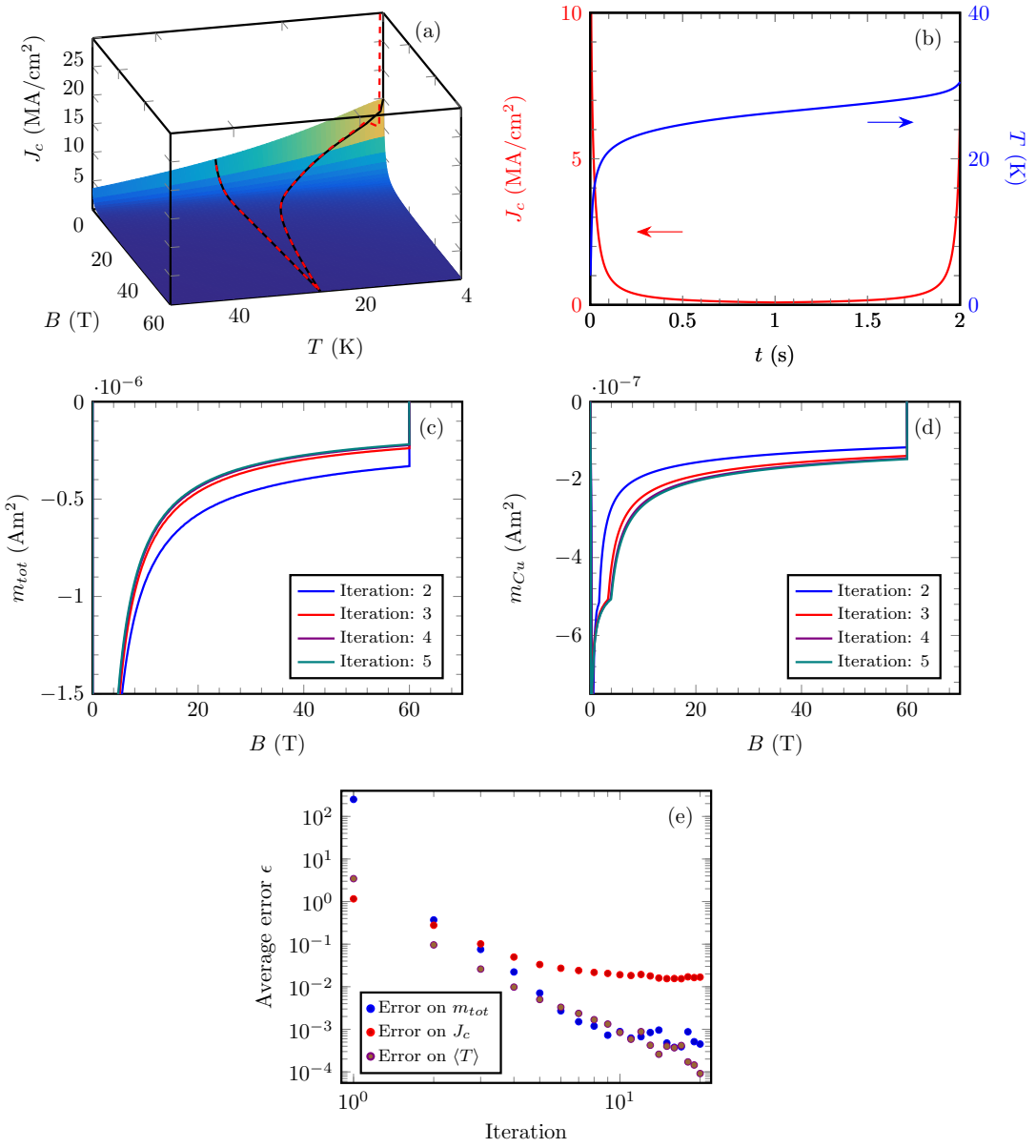


Figure 4.6 PFM algorithm results and performance. (a) $J_c(B(t), T(t))$ in $J \times B \times T$ space. The black curve is the reference path and the dashed red curve was obtained from the PFM algorithm. (b) 1D plot of $J_c(t)$ (red curve) and $\langle T(t) \rangle$ (blue curve). (c) $m_{tot}(B)$ for $i = 2, 3, 4, 5$ in the first quadrant. (d) $m_{Cu}(B)$ for $i = 2, 3, 4, 5$ in the first quadrant. (e) Log-log plot of the error averaged over time for m_{tot} (blue points), J_c (red points), and $\langle T \rangle$ (purple points).

first try is obviously very poor and as the convergence tapers off for $i \geq 10$. We notice that the final error on J_c is significantly larger than for the other quantities. This error difference is expected between J_c and m_{tot}, as the error on J_c is directly dependent on the error on m_{tot} in addition to any other error source. While justifying the existence of this error difference between J_c and $\langle T \rangle$ is less obvious as J_c and $\langle T \rangle$ are coupled to each other in $J \times B \times T$ space, the observed difference is also normal considering that most of the sample's thermal mass does not come from the superconductor (recall that we assume all other materials are perfectly known, which is in fact the case since our reference data is generated numerically).

4.4 Discussion on PFM Results and Limitations

4.4.1 Mapping the $J \times B \times T$ Critical Surface

Knowing that the state of the sample travels on the $J \times B \times T$ critical surface during the pulse, the natural question is to know whether or not the critical surface can be resolved. While we do not propose an exhaustive methodology here, we go over some of our observations. Let us also note that, once the sample is cut, the parameters available to the experimentalist are the peak field B_{pk}, the initial temperature T_0, and the pulse width Δt.

Figures 4.7 (a) and (b) present the paths for two pulse sequences. In figure 4.7 (a), B_{pk} and T_0 are swept such that $(B_{pk}, T_0) = (60\ \text{T}, 4\ \text{K})$, $(50\ \text{T}, 7\ \text{K})$, $(40\ \text{T}, 10\ \text{K})$, $(30\ \text{T}, 13\ \text{K})$, $(20\ \text{T}, 16\ \text{K})$ while $\Delta t = 2$ s is kept constant. In figure 4.7 (b), $B_{pk} = 30$ T and $\Delta t = 2$ s are held constant with $T_0 = 4$ K, 9 K, 14 K, 19 K, and 24 K. The black curves represent the reference paths obtained with our reference model (the same one as in figure 4.4) and the magenta dashed curves represent the curves obtained with our optimization method. From both measurements, we notice that the low T and high B region is not reached by any of the sample paths. This is normal as the critical current is maximal at the beginning of the pulse, which implies that heating is most important at this time as well. It can also be noticed that the temperature does not increase much once the peak of the pulse is reached. This is because J_c is low and there is comparatively little dissipation in the high B region.

Considering this, the ideal pulsing strategy should aim to disperse the paths on the critical surface as much as possible, such that the number of non-redundant sampling points is maximized. To better select pulse parameters, let us note the following heuristics.

- Increasing B_{pk} increases heating.
- Increasing Δt reduces heating.
- Increasing T_0 leads to a similar final temperature for wide T_0 ranges.

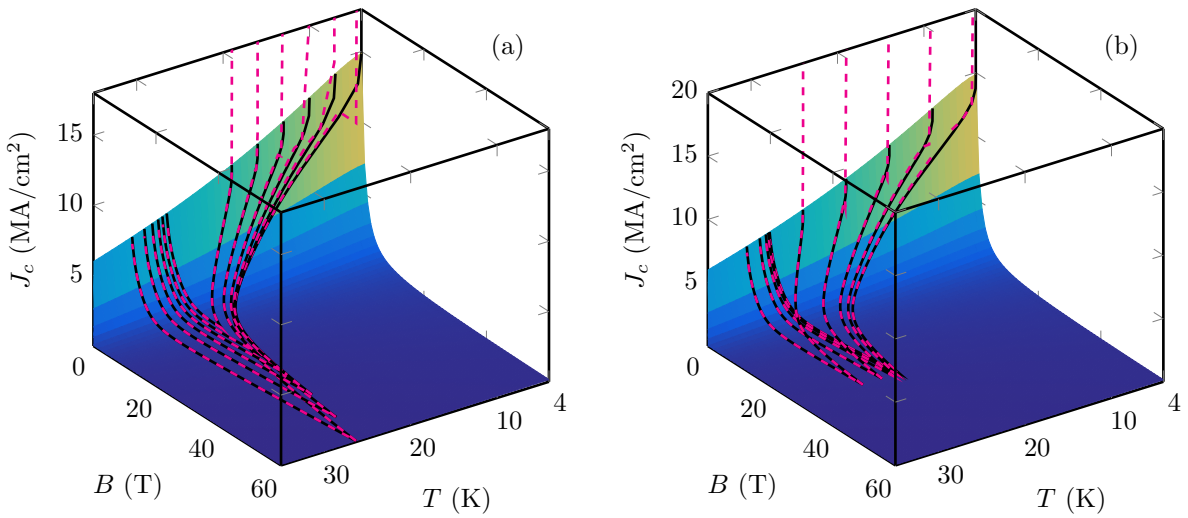


Figure 4.7 Mapping of $J \times B \times T$ space. (a) Pulse sequence with $(B_{pk}, T_0) = (60\text{ T}, 4\text{ K})$, $(50\text{ T}, 7\text{ K})$, $(40\text{ T}, 10\text{ K})$, $(30\text{ T}, 13\text{ K})$, $(20\text{ T}, 16\text{ K})$ with the pulse length held constant at $\Delta t = 2$ s. (b) Pulse sequence with $B_{pk} = 30$ T and $\Delta t = 2$ s held constant and with $T_0 = 4$ K, 9 K, 14 K, 19 K, and 24 K.

These principles can be combined, for instance, to attempt having concentric paths on the critical surface by decreasing B_{pk} as T_0 is increased (notice that this is what was done in figure 4.7 (a)). Another strategy could be, e.g., to keep B_{pk} and Δt constant and such that heating is minimized (i.e. small B_{pk} and large Δt) and increase T_0 in wide jumps such that the sample's state stays in the vicinity of the T_0 of its own pulse. A less productive example is given in figure 4.7 (b), where path segments from several pulses overlap.

Once the pulsing data has been collected, it can be fed to our algorithm to compute what the individual paths on the critical surface are. Once the paths are known, the surface could be calculated, for instance, by interpolating between the ascending and descending branches of the paths (with respect to the pulse's field) or by doing a curve fit with an equation similar to equation 4.2.

4.4.2 Error Due to the n Value Selection

The most obvious issue with this measurement method is the assumption of an n value to use in the E-J constitutive equation. This is also an issue with QSFM, but there is no ambiguity as to which n value must be chosen, as the Bean model is assumed to be valid. This is not the case here, however, and the problem is further complexified as n is generally a function of B and T and the state of the sample travels over large regions of the $J \times B \times T$ space. This is different from QSFM, where the sample's state does not move along the T direction of the critical surface. We have therefore looked at the error caused by the choice

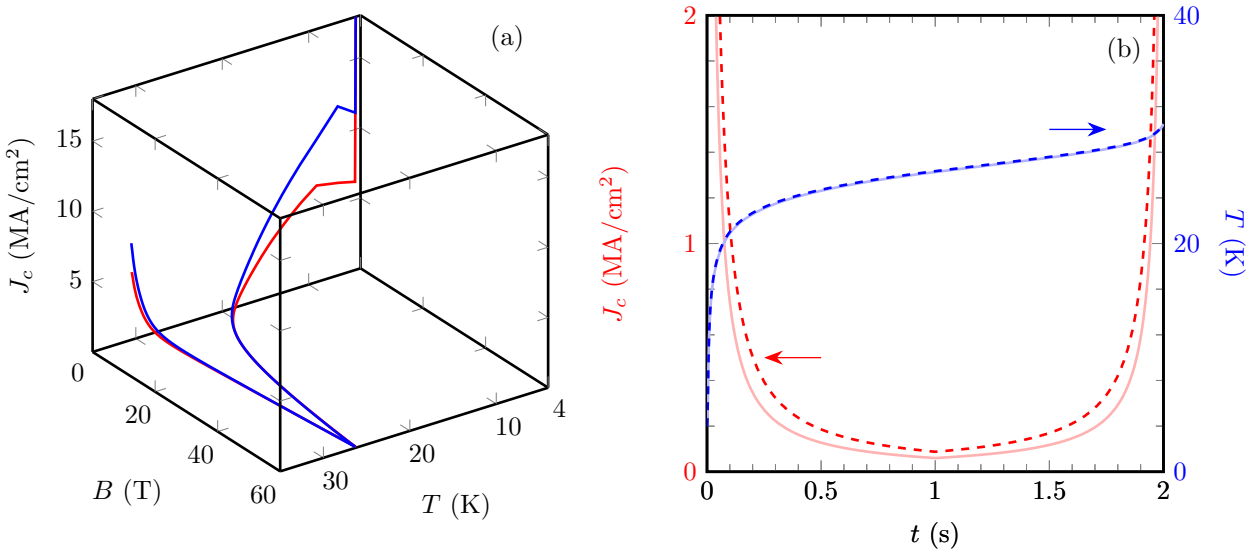


Figure 4.8 PFM results with different n values. (a) $J_c(B(t), T(t))$ in $J \times B \times T$ space for $n = 10$ (red curve) and $n = 60$ (blue curve). (b) $J_c(t)$ (red curves) and $\langle T(t) \rangle$ (blue curves) for $n = 10$ (solid curves) and $n = 60$ (dashed curves).

of n. We test the cases $n = 10$, 20, 30, 40, 50, and 60 and the results for $n = 10$ and 60 are displayed in figure 4.8. The different $J_c(B(t), T(t))$ paths in the $J \times B \times T$ space are displayed in figure 4.8 (a) for $n = 10$ and 60, such that the difference is most pronounced. The critical surface is not plotted for visibility. One can see that the paths are quite close once the heating has tapered off. Figure 4.8 (b) shows $J_c(t)$ and $\langle T(t) \rangle$ for the paths shown in figure 4.8 (a). The first noticeable thing is that $\langle T(t) \rangle$ is very close for both $n = 10$ and $n = 60$. This happens because the algorithm converges towards the same $J(t)$ (not J_c) distribution regardless of the n value and, since dissipation is only dependent on J and E (recall equation (2.6)), $\langle T(t) \rangle$ is the same in both cases. The difference is seen in the J_c calculation. As was pointed out previously, m_n increases in norm when the n value decreases. Therefore, J_c is smaller for smaller n values even though J is the same. Physically speaking, this is a consequence of the fact that the E-J constitutive law becomes less non-linear as n decreases and allows a higher J for the same electric field and J_c. Looking at the paths on the critical surface, an error on n induces a time-varying vertical shift of the sample's path in the J_c direction. In a practical setting, the experimentalist is safe considering the error on $\langle T \rangle$ and its convergence to be of the order of what was shown in figure 4.6 (e), while they should consider bounding J_c by using the presented algorithm with some maximal and minimal n values.

Let us note that while QSFM methods usually make the Bean model assumption, it is

nonetheless possible to do n value measurements either with a relaxation measurement, where the relation $n^{-1} = |d(ln(m))/dt|$ can be used, or by doing several different measurements with varying field ramping rates, using the relation $n^{-1} = |d(ln(m))/d\dot{B}_a|$ [50]. These methods are, however, not well suited for PFM. Indeed, relaxation measurements would not be possible in a pulsed magnet, or at least it would be hard to get satisfactory sampling. For instance, the 60 T controlled waveform magnet [80] at the NHMFL Pulsed Field Facility can maintain B_{pk} for at most 100 ms, at which point one could think of measuring relaxation, but it would only provide a single point in the $n = n(B, T)$ landscape. Let us mention that relaxation times in superconductors are usually in the order of years, which makes accurate observations difficult for such short timescales. With regard to repeating measurements while varying the ramping rate, it seems like this method would be difficult since changing the ramping rate would change the path taken by the superconductor in the $J \times B \times T$ space. That being said, n could be calculated at the intersection of paths, but this would constitute a somewhat crude measurement and it would be hard to properly resolve the $J \times B \times T$ space.

4.4.3 Experimental Considerations for Future PFM Measurements

The work done in this chapter is a preliminary step that was taken on the way to eventually doing accurate PFM measurements. That being said, our numerical trials had the advantage of being consistent with our reference data by definition, since the optimization was carried out with exactly the same geometry, extensive and intensive properties, etc. For practical measurements, it goes without saying that all of these aspects need to be known *a priori* if the numerical model is to be accurate.

The most important correction that would have to be made pertains to how heat exchange is modelled between the sample and the exterior. In our numerical model, we chose to have adiabatic boundary conditions to avoid modelling non-ideal experimental conditions. These include inhomogeneous contact between samples, inhomogeneous contact with the vacuum grease because of, for instance, air bubbles, and inhomogeneous contact with the bottom of the ampule. That being said, choosing to model these accurately would be challenging to say the least. A maybe simpler option in the long run would be to have a temperature sensor on the sample during the experiment. In principle, this would allow the possibility of bypassing thermal modelling since $\langle T(t) \rangle$ would be measured (or at least used to set a boundary condition), as opposed to numerically calculated from Joule heating. This would, however, require the experimental setup to be modified, as more space would be needed for the sample and the temperature probe. Indeed, the ampule that was used only has a 1 mm diameter. Modifying the setup could also be used as an opportunity to potentially enable the use of single samples with larger L and W, as opposed to a stack of smaller samples. This

would firstly be interesting because there would only be one sample geometry to account for, reducing the error, and secondly, because it would allow the sample to be considered as a thin plate and χ_m could be calculated using the demagnetizing tensor formalism (in the cases where M_r is significant).

Several other experimental considerations should also be resolved to make accurate measurements. The most essential are the following.

- The measurements presented in section 4.1 have an artificially added offset to visualize the difference between $m(B = 0, t_0)$ and $m(B = 0, t_e)$. This was done because the apparatus that was used only records the voltage in the pickup coils from t_0 to t_e for a given pulse, which makes it impossible to measure the change in magnetization as the sample cools down between pulses. That being said, it is unclear how long it takes for the sample to cool down and if the change in magnetization is substantial enough to be read with the magnetization probe that was used. More work needs to be done to determine this.

- Pulsed measurements can be violent enough for mechanical vibrations to alter the measurement. In such instances, the sample moves with respect to the pickup coil and a parasitic voltage appears. Such a measurement is shown in figure 4.9, where the measurement was performed with a stack of six samples at 4 K. While the data corresponding to the ascending portion of the pulse is smooth, the data from the descending portion is very noisy because mechanical vibrations have time to propagate as $\partial B_a/\partial T$ decays (recall the waveform shown in figure 4.2 (c)). Without sophisticated smoothing or filtering, there is no choice but to discard this part of the data. Comparing the $B_z > 0$ and the $B_z < 0$ data, we can see that the noise is not symmetrical and is not reproduced from one pulse to the next. In the event that single sample measurements are performed as mentioned above, this has to be addressed, especially if a 65 T short pulse magnet [81] is used.

- It goes without saying that all the properties of the non-superconducting materials in the sample must be well known for the simulation approach to work. That being said, measuring all the necessary properties (ρ, ρ_m, κ, c_p, χ_m, etc.) might prove to be a very labour-intensive process, as it was shown in [82] that many of these properties are functions of B, T, etc.

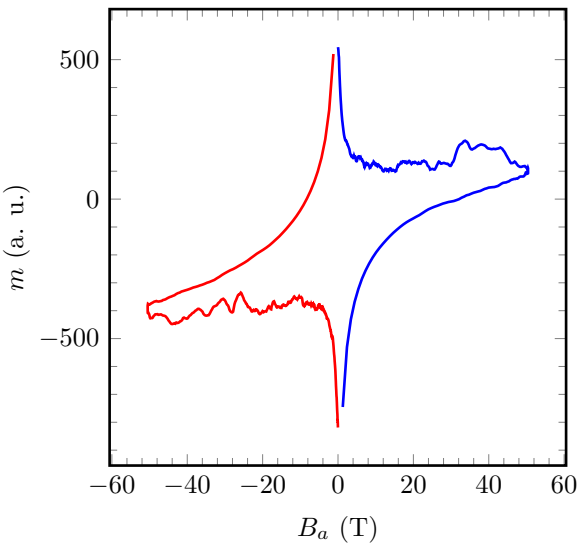


Figure 4.9 PFM measurement altered by mechanical vibrations. The differing colours of the curves indicate that they are calculated from different pulses. The effect of the parasitic voltage is visible on the descending portion of the pulses.

CHAPTER 5 PERSPECTIVES AND GENERALIZATION

This chapter discusses future perspectives and the generalization of the methods that were proposed in the previous chapters. Section 5.1 discusses what the next steps should be to better develop QSFM and PFM in perpendicular fields and section 5.2 offers a discussion on how to go about the generalization of PFM to scenarios with fields of arbitrary orientation.

5.1 Short-Term Improvements to QSFM and PFM

QSFM and PFM as presented in this work can still be developed further. For QSFM, future work should be oriented towards rigorous validation of the method. As mentioned previously, a series of in-field transport measurements should be performed and used for comparison. This validation process should aim to validate J_c measurements for full 360° rotations of both $\varphi_\perp$ and $\varphi_\parallel$. This would allow us to see if our QSFM method captures the complex features of commercial conductors, e.g., the difference in $J_c(B, \varphi_\perp)$ and $J_c(B, \varphi_\parallel)$ peaks that are 180° apart (recall the effect of different pinning potentials on the top and bottom faces of the superconducting layer [75]), the irregularities in J_c due to anisotropic pinning centres [76,83], etc. Depending on the method used for the growth of the superconductor, this could also be an opportunity to study which electric field criterion is most suitable for both transport and magnetization measurements to correspond [9]. The numerical validation method presented in section 3.3 could also be more rigorous. Indeed, while our method took advantage of the possibility to calculate J distributions during simulations, the force-free physics were not accurately captured and we could therefore not validate the accuracy of the method when, for instance, m_h and m_{v2} are the existing configurations for a given field (recall that we only observed $m_v = m_{v1}$ numerically). Finally, measurements could be done with samples that have J_c anisotropy in the ab plane such that the procedure described in section 3.4.1 can be tried out.

Future work on PFM should be focused on making accurate experimental measurements. The next obvious step is to do calibrated measurements (our own were only qualitative in nature). Calibration could be done by measuring the magnetic moment of a sample with a known magnetic moment with the PFM apparatus and establishing a correspondence between measured magnetic flux (i.e. integrated voltage) and magnetic moment. The reference magnetic moment can be measured with, for instance, a VSM or a SQUID. The sample could be a well-known nickel sample, as in [78], or the superconducting sample itself. The latter would, however, only provide a comparison point at $B_a = 0$ T before the start of the pulse (the pulse starts shortly after data recording starts, as in figure 4.2 (c), where the onset is

after $t = 0$ s), since the high $\partial B/\partial t$ changes m with respect to QSFM measurements at any other time. Furthermore, the use of our PFM algorithm requires the thermal, magnetic, and electrical properties of the other sample layers to be well known, as these all generally vary with temperature, magnetic field, etc., as mentioned in [82]. The properties of interest are ρ, κ, c_p, ρ_m, χ_m, etc., and measuring them would be very important for accurate PFM calculations. Finally, we chose to ignore reversible magnetization in our PFM algorithm, but it must be considered for a true generalized measurement.

5.2 Generalization of QSFM and PFM to PFM in Fields of Arbitrary Orientation

While a procedure for PFM measurements in fields of arbitrary orientation is not presented here, we discuss the previous assumptions that were made and how they translate to the context of generalized PFM. Let us start by reviewing the relevant ones that were made for QSFM, namely, the applied field is large enough that $B \approx B_a$, the sample's geometry is thin enough that $\mathbf{B}$, $\mathbf{H}$, and $\mathbf{M}$ are uniform across the thickness d, and the Bean model is valid. The first two stay true no matter the $\partial B_a/\partial t$ and can be assumed for general PFM measurements. As discussed in chapter 4, however, the Bean model is obviously not valid anymore when considering pulsed fields. That being said, sharp current partitions can still be expected. A demonstrative simulation was done with the same parameters as in table 3.2 except for $\partial B_a/\partial t = 35$ T/s, $\theta = 80°$, and $B_{c\|} = 10$ T, and the resulting J distributions associated with C_h and C_v are shown in figure 5.1 (let's add the caveat that T was not taken into account).

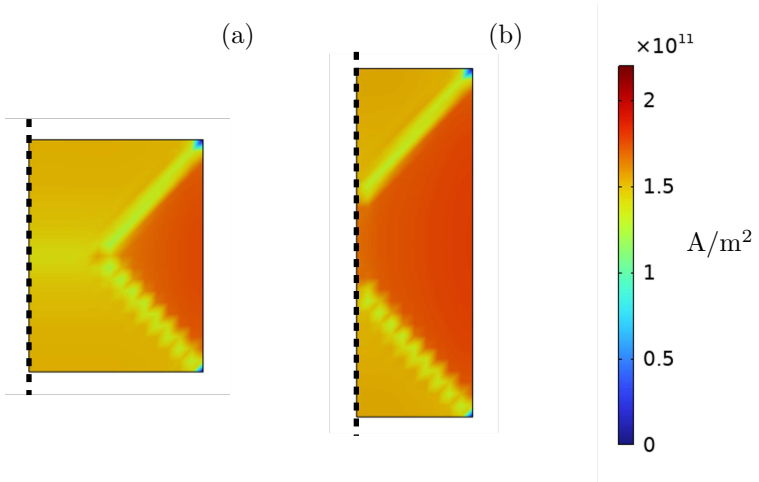


Figure 5.1 Simulated J colour plot at $B_a = 3$ T and $\theta = 80°$. (a) C_h and (b) C_v. The dashed lines represent the symmetry plane.

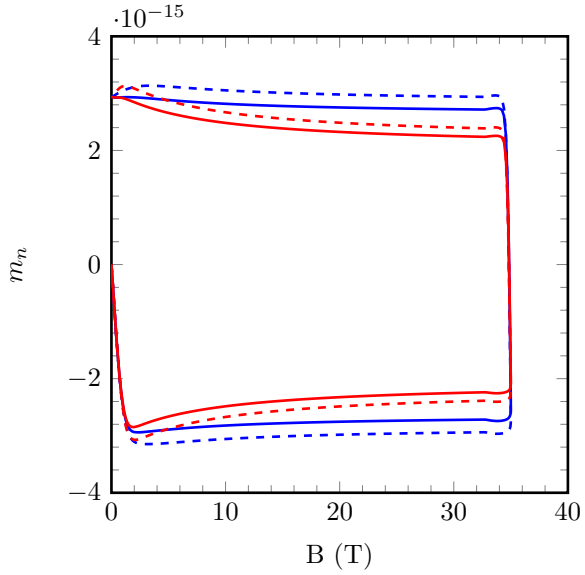


Figure 5.2 Normalized magnetic moment m_n half-hysteresis loops at $\theta = 80°$. The blue curves correspond to $B_{c\|} = 10$ T and the red curves correspond to $B_{c\|} = 50$ T. The solid lines correspond to m_h and the dashed lines correspond to m_v.

The most important assumption made for PFM, which was considered true after preliminary experimental and numerical measurements, is that T is approximately uniform in the sample. Considering that heating is a function of the $\mathbf{J} \cdot \mathbf{E}^*$ product (where the * exponent denotes the complex conjugate), this might not be true anymore. Indeed, it was shown in [84] that E is not uniform along the current loops in rectangular samples. This is in stark contrast with the cylindrical sample where, by symmetry, E is constant along the current paths concentric to the perimeter. What's more, anisotropy, regardless of its origin, creates regions of different J_c and, therefore, different J. These arguments seem to indicate that T is not uniform in rectangular samples magnetized in pulsed fields where anisotropy is present, or at least that heat generation is not uniform. That being said, T was still uniform in the cylindrical sample, despite the fact that E has a radial dependence (recall equation (4.5)) and J is larger towards the outside edges (recall figure 4.5 (a)). We attribute this to the presence of the other sample layers. This effect could be validated numerically for rectangular samples subject to PFM, but we leave this to future contributions as good convergence is a challenge in its own right.

Another element that changes significantly from PFM to generalized PFM is the notion of m_n. Let's recall that the integrand of m_n is given by $(\mathbf{r} \times \mathbf{J})/J_c$. Now that there is anisotropy and potentially a non-uniform T distribution, we must potentially deal with a continuous J_c spatial distribution in the sample. If we ignore T for now, we can attempt to generalize

the definition of m_n by using $J_c = (J_{c\perp}^2 + J_{c\parallel}^2)^{1/2}$. The behaviour of m_n calculated with this definition is shown in figure 5.2, where blue (red) curves use $B_{c\parallel} = 10$ T ($B_{c\parallel} = 50$ T) as an input (recall that equation (3.24) is used) and solid (dashed) lines are associated to C_h (C_v). Firstly, it can be seen that $m_{nh} \neq m_{nv}$. Secondly, m_{nh} and m_{nv} are shown to not be the same for both $B_{c\parallel} = 10$ T and $B_{c\parallel} = 50$ T. While this does not mean that m_n cannot be used for generalized PFM, it does show that some of its properties are lost, like independence with respect to the input J_c distributions and to the given configuration.

Considering the previous points, the generalized PFM algorithm will have to be substantially different from the ones presented for QSFM and PFM in perpendicular fields. Assuming that an optimization approach is desired, the most general method, for cases when there are no heuristic principles that can be taken advantage of, would be to use a black box optimization method like the Nelder-Mead algorithm. The input parameters should at least include J_{c1} and Γ distributions. That being said, the price to pay for a very general method with no *a priori* assumptions is the speed of convergence towards a solution. Other methods similar to the one in [76] could also be explored, where the error on the experimental measurement is used to generate the J_c distribution of the next iteration. That being said, all of these methods need initial J_c distributions as inputs and a first guess must be provided. In these circumstances, the formalism from chapter 3 could be used as it is to find $J_{c\perp}$ and $J_{c\parallel}$ distributions.

CHAPTER 6 CONCLUSION

6.1 Summary of Contributions

The contributions that were presented in this work pertain to the development of a general QSFM method for measurements in fields of arbitrary orientation and to the proposition of an iterative method leveraging the FEM for PFM measurements, both for samples of thin geometry.

With regard to QSFM, we presented an analytical framework for pairs of magnetization measurements where the Bean model was assumed and where anisotropy was dealt with by making as many independent measurements as there are unknown J_c values. The anisotropy due to force-free effects was the main case that was studied and guidelines for dealing with crystallographic anisotropy with or without force-free effects were enunciated. The calculation method revolves around the calculation of the ratio $\Gamma = J_{c2}/J_{c1}$ and the independence of measurements is achieved by rotating the sample around its normal (when only force-free effects are involved). A series of QSFM measurements were done with a rectangular sample cut from a commercial tape for several angles. With the obtained data, $J_c(B, \varphi_\perp)$ and $J_c(B, \varphi_\parallel)$ were calculated and the error due to the measurement of m was analyzed. The main trends that were extracted from our results are that error increases with angle (when using a single pickup coil) and that the error on J_{c2} is larger than the error on J_{c1} because $J_{c2} \propto \Gamma^2$. It was also noted that, when $m_v = m_{v2}$ and $Lm_h \approx Wm_v$, the Γ calculation is very sensitive to the error on m because of a singularity in the equations. A preliminary validation of the method was done by using an FEM model, and the error was found to be below 5% for both J_{c1} and J_{c2}. The source of the error calculated in this validation is the Bean model assumption ($n \to \infty$), as opposed to a physical error related to the experimental apparatus. That being said, we saw that this validation is only preliminary as more investigation into the accurate FEM modelling of superconductor anisotropy is warranted. Finally, a discussion was given as to the interpretation of our results, namely, the nature of Γ and how to interpret $\Gamma \in \mathbb{C}$, how to generalize QSFM to scenarios where multiple kinds of anisotropy are involved, and the interpretation of results from samples with non-idealities.

With regard to PFM, we first presented a preliminary experiment and a preliminary simulation, which were done to make simplifying assumptions. The important takeaways are that heating and screening currents in non-superconducting layers are not negligible, the temperature is approximately uniform in the sample, and, in general, M_r cannot be neglected. The PFM algorithm that we proposed hinges on the calculation of m_n in the superconducting layer of the sample and on an iterative process that is used to deal with

the coupling between the layers of the sample. Another particularity of our algorithm is that the input J_c distribution is calculated as a function of time and not as a function of field and/or temperature. This is done as the path of the state of the sample on the critical surface is unknown *a priori*. The algorithm was tested on numerically generated data, where the reference $J \times B \times T$ critical surface was fitted with a polynomial function to $m(T)$ data measured with a commercial sample. Our results include the sample's path on the $J \times B \times T$ critical surface, the behaviour of the convergence of different layers, and an analysis on the convergence order of the method. The obtained convergence orders for $m(t)$, $J_c(t)$, and $\langle T(t) \rangle$ were respectively 2.91, 1.66, and 2.94. A discussion was offered with respect to the results, namely, bounding the error stemming for the choice of the n value, pulsing strategies for mapping the $J \times B \times T$ critical surface, and future considerations for real experimental measurements.

REFERENCES

[1] M. Tinkham, *Introduction to Superconductivity*, 2nd ed. New York, NY, USA: McGraw–Hill, 1996.

[2] R. G. Sharma, *Superconductivity: Basics and Applications to Magnets*, ser. Springer Series in Materials Science. Cham, Switzerland: Springer International Publishing, 2015, vol. 214.

[3] Committee on the Current Status and Future Direction of High-Magnetic-Field Science in the United States, Phase II, *The Current Status and Future Direction of High-Magnetic-Field Science and Technology in the United States*. Washington, D.C.: National Academies Press, Sep. 2024.

[4] Y.-H. Zhou, D. Park, and Y. Iwasa, "Review of progress and challenges of key mechanical issues in high-field superconducting magnets," *National Science Review*, vol. 10, no. 3, p. nwad001, Feb. 2023.

[5] C. Senatore *et al.*, "Field and temperature scaling of the critical current density in commercial REBCO coated conductors," *Superconductor Science and Technology*, vol. 29, no. 1, p. 014002, Jan. 2016.

[6] G. Jakob *et al.*, "Scaling of the angular dependence of the critical current density in high-T_c superconductors," *Physical Review B*, vol. 47, no. 18, pp. 12 099–12 103, May 1993.

[7] X. Zhang *et al.*, "Study of critical current and n-values of 2G HTS tapes: Their magnetic field-angular dependence," *Journal of Superconductivity and Novel Magnetism*, vol. 31, no. 12, pp. 3847–3854, Dec. 2018.

[8] J. Jaroszynski *et al.*, "Rapid assessment of REBCO CC angular critical current density J_c (B, $T = 4.2$ K, θ) using torque magnetometry up to at least 30 tesla," *Superconductor Science and Technology*, vol. 35, no. 9, p. 095009, Sep. 2022.

[9] J. W. Ekin, *Experimental Techniques for Low-Temperature Measurements: Cryostat Design, Material Properties, and Superconductor Critical-Current Testing*. Oxford ; New York: Oxford University Press, 2006.

[10] M. Nikolo *et al.*, "Upper critical and irreversibility fields in $Ba(Fe_{0.95}Ni_{0.05})_2As_2$ and $Ba(Fe_{0.94}Ni_{0.06})_2As_2$ pnictide bulk superconductors," *Journal of Superconductivity and Novel Magnetism*, vol. 30, no. 2, pp. 331–341, Feb. 2017.

[11] ——, "Upper critical and irreversibility fields in $Ba(Fe_{0.92}Co_{0.08})_2As_2$ and $Ba(Fe_{0.91}Co_{0.09})_2As_2$ pnictide bulk superconductors," *Journal of Superconductivity and Novel Magnetism*, vol. 30, no. 3, pp. 561–568, Mar. 2017.

[12] S. Hahn *et al.*, "45.5-tesla direct-current magnetic field generated with a high-temperature superconducting magnet," *Nature*, vol. 570, no. 7762, pp. 496–499, Jun. 2019.

[13] National High Magnetic Field Laboratory, "Pulsed Field Magnets and Instruments," https://nationalmaglab.org/user-facilities/pulsed-field/magnets/, [Online]. Accessed: 2025-11-10.

[14] Laboratoire National des Champs Magnétiques Intenses, "Nondestructive pulsed magnetic fields at LNCMI-Toulouse," https://lncmi.cnrs.fr/en/pulsed-fields/, [Online]. Accessed: 2025-12-17.

[15] X. Han *et al.*, "The pulsed high magnetic field facility and scientific research at Wuhan National High Magnetic Field Center," *Matter and Radiation at Extremes*, vol. 2, no. 6, pp. 278–286, Nov. 2017.

[16] E. H. Rhoderick and R.-I. A. C., *Introduction to Superconductivity.* Pergamon Press, 1969.

[17] P. W. Anderson, "Theory of Flux Creep in Hard Superconductors," *Physical Review Letters*, vol. 9, no. 7, pp. 309–311, Oct. 1962.

[18] P. W. Anderson and Y. B. Kim, "Hard superconductivity: Theory of the motion of Abrikosov flux lines," *Reviews of Modern Physics*, vol. 36, no. 1, pp. 39–43, Jan. 1964.

[19] F. Sirois, "Modélisation de la caractéristique E-J des supraconducteurs à haute temperature critique," Ph.D. dissertation, Polytechnique Montréal, 2002. [Online]. Available: https://publications.polymtl.ca/7091/

[20] T. Matsushita, *Flux Pinning in Superconductors*, ser. Springer Series in Solid-State Sciences. Cham, Switzerland: Springer International Publishing, 2022, vol. 198.

[21] D. G. Walmsley, "Force free magnetic fields in a type II superconducting cylinder," *Journal of Physics F: Metal Physics*, vol. 2, no. 3, pp. 510–528, May 1972.

[22] Y. Nakayama and O. Horigami, "A.C. losses of Nb-Ti wires," *TEION KOGAKU (Journal of Cryogenics and Superconductivity Society of Japan)*, vol. 6, no. 3, pp. 95–105, 1971.

[23] B. Maiorov *et al.*, "Effects of the variable Lorentz force on the critical current in anisotropic superconducting thin films," *IEEE Transactions on Applied Superconductivity*, vol. 17, no. 2, pp. 3697–3700, Jun. 2007.

[24] J. R. Cave, J. E. Evetts, and A. M. Campbell, "AC flux penetration measurements on force free configurations in reversible type II superconductors," *Le Journal de Physique Colloques*, vol. 39, no. C6, pp. C6–616, Aug. 1978.

[25] C. J. Bergeron, "Simple model for longitudinal force-free current flow in superconductors of the second kind," *Applied Physics Letters*, vol. 3, no. 4, pp. 63–66, Aug. 1963.

[26] J. R. Clem, "Steady-state flux-line cutting in type II superconductors," *Journal of Low Temperature Physics*, vol. 38, no. 3-4, pp. 353–370, Feb. 1980.

[27] E. H. Brandt, "Continuous vortex cutting in type II superconductors with longitudinal current," *Journal of Low Temperature Physics*, vol. 39, no. 1-2, pp. 41–61, Apr. 1980.

[28] E. H. Brandt, J. R. Clem, and D. G. Walmsley, "Flux-line cutting in type II superconductors," *Journal of Low Temperature Physics*, vol. 37, no. 1-2, pp. 43–55, Oct. 1979.

[29] T. Matsushita and M. Kiuchi, "Consideration on appearance and disappearance of energy in superconductors during change in external magnetic field," *Japanese Journal of Applied Physics*, vol. 57, no. 10, p. 103101, Oct. 2018.

[30] T. Matsushita *et al.*, "Critical current density of superconducting Pb–Bi alloys with normal Bi precipitates in a longitudinal magnetic field," *Japanese Journal of Applied Physics*, vol. 25, no. 9A, p. L725, Sep. 1986.

[31] C. P. Bean, "Magnetization of hard superconductors," *Physical Review Letters*, vol. 8, no. 6, pp. 250–253, Mar. 1962.

[32] ——, "Magnetization of high-field superconductors," *Reviews of Modern Physics*, vol. 36, no. 1, pp. 31–39, Jan. 1964.

[33] J. Rhyner, "Magnetic properties and AC-losses of superconductors with power law current—voltage characteristics," *Physica C: Superconductivity*, vol. 212, no. 3-4, pp. 292–300, Jul. 1993.

[34] E. Zeldov *et al.*, "Flux creep characteristics in high-temperature superconductors," *Applied Physics Letters*, vol. 56, no. 7, pp. 680–682, Feb. 1990.

[35] W. Paul, D. Hu, and T. Baumann, "Voltage-current characteristic between 10^{-13} V/cm and 10^{-13} V/cm of BSCCO and time decay of the magnetization," *Physica C: Superconductivity*, vol. 185, pp. 2373–2374, 1991.

[36] E. Zeldov *et al.*, "Optical and electrical enhancement of flux creep in $YBa_2Cu_3O_{7-\delta}$ epitaxial films," *Physical Review Letters*, vol. 62, no. 26, pp. 3093–3096, Jun. 1989.

[37] T. T. M. Palstra *et al.*, "Thermally activated dissipation in $Bi_{2.2}Sr_2Ca_{0.8}Cu_2O_{8+\delta}$," *Physical Review Letters*, vol. 61, no. 14, pp. 1662–1665, Oct. 1988.

[38] J. D. Hettinger *et al.*, "Flux creep and high-field critical currents in epitaxial thin films of $YBa_2Cu_3O_7$," *Physical Review Letters*, vol. 62, no. 17, pp. 2044–2047, Apr. 1989.

[39] F. Gömöry *et al.*, "Phenomenological description of flux pinning in non-uniform high-temperature superconductors in magnetic fields lower than the self-field," *Superconductor Science and Technology*, vol. 20, no. 9, pp. S271–S277, Sep. 2007.

[40] J. R. Clem *et al.*, "Theory and experiment testing flux-line cutting physics," *Superconductor Science and Technology*, vol. 24, no. 6, p. 062002, Jun. 2011.

[41] C. Romero-Salazar and F. Pérez-Rodríguez, "Critical state of anisotropic hard superconductors," *Superconductor Science and Technology*, vol. 16, no. 11, pp. 1273–1281, Nov. 2003.

[42] C. Romero-Salazar and F. Pérez-Rodríguez, "Elliptic flux-line-cutting critical-state model," *Applied Physics Letters*, vol. 83, no. 25, pp. 5256–5258, Dec. 2003.

[43] ——, "Response of hard superconductors to crossed magnetic fields: Elliptic critical-state model," *Physica C: Superconductivity*, vol. 404, no. 1-4, pp. 317–321, May 2004.

[44] C. Lacroix and F. Sirois, "Concept of a current flow diverter for accelerating the normal zone propagation velocity in 2G HTS coated conductors," *Superconductor Science and Technology*, vol. 27, no. 3, p. 035003, Mar. 2014.

[45] Z. Hao *et al.*, "Model for the reversible magnetization of high-κ type-II superconductors: Application to high-T_c superconductors," *Physical Review B*, vol. 43, no. 4, pp. 2844–2852, Feb. 1991.

[46] E. H. Brandt, "Properties of the ideal Ginzburg-Landau vortex lattice," *Physical Review B*, vol. 68, no. 5, p. 054506, Aug. 2003.

[47] A. Abrikosov, "The magnetic properties of superconducting alloys," *Journal of Physics and Chemistry of Solids*, vol. 2, no. 3, pp. 199–208, Jan. 1957.

[48] L. Wang, H. S. Lim, and C. K. Ong, "Upper critical fields and order parameters of layered superconductors in a continuous Ginzburg-Landau model," *Superconductor Science and Technology*, vol. 14, no. 9, pp. 754–761, Sep. 2001.

[49] S. Candia and L. Civale, "Angular dependence of the magnetization of isotropic superconductors: Which is the vortex direction?" *Superconductor Science and Technology*, vol. 12, no. 4, pp. 192–198, Apr. 1999.

[50] M. Zehetmayer, "Simulation of the current dynamics in superconductors: Application to magnetometry measurements," *Physical Review B*, vol. 80, no. 10, p. 104512, Sep. 2009.

[51] A. Campbell and J. Evetts, "Flux vortices and transport currents in type ii superconductors," *Advances in Physics*, vol. 21, no. 90, pp. 199–428, 1972. [Online]. Available: https://doi.org/10.1080/00018737200101288

[52] E. Zeldov *et al.*, "Magnetization and transport currents in thin superconducting films," *Physical Review B*, vol. 49, no. 14, pp. 9802–9822, Apr. 1994.

[53] H. Theuss, A. Forkl, and H. Kronmüller, "Current density and magnetic field distribution in hard thin film superconductors," *Physica C: Superconductivity*, vol. 190, no. 3, pp. 345–352, Jan. 1992.

[54] M. Däumling and D. C. Larbalestier, "Critical state in disk-shaped superconductors," *Physical Review B*, vol. 40, no. 13, pp. 9350–9353, Nov. 1989.

[55] L. W. Conner and A. P. Malozemoff, "Calculations of the dimensional dependence of the critical state in disk-shaped superconductors," *Physical Review B*, vol. 43, no. 1, pp. 402–407, Jan. 1991.

[56] E. H. Brandt, M. V. Indenbom, and A. Forkl, "Type-II Superconducting Strip in Perpendicular Magnetic Field," *Europhysics Letters (EPL)*, vol. 22, no. 9, pp. 735–740, Jun. 1993.

[57] E. H. Brandt and M. Indenbom, "Type-II-superconductor strip with current in a perpendicular magnetic field," *Physical Review B*, vol. 48, no. 17, pp. 12 893–12 906, Nov. 1993.

[58] A. A. Zhukov *et al.*, "Geometrical locking of the irreversible magnetic moment to the normal of a thin-plate superconductor," *Physical Review B*, vol. 56, no. 5, pp. 2809–2819, Aug. 1997.

[59] E. M. Gyorgy *et al.*, "Anisotropic critical currents in $Ba_2YCu_3O_7$ analyzed using an extended Bean model," *Applied Physics Letters*, vol. 55, no. 3, pp. 283–285, 1989.

[60] M. Leroux *et al.*, "Dynamics and Critical Currents in Fast Superconducting Vortices at High pulsed Magnetic Fields," *Physical Review Applied*, vol. 11, no. 5, p. 054005, May 2019.

[61] J. Lu *et al.*, "Hysteresis Loss of REBCO Conductor Up to 35 T," *IEEE Transactions on Applied Superconductivity*, vol. 24, no. 3, pp. 1–4, Jun. 2014.

[62] A. I. Kosse *et al.*, "Measurements of the magnetic field and temperature dependences of the critical current in YBCO films and procedures for an appropriate theoretical model selection," *Superconductor Science and Technology*, vol. 21, no. 7, p. 075015, Jul. 2008.

[63] A. Arsenault, B. D. S. Alves, and F. Sirois, "COMSOL Implementation of the H-ϕ Formulation With Thin Cuts for Modeling Superconductors With Transport Currents," *IEEE Transactions on Applied Superconductivity*, vol. 31, no. 6, pp. 1–9, Sep. 2021.

[64] A. Arsenault, F. Sirois, and F. Grilli, "Implementation of the H-ϕ formulation in COMSOL Multiphysics for simulating the magnetization of bulk superconductors and comparison with the H-formulation," *IEEE Transactions on Applied Superconductivity*, vol. 31, no. 2, pp. 1–11, Mar. 2021.

[65] A. Arsenault *et al.*, "Magnetodynamic H-ϕ formulation for improving the convergence and speed of numerical simulations of superconducting materials," *IEEE Transactions on Applied Superconductivity*, vol. 33, no. 7, pp. 1–6, Oct. 2023.

[66] F. Huber *et al.*, "The T-A formulation: An efficient approach to model the macroscopic electromagnetic behaviour of HTS coated conductor applications," *Superconductor Science and Technology*, vol. 35, no. 4, p. 043003, Apr. 2022.

[67] F. Liang *et al.*, "A finite element model for simulating second generation high temperature superconducting coils/stacks with large number of turns," *Journal of Applied Physics*, vol. 122, no. 4, p. 043903, Jul. 2017.

[68] B. Dutoit, F. Grilli, and F. Sirois, Eds., *Numerical Modeling Of Superconducting Applications: Simulation Of Electromagnetics, Thermal Stability, Thermo-hydraulics And Mechanical Effects In Large-scale Superconducting Devices*, ser. World Scientific Series In Applications Of Superconductivity And Related Phenomena. Singapore: World Scientific Publishing Company, 2023.

[69] HTS Modelling Workgroup, "Magnetodynamic H-ϕ disk," https://htsmodelling.com/model-files/magnetodynamic-h-phi-disk, [Online]. Accessed: 2025-09-09.

[70] ——, "Modeling of HTS bulks surrounded by magnetic components using the H-φ formulation," https://htsmodelling.com/model-files/modeling-of-hts-surrounded, [Online]. Accessed: 2025-09-09.

[71] F. Sirois, F. Grilli, and A. Morandi, "Comparison of constitutive laws for modeling high-temperature superconductors," *IEEE Transactions on Applied Superconductivity*, vol. 29, no. 1, pp. 1–10, Jan. 2019.

[72] M. Kapolka, "Three-dimensional electromagnetic modeling of practical superconductors for power applications," Ph.D. dissertation, Slovak University of Technology in Bratislava, 2019.

[73] A. Badía-Majós, C. López, and H. S. Ruiz, "General critical states in type-II superconductors," *Physical Review B*, vol. 80, no. 14, p. 144509, Oct. 2009.

[74] M. Lyatti *et al.*, "In-plane anisotropy of electrical transport in $Y_{0.85}Tb_{0.15}Ba_2Cu_3O_{7-x}$ films," *Materials*, vol. 17, no. 3, p. 558, Jan. 2024.

[75] B. Roas, L. Schultz, and G. Saemann-Ischenko, "Anisotropy of the critical current density in epitaxial $YBa_2Cu_3O_x$ films," *Physical Review Letters*, vol. 64, no. 4, pp. 479–482, Jan. 1990.

[76] V. M. R. Zermeño *et al.*, "A parameter-free method to extract the superconductor's $J_c(B, \theta)$ field-dependence from in-field current–voltage characteristics of high temperature superconductor tapes," *Superconductor Science and Technology*, vol. 30, no. 3, p. 034001, Mar. 2017.

[77] F. Herlach *et al.*, "Experimental techniques for pulsed magnetic fields," *Physica B: Condensed Matter*, vol. 216, no. 3-4, pp. 161–165, 1996.

[78] A. Lagutin *et al.*, "A probe for magnetization measurements of thin superconducting films in pulsed high magnetic fields," *Review of scientific instruments*, vol. 66, no. 8, pp. 4267–4270, 1995.

[79] SuperPower Inc, "2G HTS Wire Specification," https://www.superpower-inc.com/specification.aspx, [Online]. Accessed: 2025-11-17.

[80] National High Magnetic Field Laboratory, "60 Tesla Controlled Waveform Magnet," https://nationalmaglab.org/user-facilities/pulsed-field/magnets/60-tesla-controlled-waveform/, [Online]. Accessed: 2025-11-17.

[81] National High Magnetic Field Laboratory, "65 Tesla Short Pulse Magnet," https://nationalmaglab.org/user-facilities/pulsed-field/magnets/65-tesla-magnet/, [Online]. Accessed: 2025-11-17.

[82] M. Bonura and C. Senatore, "High-field thermal transport properties of REBCO coated conductors," *Superconductor Science and Technology*, vol. 28, no. 2, p. 025001, Feb. 2015.

[83] A. Silhanek *et al.*, "Anomalous behavior of the irreversible magnetization and time relaxation in $YBa_2Cu_3O_7$ single crystals with splayed tracks," *Physical Review B*, vol. 60, no. 18, pp. 13 189–13 195, Nov. 1999.

[84] E. H. Brandt, "Electric field in superconductors with rectangular cross section," *Physical Review B*, vol. 52, no. 21, pp. 15 442–15 457, Dec. 1995.

APPENDIX A SUBTRACTION OF REVERSIBLE MAGNETIZATION FROM QSFM MEASUREMENTS

The extended QSFM formalism can only be used with the irreversible contribution of the magnetic moment. Considering that non-superconducting layers in the sample can have a magnetic response, the raw m_h and m_v data must be corrected. As mentioned in section 3.2.2, the correction is made by computing the average of the top and bottom branches of the hysteresis loops and then subtracting it to the uncorrected data. The average of both branches is equivalent to the reversible magnetization and the uncorrected data is equivalent to the total m_z. Figure A.1 shows an example of this process for m_h at $\theta = 75°$. It can be seen that the red curve, representing the irreversible m_z, is obtained by subtracting the purple curve to the blue one. The purple and blue curves are respectively the reversible magnetization (i.e. the correction that is subtracted) and the total m_z (i.e. the uncorrected data). We note that the top and bottom branches are of uneven length because of the current direction reversal after the sign change of $\partial B_a/\partial t$. To compute the average of both branches and apply the correction for the full B_a range, a linear extrapolation of the uncorrected magnetization data is done in the range where the current reversal occurs.

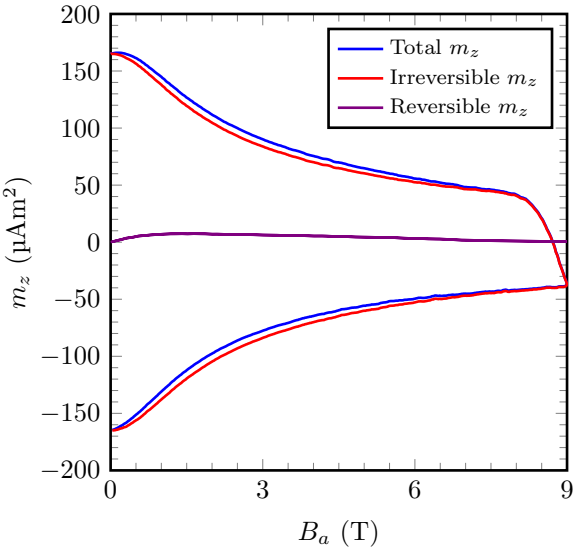


Figure A.1 Data correction process for m_h at $\theta = 75°$. The red curve is equivalent to the irreversible portion of the measured m_z and is obtained by subtracting the purple curve to the blue one. The purple and blue curves respectively represent the reversible portion of the measured m_z and the total m_z.

APPENDIX B QSFM MAGNETIZATION DATA AT 88°

Figure B.1 shows the measured m_h at $\theta = 88°$. This measurement is clearly dominated by the reversible magnetization of the sample since the top and bottom branches of the hysteresis loop are very close to each other, i.e. there is very little current penetration in the sample, and because the magnitude of m_z is very small compared to other angles.

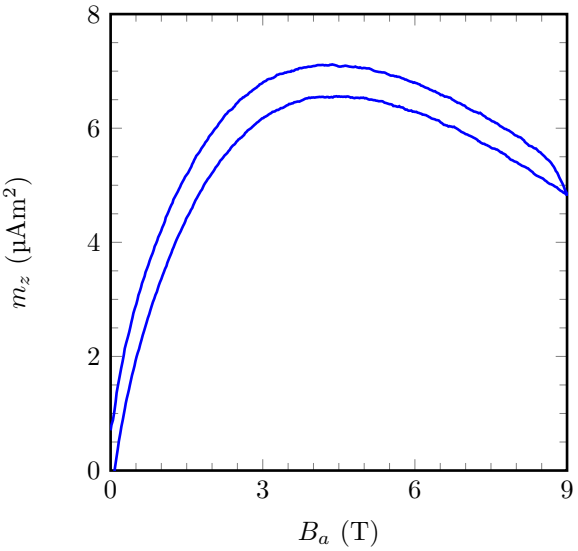


Figure B.1 m_z measurement in the horizontal configuration at $\theta = 88°$.

APPENDIX C DATA CORRECTION METHODOLOGY FOR QSFM MEASUREMENTS AT 85°

The current direction reversal in the sample occurs after the peak B_a value is reached and the sign of $\partial B_a/\partial t$ changes. Looking at figure C.1 (a), the data corresponding to this are the points of the top branch between ~ 6 T and 9 T. It can be seen that the current reversal takes place over a large range of applied fields. In these circumstances, it becomes inaccurate to use linear extrapolation to make possible the computation of the reversible magnetization over the whole B_a range, as is done in appendix A. In an attempt to render the measurement data at $\theta = 85°$ usable, we interpolate between the reversible magnetizations computed at $\theta = 80°$ and $88°$, where the reversible contributions are computed in the same manner as in appendix A. Once the interpolation is done, a scaling factor is applied such that the reversible magnetization intersects with the average of the top and bottom branches at a B_a value outside of the current reversal range. This is pictured in figure C.1 (a), where the scaled reversible m_z passes through the average of the top and bottom branches at $B_a = 3.6$ T. The top and bottom black dots indicate which points were used to compute the average, which is represented by the middle one. The result of the reversible magnetization calculation is presented in figure C.1 (b). It is noted that that despite using interpolation, the reversible magnetization computed at 85° does not share the same intersection point as the reversible magnetizations at 80° and 88° because of the scaling factor that is applied and data smoothing.

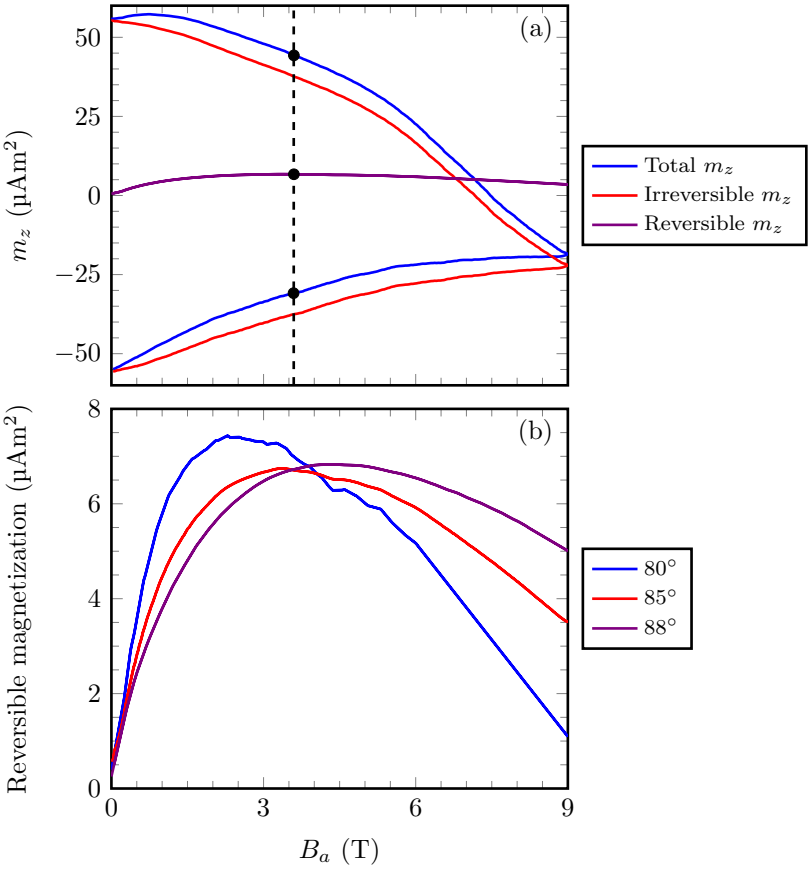


Figure C.1 Data correction process for m_h at $\theta = 85°$. (a) The red curve is equivalent to the irreversible portion of the measured m_z and is obtained by subtracting the purple curve to the blue one. The purple and blue curves respectively represent the reversible portion of the measured m_z and the total m_z. The purple curve is computed by interpolating between the reversible magnetization at 80° and 88° and then applying a scaling factor such that it intersects with the average of the top and bottom branches at $B_a = 3.6$ T. (b) The reversible magnetization computed for 80° and 88° are calculated with the method discussed in appendix A. The reversible magnetization at 85° is obtained by linearly interpolating between the data at 80° and 88° and applying a scaling factor such that it intersects with the average of the top and bottom branches of the hysteresis loops at $B_a = 3.6$ T.